UNIVERSITY OF GENOVA

PHD PROGRAM IN BIOENGINEERING AND ROBOTICS

# An information-theoretic approach to understanding the neural coding of relevant tactile features

by

**Miguel Ángel Casal Santiago**

Thesis submitted for the degree of *Doctor of Philosophy* (35° cycle)

March 2023

| | |
|---|---|
| Stefano Panzeri | Supervisor |
| Paolo Massobrio | Head of the PhD program |

***Thesis Jury:***

| | |
|---|---|
| Alberto Mazzoni, *Scuola Superiore Sant'Anna* | External examiner |
| Rasmus Petersen, *University of Manchester* | External examiner |
| Michela Chiappalone, *Università degli Studi di Genova* | Internal examiner |

Dibris

Department of Informatics, Bioengineering, Robotics and Systems Engineering


UNIVERSITY OF GENOVA

PHD PROGRAM IN BIOENGINEERING AND ROBOTICS

# An information-theoretic approach to understanding the neural coding of relevant tactile features

by

**Miguel Ángel Casal Santiago**

Thesis submitted for the degree of *Doctor of Philosophy* (35° cycle)

March 2023

| | |
|---|---|
| Stefano Panzeri | Supervisor |
| Paolo Massobrio | Head of the PhD program |

***Thesis Jury:***

| | |
|---|---|
| Alberto Mazzoni, *Scuola Superiore Sant'Anna* | External examiner |
| Rasmus Petersen, *University of Manchester* | External examiner |
| Michela Chiappalone, *Università degli Studi di Genova* | Internal examiner |

Dibris
Department of Informatics, Bioengineering, Robotics and Systems Engineering

— English below —

Me gustaría dedicar este trabajo a mucha gente. Sin embargo, siento que necesito poner a una persona por encima del resto aquí. Este viaje no ha sido sencillo, ha habido una pandemia global de por medio. Pero eso no es todo lo que ha sucedido para mí. El cáncer se llevó a mi madre a mitad del camino, pero eso no me ha parado. He conseguido juntar el trabajo de tres años en esta tesis, y siento que debo dedicárselo a ella. Simplemente, es por ti, Mamá.

I would like to dedicate this work to many people. However, I feel that someone is particularly important at this point. The PhD journey has not been precisely easy, including the pandemic, which has not been the only thing for me. Despite my mother loosing the battle against cancer at the half-way of my PhD, I have gathered all the work performed during the last three years in this thesis, and I feel it is all for her. It is yours, Mum.

# Acknowledgements

I need to start giving thanks to my supervisor, Stefano Panzeri, for giving me the opportunity to carry out this journey and belong to the Neutouch network as a Marie Skłodowska–Curie fellow. I also want to thank Chiara Bartolozzi, the Neutouch coordinator, for creating a stimulating network in which I found not only super smart people, but also amazing friends. I would like to thank Hannes Saal for welcoming me during a couple of months in his lab in the UK. Finally, thanks to the EU for the funding to perform this research, since this work was supported by the EU Horizon 2020 research and innovation programme under grant agreement 813713 (NeuTouch).

Aside from PIs, coordinators, and funding, many people deserves acknowledgement for this thesis, and I think I will never come up with a clear list of who has contributed, both scientifically and personally, to this work. You all know who you are, but I will try to list you all. Giulia Corniani, we have not spend a huge amount of time together in place, but we have shared tons of talks (sicentific and personal), and you are not only my collaborator, but a friend forever. Alex Tlaie, I have learnt tons of things from you, you have pushed me to evolve and to be a new person, which I am proud of, but what is more important is the passion we share, food. Michele Mastella, we started this journey together, and with Giulia, we pushed Neutouch to be what it is now since the beginning. Pablo Martínez, for being the ground truth knowledge in the surroundings, and for showing me that being a great scientist does not mean investing your whole time in science. Roberto Maffulli, for the time you spent on teaching me things that I did not know, and all the whole afternoons and evenings we spent discussing how to approach problems. Last, but not least, Alex Pequeño, because despite belonging to the same lab and not having performed science together, we had many discussions about science that ended up with productive ideas, and what is more important, also with food.

# Abstract

Objective: Traditional theories in neuroscience state that tactile afferents present in the glabrous skin of the human hand encode tactile information following a submodality segregation strategy, meaning that each modality (eg. motion, vibration, shape, ... ) is encoded by a different afferent class. Modern theories suggest a submodality convergence instead, in which different afferent classes work together to capture information about the environment through tactile sense. Typically, studies involve electrophysiological recordings of tens of afferents. At the same time, the human hand is filled with around 17.000 afferents. In this thesis, we want to tackle the theoretical gap this poses. Specifically, we aim to address whether the peripheral nervous system relies on population coding to represent tactile information and whether such population coding enables us to disambiguate submodality convergence against the classical segregation.

Approach: Understanding the encoding and flow of information in the nervous system is one of the main challenges of modern neuroscience. Neural signals are highly variable and may be non-linear. Moreover, there exist several candidate codes compatible with sensory and behavioral events. For example, they can rely on single cells or populations and also on rate or timing precision. Information-theoretic methods can capture non-linearities while being model independent, statistically robust, and mathematically well-grounded, becoming an ideal candidate to design pipelines for analyzing neural data. Despite information-theoretic methods being powerful for our objective, the vast majority of neural signals we can acquire from living systems makes analyses highly problem-specific. This is so because of the rich variety of biological processes that are involved (continuous, discrete, electrical, chemical, optical, ...).

Main results: The first step towards solving the aforementioned challenges was to have a solid

methodology we could trust and rely on. Consequently, the first deliverable from this thesis is a toolbox that gathers classical and state-of-the-art information-theoretic approaches and blends them with advanced machine learning tools to process and analyze neural data. Moreover, this toolbox also provides specific guidance on calcium imaging and electrophysiology analyses, encompassing both simulated and experimental data.

We then designed an information-theoretic pipeline to analyze large-scale simulations of the tactile afferents that overcomes the current limitations of experimental studies in the field of touch and the peripheral nervous system. We dissected the importance of population coding for the different afferent classes, given their spatiotemporal dynamics. We also demonstrated that different afferent classes encode information simultaneously about very simple features, and that combining classes increases information levels, adding support to the submodality convergence theory. Significance: Fundamental knowledge about touch is essential both to design human-like robots exhibiting naturalistic exploration behavior and prostheses that can properly integrate and provide their user with relevant and useful information to interact with their environment. Demonstrating that the peripheral nervous system relies on heterogeneous population coding can change the designing paradigm of artificial systems, both in terms of which sensors to choose and which algorithms to use, especially in neuromorphic implementations.

**Keywords:** information theory · neural coding · population coding · touch · peripheral nervous system · calcium imaging

# Contents

# List of Figures

# List of Tables

# Introduction

## 1 Preface

The human brain is one of the most complex and enigmatic structures in the known universe. Comprised of approximately 100 billion neurons and trillions of supporting glial cells, the brain is responsible for regulating our most basic physiological functions and for enabling us to experience the world around us through our senses, think, feel, and make decisions. Despite decades of research, scientists are still grappling with many of the mysteries of the brain and how it works.

Neurons, the basic building blocks of the brain, are the primary cellular components responsible for transmitting information from one part of the brain to another. They are specialized cells that receive and transmit signals via their dendrites, which receive inputs from other neurons, and their axons, which send outputs to other neurons. Neurons communicate with each other through chemical signals called neurotransmitters and electrical signals known as action potentials.

Over the past few decades, advances in technology and techniques have made it possible to study the brain and its functions at an unprecedented level of detail. However, despite this progress, there is still much that we do not understand about the workings of the brain and its neurons. For example, the mechanisms behind learning and memory, the generation of conscious thought, and the way in which populations of neurons integrate and process information for perception are still largely unknown. The computations and information processing steps needed for perception can be broken into several elementary computations throughout the nervous system. The most important ones are sensory coding and choice coding [1].

Sensory coding is essential for organisms to perceive their environment, since it is the

computational process that translates external stimuli into neuronal language. It consists of three different essential subtasks: reception, transduction, and coding. Reception occurs when a receptor is stimulated by some kind of physical energy such as tactile pressure or a photon delivering energy in the retina. Reception is followed by transduction, in which the physical energy is then converted into electrochemical energy. Finally, the coding part corresponds to a mapping between the attributes of the stimuli and the attributes of neural activity (e.g firing rate).

Choice coding is the second elementary computation related to the perception process. In this procedure, neurons carry information in the shape of action potentials (APs), which is then transformed into actions. As it happens with the sensory coding process, there also exists a mapping between the neural code and the behavioral choice that the organisms finally execute.

How and how well neural sensory coding informs behavioral choices also has a remarkable importance. Our senses can capture a lot of information from the external world, but not all that information is actually processed by the central nervous system. However, what we can say is that not only the brain, but also individual or groups of neurons, can be understood as a communication system that sends and process information coming from the senses to shape actions.

## 1.1 The sense of touch

Humans and animals perceive their environment through five different senses: sight, taste, touch, hearing and smell. The sense of touch is a fundamental aspect of human experience and plays a critical role in our perception of the world around us. From the sensations of pressure, temperature, and texture, to the emotional and social aspects of touch, this sense provides us with a wealth of information that helps us interact with our environment and others. Despite its importance, the scientific understanding of touch has lagged behind that of other senses, such as vision and hearing. However, in recent years, there has been a resurgence of interest in this field, driven by advances in neuroscience, psychology, and engineering.

The sense of touch begins with the activation of sensory receptors in the skin, which send signals to the central nervous system to create the perception of touch. In this section of the thesis, we will examine the neural mechanisms underlying touch perception, by investigating the structure

and function of sensory receptors, the pathways that transmit touch signals from the skin to the brain, and the neural circuits involved in processing touch information. Touch perception is not just a simple matter of sensory signals from the skin to the brain. It is also influenced by a variety of cognitive, emotional, and cultural factors, which shape our experiences of touch.

Despite its importance, the scientific understanding of touch has lagged behind that of other senses, such as vision and hearing. This might have happened for limitations on how we study the sense of touch. Unlike other senses, touch is not isolated in compact structures within the body. The sense of touch is present in our whole skin [2]. Plus, it does not only depend on the receptors on the skin, but also receptors located in the muscles, joints, tendons, and on the surface of internal organs [3]. However, in recent years, there has been a resurgence of interest in this field, driven by the potential applications that can be done in the fields of robotics and prosthetics due to the advances in engineering and technology.

Richard Feynman said once: *What I cannot create, I do not understand*. At the present time, we cannot say that we have been able to produce robots exhibiting a tactile sense like humans, neither a prosthetic device that perfectly replaces and integrates a body limb. My personal interpretation of this sentence implies that, for being able to produce such devices, we really need to dig in the biological principles underlying touch, to understand which of them are enough relevant to be used in artificial. And all this starts with the understanding of the encoding mechanisms of the tactile afferent innervating the skin.

## 1.2 Information Theory

Information theory (IT) has emerged as a powerful tool in the field of neuroscience, providing a mathematical framework for understanding the complex processes of sensory processing, coding, and decision making in the brain. Information theory was originally developed by Claude Shannon in 1948 as a way to quantify the amount of information transmitted in communication systems [4]. However, the principles of information theory have since been applied to a wide range of fields, including physics, biology, and psychology. In neuroscience, information theory has been key to analyze the properties of neural signals, to understand the mechanisms of sensory coding, sensation, spatial navigation, and to study the process of decision making in the brain [5–8].

One of the key ideas in information theory is the concept of entropy, which measures the uncertainty or randomness of a system. In the context of neuroscience, entropy has been used to analyze the distribution of neural firing rates, to quantify the variability of sensory responses, and to assess the information content of neural signals. Another important concept in information theory is mutual information, which measures the amount of information that is shared between two variables. In neuroscience, mutual information has been used to study the relationship between neural activity and behavioral responses (or given stimuli), to analyze the structure of functional networks in the brain, and to explore the dynamics of neural interactions.

Information theory is then one of the disciplines that can help to shed light on how neural systems integrate, encode and compute information, and it is and ideal candidate to understand the nervous systems for being statistically robust, mathematically well-grounded, and model independent, meaning that analyses on how neurons (or brain areas, among others) encode and transmit information can be done in an assumption-free way. Additionally, IT can capture both linear and non-linear interactions that can define coding mechanisms [1, 9].

## 2 Research goals

The main objective of this thesis aims at understanding the sensory encoding mechanisms of the tactile afferents present in the skin of the human hand by means of applying information theoretic methods. Such question brought us to divide the development of this project into two to different stages based on more defined and bounded questions that are written below.

The advantages that make information theory a powerful an ideal candidate to analyze neural signals were clearly stated in the previous section. Even if the methods can be generally applied to any kind of data, its application remains very problem specific due to the huge types of neural data we can record [9]. There exist several methods that can be used to understand the flow of information and that can be combined with both supervised and unsupervised machine learning techniques to deal with very large datasets [7, 10, 11]. Precisely listing the advantages and limitations of the different methods implies a proper definition of the adequation of each of them based on the type of neural data we need to analyze. For this reason we defined a first Research Question (RQ) as follows:

**RQ1:** *Which are the most useful information theoretic methods depending on the type of neural signals we record and what are their limitations and advantages?*

Once having defined a proper methodology to deal with different types of neural signals, we can focus on the understanding of the sensory coding strategies of the tactile afferents. Two types of data can be used for such a purpose.

First, neurophysiological recordings, that suffer from strict limitations in terms of the time required to prepare participants and typically only a handful of afferents can be recorded simultaneously, while we do know that the human hand gathers around 17.000 [12]. Second, computational models [13], that can be less precise or constrained to the specific conditions in which the data for the training was obtained. The main advantage of computational models is that they are not subject to the experimental limitations. Literature has focused on describing the coding mechanisms based on such recordings. However, population coding has been rarely investigated [14], discarding the possibility of tactile afferents relying on population strategies to encode stimulus information [7, 15]. On the other, hand, the fact of using a small sample of the whole population might have led experimental studies to biased conclusions about the sensory coding procedure. Considering this gap, we defined the second research question as:

**RQ2:** *Do tactile afferents rely on population coding strategies to encode stimulus information?*

# 3 Contributions

Two different self-standing studies have been gathered in this manuscript and the specific scientific contributions to this thesis are broadly discussed in the corresponding chapters.

Both studies together add knowledge the study of neural coding. The first study adds knowledge about very powerful methods (information theory) to understand neural coding in general, independently of the type of neural signal that can be recorded from the nervous system, and providing guidance are suggestions under specific conditions that scientists can find during their experiments. This study not only added theoretical knowledge about neural coding, but also a publicly available toolbox that aims to facilitate the use of computational methods to neuroscientists (in particular, experimental ones). The second study scaled the methods included

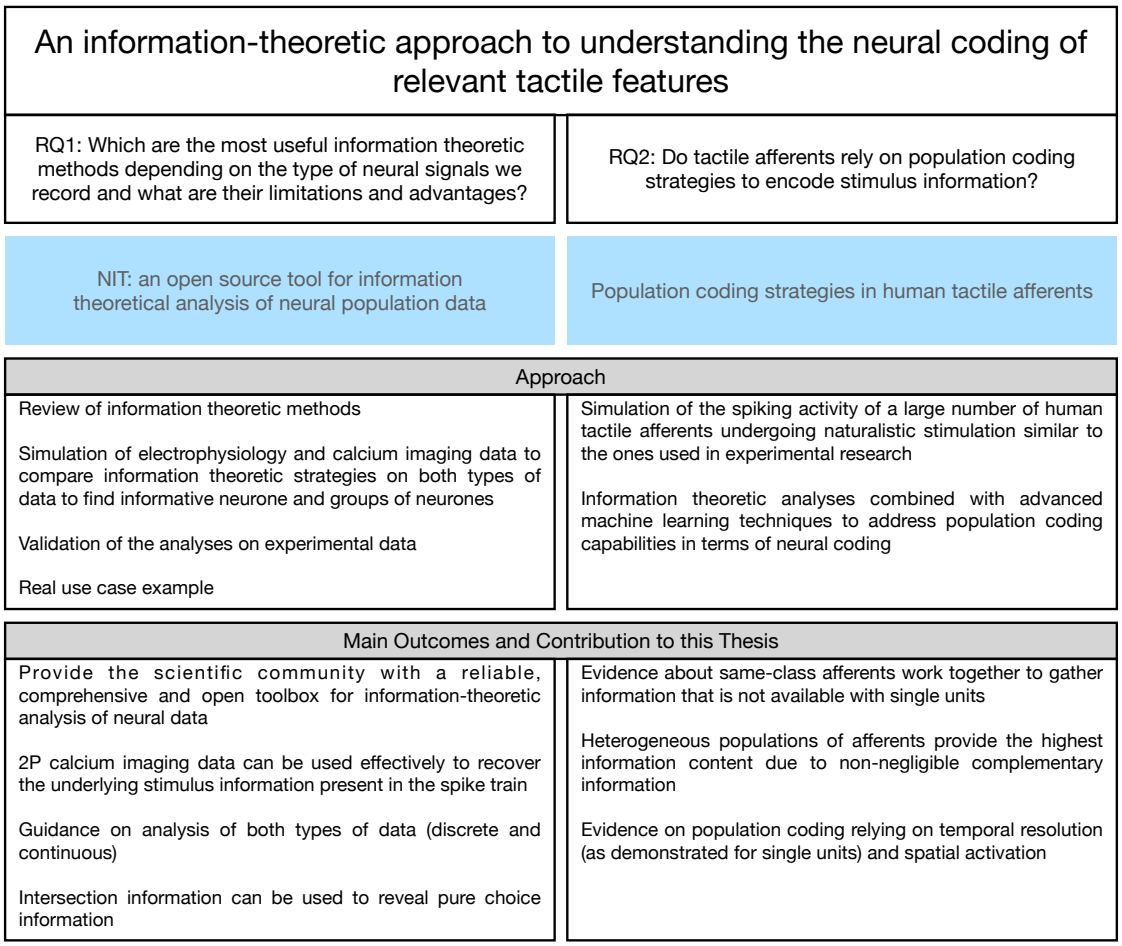


**Fig. 1:** Overview of the research questions, approaches, and contributions of the manuscript. Two questions constitute the objective of the thesis, the diagram provides an overview of the approaches and the resulting scientific contributions.

in the toolbox to analyze the encoding of information by the human tactile afferents from a population coding perspective, that was rarely investigated, probably due to the large number of afferents that we can find only in the hand, unveiling basic knowledge about tactile coding that can guide the design of future neuromorphic-embedded systems on prosthetics and robotics

In Figure 1, we offer an overview of the research questions, the studies' approach and the main scientific contributions.

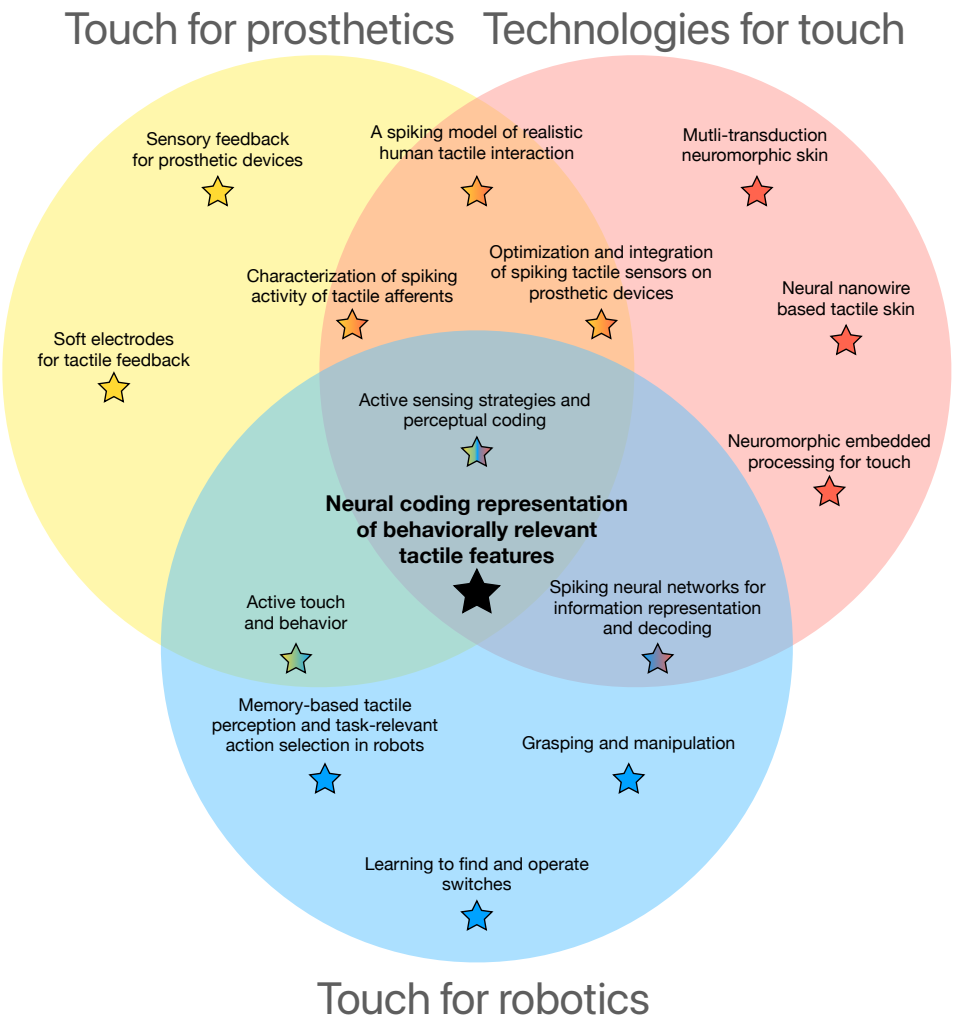


**Fig. 2:** Neutouch organization in working packages including the contributions of the researchers.

# 4 Research in context

The research presented in this manuscript was performed within the Innovative Training Network (ITN) of NeuTouch, a project supported by the European Union's Horizon 2020 Marie Skłodowska-Curie Actions (grant agreement 813713). 15 Early Stage Researchers (ESR) and 16 principal investigators build NeuTouch, including 9 different institutions across such as: universities, research institutes, and industrial companies.

The objective of Neutouch is improving artificial touch perception and hand prostheses by designing systems with bioinspired electronic circuits, known as neuromorphic computing. Artificial systems have reached even better results than structures that evolution has been shaping for millions of years, and the simplest example are the planes. However, we know that one of the optimisation that evolution performs is energy consumption, or what is the same, efficiency. If we want to produce systems that work well and with a low energy consumption, looking at biological systems is the most straightforward way to reach such objective. Following this insight, we may be able to create not only robots that achieve a more human behavior, but also prostheses exhibiting a better human-machine integration providing then the user with a more realistic and intuitive experience (e.g. in terms of perception or feedback), which could be crucial to improve the user's abilities and precision.

With this aim Neutouch was organized as a multidisciplinary project divided into three different overlapping topics that give rise to three different working packages: Technologies for Touch, Touch for Robotics, and Touch for Prosthetics (see Figure 2).

Technologies for Touch aims at developing neuromorphic tactile sensors with low-energy consumption that can still correctly mimic the function of tactile afferents together with spiking neural networks that can encode information in following the neural codes of the peripheral nervous system. More specifically, this working package aims at developing nanowires and materials for smart transduction that are able to reproduce the dynamics of the human tactile afferents to integrate them in neuromorphic circuits. Then, understanding the neural encoding of tactile features is essential for such investigations.

The neural encoding of tactile features and their neural representations are also basic to define

robotic behavior policies. Touch for Robotics is precisely focused in generating autonomous grasping and object recognition algorithms, among other active touch related actions, by integrating the information obtained from the neuromorphic mechanoreceptors. The close-loop between sensory perception and behavior, makes the understanding of tactile encoding a crucial step to define proper decision-making and behavior policies. In this context, the aim of the working package is to define algorithms that perform proper object grasping and manipulation with the information provided by the tactile sensors.

Touch for Prosthetics is the working package that is focused more on the health field, aiming at developing functional replacement of missing limbs in humans. Some preliminary results showed how, by means of surgical implants in the peripheral nerves, the flow of tactile information could be restored such that it could arrive from a hand prosthesis to the central nervous system. Following this insight, the questions that Neutouch wants to address in this context is how to define more natural stimulation strategies for the proper encoding of tactile features and the development of biocompatible and resistent active materials that can act as a neural interface between artificial systems and the peripheral nervous system.

As mentioned before, these three different areas overlap between each other. This is the main reason causing for the knowledge generated in each of them being of the utmost importance for the remaining two. In fact, the research project producing this manuscript, is at the core of the three different research topics (see Figure 2), being a key part for Neutouch, and providing with useful tools and insights to other fellows' projects.

The second chapter in this manuscript gathers the work in the paper "Population coding strategies in human tactile afferents" and arises from the collaboration with Giulia Corniani and her supervisor, Hannes P Saal, from the Active Touch Laboratory in Sheffield. The valuable knowledge they had about existing literature in tactile coding for the peripheral nervous system in combination with the knowledge we provided to extract information about neural signals, we managed to produce a novel study characterizing population coding strategies of human tactile afferents. This study served as a basis for working on neuromorphic tactile sensors that significantly rely on fundamental understanding about the underlying biological processes.

Neutouch was also an environment providing ESRs with several training opportunities and

resources. During the development of the project, three international summer schools were organized and soft-skills courses addressing transversal needs for science were provided to the PhD students. Additionally, we were involved in the organization of the events of a Horizon project and the planification of deliverables and plans that have to be delivered to the EU, providing the students not only with theoretical soft-skills knowledge, but also with an important pragmatical part that can help us both in industry or academia.

# 5 Manuscript structure

This manuscript gathers the investigation carried in a manuscript format. Therefore, the following chapters consist of papers in a form suitable for publication in a peer-reviewed journal. The current chapter connects the three works and discusses their coherence and significance. Each of the following chapters is a complete and self-standing piece of work. The last chapter of this manuscript is focused on the impact of the research and the questions that should be addressed in future work.

Paper 1 addresses the RQ1 and consists of the preprint "NIT: an open-source tool for information theoretic analysis of neural population data" which was published currently available in biorxiv [16]. An alternative version of this manuscript is currently being prepared for the submission to the journal PLOS Computational Biology as a Software Article. In parallel, this research has produced both an information theoretic toolbox [17] and a calcium imaging simulator [18] hat are currently publicly available to download for the scientific community. This work was carried as an internal collaboration with Roberto Maffulli, a PostDoc in the Neural Computation Laboratory. Preliminary results of this work were presented as a poster in the FENS Forum 2022 in Paris.

Paper 2 addresses RQ2 and consists of the journal paper "Population coding strategies in human tactile afferents" which has been published in the journal PLOS Computational Biology the 7th December 2022 (the first submission in the same journal was on the 15th of June 2022). Note that the article is open-access. This work is the result of a close collaboration with Giulia Corniani (ESR of the NeuTouch ITN) and Prof. Hannes P Saal. The study started in November 2020 with a two months secondment of Giulia Corniani at the Laboratory of Neural Computation and finished with the secondment of the author of this manuscript to the Active Touch Laboratory

in the University of Sheffield, led by the Prof. Hannes P Saal. Partial or preliminary results of this work were presented at several international conferences and workshops (IEEE NER2021, 50th annual meeting of the Society of Neuroscience, BARCCSYN 2021, and Neuromatch 2021 conference).

# 6 Covid-19 statement

The PhD project summarized in this manuscript was started in November 2019. The Covid-19 pandemic outbreak occured less than 6 months after, affecting the project management of the whole Neutouch network, including this project.

Neutouch launched a contigency plan to facilitate the PIs and students the development of their work minimizing the impact and avoiding significant delays due to the effect of restrictions limiting traveling to other laboratories and perform collaborations. To do so, online meetings and training events were organized to embrace the collaborations between different partners and facilitate the discussion of main topics that Neutouch was focused on.

The main limitation caused to this project is from the experimental point of view. The data majority of data included in this manuscript is either simulated or old datasets. However, due to the restrictions, experimental partners in Neutouch were not able to provide the rest with novel experiments that could be analyzed on time.

As soon as most travel restrictions were lifted and in-person events started to be organized again, we also embraced all the opportunities to engage with the scientific community and disseminate the work. This included the participation in the BARCCSYN 2021 (Barcelona, Spain), European Researchers Night (September 2021, Genova, Italy), FENS Forum 2022 (July 2022, Paris, France), International School on Technologies for Touch (September 2022, Arenzano, Italy) and other NeuTouch training and local events.

# References


[1] S. Panzeri, C. D. Harvey, E. Piasini, P. E. Latham, and T. Fellin, "Cracking the neural code for sensory perception by combining statistics, intervention, and behavior," *Neuron*, vol. 93, no. 3, pp. 491–507, 2023/02/04 2017. [Online]. Available: https://doi.org/10.1016/j.neuron.2016.12.036

[2] Y. Gilaberte, L. Prieto-Torres, I. Pastushenko, and Á. Juarranz, "Chapter 1 - anatomy and function of the skin," in *Nanoscience in Dermatology*. Academic Press, Jan. 2016, pp. 1–14.

[3] M. L. Zimny, "Mechanoreceptors in articular tissues," *Am. J. Anat.*, vol. 182, no. 1, pp. 16–32, May 1988.

[4] C. E. Shannon, "A mathematical theory of communication," *The Bell system technical journal*, vol. 27, no. 3, pp. 379–423, 1948.

[5] A. G. Dimitrov, A. A. Lazar, and J. D. Victor, "Information theory in neuroscience," *Journal of computational neuroscience*, vol. 30, no. 1, pp. 1–5, 2011.

[6] A. Borst and F. E. Theunissen, "Information theory and neural coding," *Nature Neuroscience*, vol. 2, no. 11, pp. 947–957, 1999. [Online]. Available: https://doi.org/10.1038/14731

[7] R. Quian Quiroga and S. Panzeri, "Extracting information from neuronal populations: information theory and decoding approaches," *Nat. Rev. Neurosci.*, vol. 10, no. 3, pp. 173–185, Mar. 2009.

[8] A. Fairhall, E. Shea-Brown, and A. Barreiro, "Information theoretic approaches to understanding circuit function," *Current Opinion in Neurobiology*, vol. 22, no. 4, pp. 653–659, 2012. [Online]. Available: https://www.sciencedirect.com/science/article/pii/S0959438812001043

[9] N. M. Timme and C. Lapish, "A Tutorial for Information Theory in Neuroscience," *eNeuro*, vol. 5, no. 3, May 2018. [Online]. Available: https://www.eneuro.org/content/5/3/ENEURO.0052-18.2018

[10] A. Onken, J. K. Liu, P. P. C. R. Karunasekara, I. Delis, T. Gollisch, and S. Panzeri, "Using matrix and tensor factorizations for the Single-Trial analysis of population spike trains," *PLoS Comput. Biol.*, vol. 12, no. 11, p. e1005189, Nov. 2016.

[11] C. A. Runyan, E. Piasini, S. Panzeri, and C. D. Harvey, "Distinct timescales of population coding across cortex," *Nature*, vol. 548, no. 7665, pp. 92–96, 2017.

[12] G. Corniani and H. P. Saal, "Tactile innervation densities across the whole body," *J. Neurophysiol.*, vol. 124, no. 4, pp. 1229–1240, Oct. 2020.

[13] H. P. Saal, B. P. Delhaye, B. C. Rayhaun, and S. J. Bensmaia, "Simulating tactile signals from the whole hand with millisecond precision," *Proceedings of the National Academy of Sciences*, vol. 114, no. 28, pp. 201 704 856–201 704 856, Jun. 2017.

[14] A. W. Goodwin and H. E. Wheat, "Sensory signals in neural populations underlying tactile perception and manipulation," *Annu. Rev. Neurosci.*, vol. 27, pp. 53–77, Dec. 2004.

[15] V. E. Abraira and D. D. Ginty, "The sensory neurons of touch," *Neuron*, vol. 79, no. 4, pp. 618–639, Aug. 2013.

[16] R. Maffulli, M. A. Casal, M. Celotto, S. Zucca, H. Safaai, T. Fellin, and S. Panzeri, "Nit: an open-source tool for information theoretic analysis of neural population data," *bioRxiv*, 2022. [Online]. Available: https://www.biorxiv.org/content/early/2022/12/13/2022.12.11.519966

[17] R. Maffulli and M. A. Casal, "Nit: Neuroscience information toolbox," 12 2022. [Online]. Available: https://gitlab.com/rmaffulli/nit

[18] R. Maffulli, "Casim: realistic calcium imaging simulator," 12 2022. [Online]. Available: https://gitlab.com/rmaffulli/casim

# NIT: an open-source tool for information theoretic analysis of neural population data

R. Maffulli, **M. A. Casal**, M. Celotto, S. Zucca, H. Safaai, T. Fellin, S, Panzeri "NIT: an open-source tool for information theoretic analysis of neural population data," *bioRxiv 2022.12.11.519966*

DOI: https://doi.org/10.1101/2022.12.11.519966

Keywords: *information theory* | *calcium imaging* | *neural coding* | *electrophysiology*

This chapter consists of a biorxiv version of a manuscript, published to receive feedback while we are currently working to evaluate the work needed for submission to a journal.

## Candidate's contribution to the paper

**Conceptualization:** Roberto Maffulli, **Miguel A. Casal**, Stefano Panzeri

**Data Curation:** Roberto Maffulli, **Miguel A. Casal**, Stefano Zucca

**Formal analysis:** Roberto Maffulli, **Miguel A. Casal**

**Funding acquisition:** Roberto Maffulli, Tommasso Fellin, Stefano Panzeri

**Investigation:** Roberto Maffulli, **Miguel A. Casal**, Stefano Zucca

**Methodology:** Roberto Maffulli

**Software:** Roberto Maffulli, **Miguel A. Casal**, Marco Celotto

**Validation:** Roberto Maffulli

**Visualization:** Roberto Maffulli, **Miguel A. Casal**

**Supervision:** Tommasso Fellin, Stefano Panzeri

**Writing – original draft:** Roberto Maffulli, **Miguel A. Casal**, Stefano Panzeri

**Writing – review & editing:** Roberto Maffulli, **Miguel A. Casal**, Marco Celotto, Tommasso Fellin, Stefano Panzeri

## Abstract

Information theory provides a popular and principled framework for the analysis of neural data. It allows to uncover in an assumption-free way how neurons encode and transmit information, capturing both linear and non-linear coding mechanisms and including the information carried by interactions of any order. To facilitate its application, here we present Neuroscience Information Toolbox (NIT), a new toolbox for the accurate information theoretical analysis of neural data. NIT contains widely used tools such as limited sampling bias corrections and discretization of neural probabilities for the calculation of stimulus coding in low-dimensional representation of neural activity (e.g. Local Field Potentials or the activity of small neural population). Importantly, it adds a range of recent tools for quantifying information encoding by large populations of neurons or brain areas, for the directed transmission of information between neurons or areas, and for the calculation of Partial Information Decompositions to quantify the behavioral relevance of neural information and the synergy and redundancy among neurons and brain areas. Further, because information theoretic algorithms have been previously validated mainly with electrophysiological recordings, here we used realistic simulations and analysis of real data to study how to optimally apply information theory to the analysis of two-photon calcium imaging data, which are particularly challenging due to their lower signal-to-noise ratio and temporal resolution. We also included algorithms (based on parametric and non-parametric copulas) to compute robustly information specifically with analog signals such as calcium traces. We provide indications on how to best process calcium imaging traces and to apply NIT depending on the type of calcium indicator, imaging frame rate and firing rate levels. In sum, NIT provides a toolbox for the comprehensive and effective information theoretic analysis of all kinds of neural data, including calcium imaging.


## 1 Introduction

Information theory (IT), is the principled mathematical theory of communication [19]. Its use as analysis tool to measure how neurons encode and transmit information has been key to understanding brain functions such as sensation, spatial navigation, and decision-making. Mutual information (MI), the key quantity of IT, measures how well variables important for cognitive

functions, such as sensory stimuli, are encoded in the activity of neurons, and how information is transmitted across brain regions. Its use has many advantages [20–26]. It provides a single-trial measure of information encoding and it is thus more relevant for single-trial behavioral or perceptual functions than trial-averaged measures of discriminability. It quantifies information in units of bits, a meaningful and interpretable uncertainty-reduction scale. It allows largely hypotheses-free measures of information encoding that place upper bounds to the performance of any decoder, and that can potentially capture the contributions of both linear and non-linear interactions between variables at all orders. Because of its generality, it can be applied to any type of brain activity recordings. Also, because neural systems may need to maximize information encoding for evolutionary reasons, applications of IT to empirical data allows a direct comparison between the predictions of normative neural theories and real neural data [5, 9]. Because of these advantages, information theory has deeply influenced neuroscience over many years [23, 25, 27–31].

Earlier work using information theory to analyze empirical neuroscience data has focused on low-dimensional measures of neural activity such as single neurons, small neural populations or aggregate measures such as LFPs/EEGs (because of the systematic errors in estimating information with the small numbers of trials that can be collected empirically are exacerbated with high-dimensional neural responses [32]). It has also focused mostly on information encoding, regardless of the downstream use of the encoded information. Seminal studies of this kind have used electrophysiological recordings of neural activity to demonstrate the role of single-neuron spike timing for the encoding of sensory information [24, 25, 33–35]. Other studies have provided the foundations of how trial-to-trial correlations between neurons shape the encoding of information and create redundancy and synergy in pairs of neurons [36–38]. Further studies have examined how information is encoded in the neural oscillations found in aggregate measures of neural activity such as Local Field Potentials (LFPs) [39, 40]. Several algorithms have been proposed for the application of IT to these low-dimensional neural data [24, 41, 42]. Their ability to provide accurate and data-robust information estimates has been extensively validated and demonstrated on electrophysiological recordings, including on spike trains of small populations and on LFPs and EEGs [42–45], and their use and dissemination has been aided by software toolboxes [43, 46–49].

Over the last decade, due to major progress in the simultaneous recording from many neurons and/or brain areas, and in the measure and quantification of behavior [50], neuroscience research [51–53] – and consequently neuroscientific IT – has evolved to investigate how behavior and information processing emerge from the interaction and communication between neurons and across brain areas. For example, recent work has coupled IT with dimensionality-reduction techniques to study how information is encoded in populations of tens to hundreds of neurons [54–63], and of how patterns of synergy between pairs of neurons are organized within larger networks [38]. Studies have also characterized the transfer of information between neural populations [64, 65] and between brain areas [66–68]. Importantly, neuroscientific IT has also been used to measure the information carried by neural activity not only about sensory stimuli, as in traditional studies, but also about behaviorally relevant signals such as choice and reward [62]. Moreover, Partial Information Decompositions (PID) [69] has extended Shannon's IT to quantify how much of the information encoded in neural activity is used to inform behavioral choices during perceptual discriminations [70, 71] and synergistic or redundant transfer of information across brain regions [66]. However, progress in using latest IT advances in neuroscience to address large populations, behavioral relevance and information transmission, synergy and redundancy with PID, has been slowed by the absence of comprehensive toolboxes including all or most these recent tools.

Key to the recent progress in understanding the relevance of neural population activity for behaviors has been the application of 2-Photon (2P) fluorescence microscopy [72–74] to image the activity of populations of neurons in animals performing cognitive tasks [75–80], even over days or months [81–85]. However, applying information theory to 2P imaging recordings is particularly challenging. 2P calcium imaging measures neural activity only indirectly (by the optically recorded fluorescence signal changes that originate from changes in calcium concentrations related to changes in neural activity), and it generally has low SNR and limited temporal resolution. Understanding how to optimize the use of information theory to analyze large-scale recordings of populations with 2P imaging during behavior would greatly aid progress in studying neural population coding.

Here, we introduce the Neuroscience Information Toolbox (NIT) to specifically address both the need of having a single open-source toolbox including many recent advances in IT tools for

neuroscience and of optimizing its use for 2P calcium imaging. NIT provides a comprehensive set of IT tools (including MI, directed communication measures, PID tools, binned and copula probability estimators, and limited sampling bias corrections) applicable to both discrete and continuous measures of neural activity. It thus can be used with both direct electrophysiological recordings of action potentials and with indirect measures of neural activity, such as LFP, EEG, fMRI and 2P imaging. Algorithms that we implemented and optimized in NIT were already validated on electrophysiological recordings [43–45]. However, here we study extensively, both with realistic simulations and with analysis of real data, how best to extract from 2P imaging data information about variables of interest (sensory stimuli, behavioral choice, and/or the underling firing levels of neurons) and how best to tune algorithms for information measures and for calcium imaging processing depending on factors including imaging frames, calcium indicators, signal-to-noise ratio of fluorescence and neural firing regimes.

# 2 Results

## 2.1 NIT: a complete toolbox for information theoretical analysis of neural data

We present NIT, the Neuroscience Information Toolbox. NIT is a comprehensive package of open-source tools for information-theoretical analysis of neuroscience data. NIT is fully documented, and its MATLAB interface allows easy integration with custom built analysis pipelines.

Features and structure of NIT are shown in Figure 3. At the core of the software sits a set of modules for the calculation of information theoretic quantities. The software consists also of a set of routines for applying dimensionality reduction and neural decoding strategies. Some of the computations are performed through ad-hoc developed interfaces to external libraries which are distributed with the code, making NIT a self-contained toolbox. The key features and functions of the software are briefly described in the following sections.

In the following, we first list and explain the various information theoretic functions and features included in the toolbox. We then introduce the detailed simulations of 2P calcium imaging recordings together with the results of the parametric study used to discuss the limitations of extracting information from those data as opposed to electrophysiology. Finally, we apply NIT to

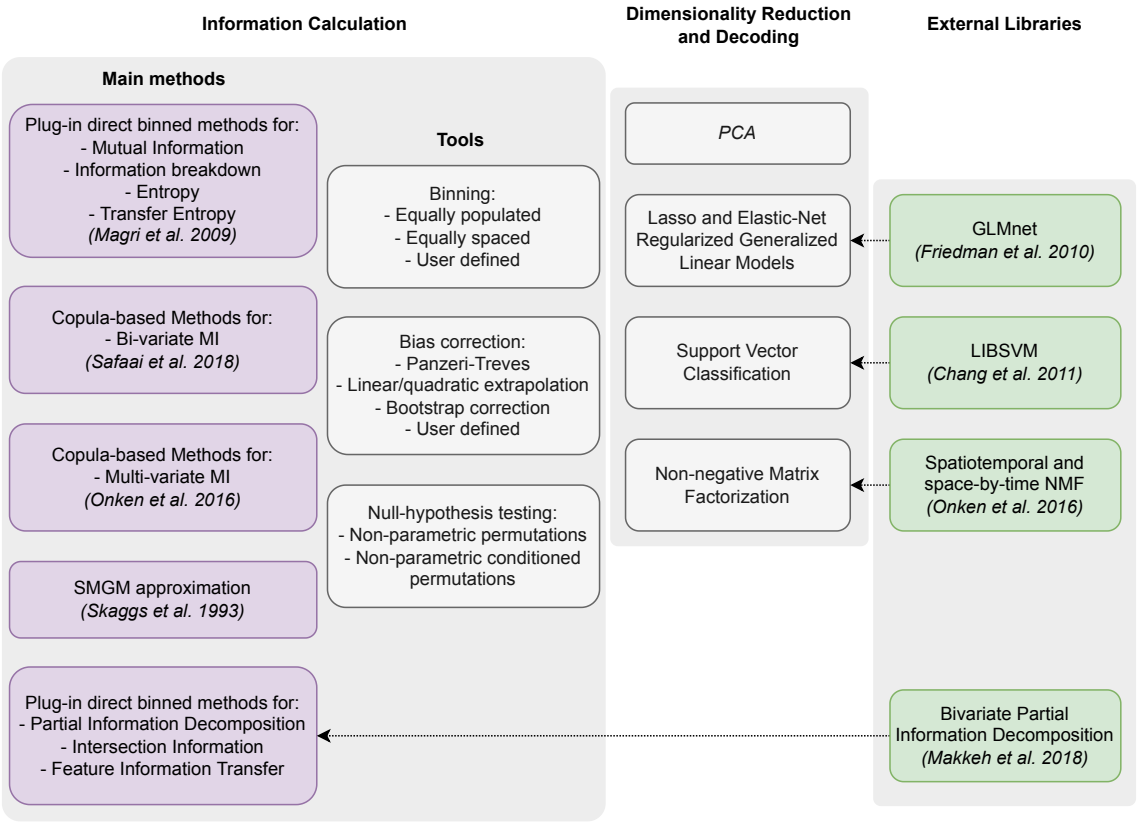


**Fig. 3: Structure of Neuroscience Information Toolbox (NIT).** The toolbox comprises modules (black boxes) for calculation of information-theoretic quantities and dimensionality reduction. External libraries (green boxes) are interfaced (arrows) with some of NIT native modules to integrate their functionalities.

experimental data, first to validate what we have observed on synthetic data, as well as to illustrate how the methods implemented in NIT can be effectively used to reveal a higher level of detail of the information processing principles in the brain.

## 2.2 Information theoretic algorithms and functions implemented in NIT

### 2.2.1 Mutual Information

MI between two random variables $R$ (in this example the neuronal response) and $S$ (in this example an external stimulus) measures how well a single-trial knowledge of one variable reduces our uncertainty about the value of the other variable is defined as follows [19]:

$$MI(R;S) = \sum_{r\in R, s\in S} p(r,s)\log_2\left(\frac{p(r,s)}{p(r)p(s)}\right) \quad (1)$$

where $p(r, s)$ is the joint probability of observing in a given trial stimulus $s$ and response $r$, and $p(s)$, $p(r)$ are the corresponding marginal probabilities. $MI(R; S)$ is measured in units of bits, it is non-negative, and it is zero if and only if $S$ and $R$ are statistically independent. One bit of information means that the knowledge of one variable halved the uncertainty about the other variable. $R$ can be either univariate (e.g. time-averaged single neuron activity) or multivariate (e.g. neural population activity, with each dimension of $R$ quantifying the activity of each neuron in a population). NIT accepts either univariate or multivariate entries for both responses and stimuli (useful when several stimulus features are varied across trials). The value of MI is computed once these probabilities are measured from the data over repeated experimental trials and inserted into Equation 1. Different methods to compute MI from real data typically differ depending on how these probabilities are estimated from the data. Three different MI calculation methods are provided in NIT.

The first one, the direct or plug-in method, consists in estimating the probabilities in Equation 1 by simply counting the number of occurrences of the discrete values of both $R$ and $S$ across repeated presentations of the stimulus. The plug-in method does not make assumptions on the shape of the probability distributions and has a low computational cost. To make the plug-in method applicable to cases in which $R$ and/or $S$ are continuous (e.g. $R$ will be continuous if is extracted from unprocessed 2P calcium traces or from LFP traces), NIT has two built-in discretization functions, that bin data in equally-populated or equally-spaced classes. Equally-populated binning maximizes the entropy available in the neural response for a given number of bins and thus often leads to larger information values, whereas equally-spaced binning preserves the shape of the original probability distribution. An interface is provided for inserting into the workflow other user-defined binning methods.

A second method, applicable only when the underlying distributions of the data are Gaussian, relies on fitting a Gaussian probability density function to the data. This method, suitable for continuous data not discretized in post-processing, is less prone to limited sampling bias (see below) than the direct plug-in method. However, it is applicable only when signals are approximately Gaussian. This may hold in specific instances for aggregated electrical signals (LFP, EEG, MEG) [39, 43, 47], but it does not hold for 2P calcium traces of individual cells [86].

Finally, NIT implements also a Copula estimator, including both parametric Copulas [47, 87] and Non-Parametric Copula (NPC) MI estimation [88]. Joint multi-dimensional probabilities distributions can be expressed in terms of marginal probabilities and a copula, a mathematical term that specifically describes the statistical dependences between the variables (see Materials and Methods). The MI between two variables depends on the copula but not on the marginal probabilities. This allows to estimate MI without calculating the latter [47, 87, 88]. In the NPC approach, copulas are estimated non-parametrically with Kernel methods rather than with parametric forms, allowing largely assumption-free information estimations and avoiding potential mis estimations of information due to wrong parametric assumptions being used [88]. Estimating MI with NPC has a much higher computational cost compared to the direct plug-in method, at the advantage of being more accurate and not requiring the discretization of continuous variables (although it can be applied also to discrete variables). As an alternative, we also implemented parametric copula estimator, which use parametric assumptions for the joint probability density estimators. This has an advantage in terms of computational costs but it may become highly inaccurate when the Gaussian assumptions are not met [88]. For continuous margins, we provide implementations of the normal and the gamma distributions. For discrete margins, we provide the Poisson, binomial and negative binomial distributions. As bivariate copula building blocks, we provide the Gaussian, student and Clayton families as well as rotation transformed Clayton families [87].

### 2.2.2 Mutual Information breakdown to quantify the information content of neuronal correlations

The information about the stimulus encoded in the activity of a population of individual neurons depends on the strength and structure of correlations among neurons [26, 52]. NIT allows to quantify how correlations affect neural population encoding of the stimulus by using the Information Breakdown formalism [37]. The MI between the stimulus and the neuronal population response $R$ (a multi-dimensional vector containing the activity of each neuron in a given trial) is divided in components that capture the different ways in which correlations affect neural population information, as follows:

$$MI(R;S) = MI_{\text{lin}} + MI_{\text{sig sim}} + MI_{\text{corr-ind}} + MI_{\text{corr-dep}} \quad (2)$$

where $MI_{\text{lin}}$, the linear term, is simply the sum of the $MI$ about the stimulus carried by the individual neurons. The other terms, capturing the differences between $MI(R;S)$ and $MI_{\text{lin}}$ reflect the effect of the statistical dependencies between neuronal responses. Such dependencies are traditionally conceptualized as signal correlations (correlations of the trial-averaged neural responses across different stimuli, quantifying the similarity of tuning to stimuli of different neurons) and noise correlations (correlations in trial-to-trial variability of the activity of different over repeated presentations of the same stimulus, quantifying functional interactions between neurons after discounting the effect of similarities in stimulus tuning), see e.g. [52, 89, 90]. The term $MI_{\text{sig sim}}$, always less than or equal to zero, quantifies the reduction of information (or increase in redundancy) due to signal correlations (that is, because neurons have partly similar response profiles to the stimuli). $MI_{\text{corr-ind}}$, a term that can be either positive or negative, quantifies the increment or decrement of information due to the relationship between signal correlation and noise correlation. The term is positive (providing synergy) if signal and noise correlations have opposite sign, while is negative (providing redundancy) if signal and noise correlations have the same sign [19]. $MI_{\text{corr-dep}}$ is a non-negative term that quantifies the information added by the stimulus modulations of noise correlations [37]. The information breakdown includes as a sub-case other types of decomposition and quantifications of the effect of correlations in population activity. For example, $MI_{\text{corr-ind}}$ + $MI_{\text{corr-dep}}$ quantifies the total effect of noise correlations on stimulus information and equals the quantity $\Delta I_{\text{noise}}$ defined in [91]. Similarly, $MI_{\text{lin}}$ + $MI_{\text{sig sim}}$ quantifies the information that the population would have if all single neurons properties were the same but noise correlations were absent, and equals the quantity $I_{\text{no-noise}}$ of [74]. Finally, $MI_{\text{corr-dep}}$ equals the quantity $\Delta I$ introduced in [92] as an upper bound to the information that would be lost if a downstream decoder of neural population activity would ignore noise correlations. The information breakdown formalism and the related quantities that can be obtained from it have been used in many studies to empirically characterize the effect of correlations [26, 34, 38, 55, 93–96].

### 2.2.3 Partial Information Decomposition

Other methods to decompose the contributions of multivariate dependencies between neurons to information carried by populations include the Partial Information Decomposition (PID) [69]. In the form implemented in NIT, PID is applied to three stochastic variables $(R_1, R_2, S)$ (e.g. two neurons with responses $R_1$ and $R_2$ respectively, and a stimulus variable $S$). The method decomposes the information that two of them (called source variables, in the example above the two neuronal responses) carry about the third one (called target variable, in the example above the stimulus), in four non-negative and well-interpretable terms called "atoms", as follows:

$$\begin{aligned} MI((R_1, R_2); S) =& SI((R_1, R_2); S) + CI((R_1, R_2); S) \\ &+ UI((R_1 \backslash R_2); S) + UI((R_2 \backslash R_1); S) \end{aligned} \tag{3}$$

In Equation 3: $SI((R_1, R_2); S)$ is the shared (redundant) information that $R_1$ and $R_2$ carry about $S$; $UI((R_1 \backslash R_2); S)$ is the unique information about $S$ that is carried by $R_1$ but is not carried by $R_2$; $UI((R_2 \backslash R_1); S)$ is the unique information about $S$ only present in $R_2$ but not in $R_1$; and $CI((R_1, R_2); S)$ is the complementary (synergistic) information about $S$ that is available only when $R_1$ and $R_2$ are measured simultaneously. NIT calculates the above PID three-variate decomposition using the so-called BROJA definition [97] through a specifically designed interface to the BROJA-2PID algorithm [98].

### 2.2.4 Intersection Information

One application of PID is the measure of Intersection Information ($II$, see [99, 100]). $II$ applies to tasks such as perceptual decisions in which in each trial a stimulus ($S$) is presented, neural activity ($R$) is recorded and the subject's perceptual report of which stimulus was presented is measured as a behavioral choice ($C$). $II$ measures, in bits, how much of the stimulus information carried by neural activity $MI(R; S)$ is used to inform the behavioral choice, and is defined in terms of PID as follows [100]:

$$II(S;R;C) = \min\left(SI((S,R);C), SI((C,R);S)\right) \tag{4}$$

As shown in Ref [100], this expression quantifies the part of information carried by neural activity that is shared between stimulus and choice, and that at the same time is part of the overall information between stimulus and choice. $II$ is non-negative, is bounded by the stimulus and choice information carried by neural activity, and by the information between stimulus and choice. $II$ has been used in several studied to determine the behavioral relevance of aspects of neural population codes (e.g. [56, 71, 100]). NIT has a specifically built module for the calculation of $II$ with the plug-in probability estimation method.

### 2.2.5 Measures of directed information transfer between neurons or brain regions

NIT implements also the most used information-theoretic measure of directed information transfer between different brain regions or neurons: Transfer Entropy (TE) [101], equivalent under the definition we use to Directed Information [102]. TE is an information-theoretic measure of the causal dependency between the time series of a putative sender $X$ and the time series of a putative receiver $Y$. It is based on the Wiener-Granger causality principle, stating that a signal $X$ is causing $Y$ if the knowledge of the past of $X$ reduces the uncertainty about the future of $Y$. Given the time series $X$ and $Y$ of two signals simultaneously recorded over time from different neurons or brain regions, TE is defined as:

$$TE(X \to Y) = MI(Y_{\text{present}}; X_{\text{past}} | Y_{\text{past}}) \tag{5}$$

Where $Y_{\text{present}}$ is the value of signal $Y$ at the present time, and $Y_{\text{past}}$ and $X_{\text{past}}$ are the values of $Y$ and $X$ at a set of $k$ past times. TE computes the MI information that the past values of $X$ carries about the present value of $Y$, discounting the information that the past of $Y$ carries about its own present value. These measures of directed information transfer have been widely used to characterize communication between brain regions (see e.g. [64, 65, 67, 103]).

NIT allows calculating TE using the direct plug-in method. It allows to define the set of k past value used to compute TE. In most applications, TE is computed using one past value for X and Y,

defined by the delay between the selected past value and the present [65, 104, 105]. However, NIT allows to include past values over a range of different delays from the present. NIT features also an optimized routine for fast calculation of TE on spike trains, taking advantage of the reduced probability space deriving from binary signals [106].

Note that NIT implements also other more recent extensions of directed information calculations derived from the PID. For example, it implements also the recently introduced Feature-specific Information Transfer (FIT) [107]. FIT extends the previously described TE by computing not only the total amount of directed information that is transmitted from the putative sender $X$ and receiver $Y$, but quantifying how much of this total transmitted information relates to a specific stimulus feature of interest $S$. Conceptually, FIT quantifies how much of the MI encoded by the present activity of $Y$ was shared (redundant) with information about $S$ present already in the past of $Y$ while being unique with respect to the stimulus information that was encoded by past activity of $Y$ [107].

Importantly, NIT allows computing also other more refined directed information transfer measures derived from PID which can be expressed in terms of appropriate combinations of MI quantities, such as those introduced in Refs [66, 108].

### 2.2.6 Limited sampling bias correction

Accurate estimation of information quantities depends on accurate estimation of probabilities. Measuring probabilities from a limited number of experimental trials leads to statistical fluctuations in the estimated probabilities, which in turn leads to both statistical and systematic errors in information measures. The systematic error, or limited sampling bias, is due to the non-linear dependence of the information on the probabilities [32]. In most conditions, the limited sampling bias is positive, meaning that limited sampling tends to overestimate the MI [32, 109]. Intuitively, this is because differences of stimulus-specific neural response probabilities generated by random fluctuations due to limited sampling result through the MI equation as genuine, information-bearing features. The amount of bias is typically higher for less informative variables, and it decreases approximately linearly with the number of trials [32, 110]. Thus, although the limited sampling bias is present in all calculations of MI, it is particularly

prominent for neuroscience experiments because of the limited number of trials that can be collected and because of the relatively small information values of neural activity (in our experience, in typical experiments with subjects performing tasks while recording brain activity, it is extremely rare than more than $\sim 10 - 20$ trials per stimulus or task condition are available, and information values of individual neurons are usually much smaller than one bit).

Fortunately, several bias correction procedures have been developed, which reduce substantially the limited sampling bias from neural measures. In case of stimulus-response information $MI(S;R)$, Equation 1, most measures work well when the number of trials per stimulus is at least 4-10 times larger than the number of possible values of response $R$ [32, 41, 46]. This is a rule of thumb that is useful to set the number of bins used to discretize the neural response $R$. NIT is equipped with a sets of well-used for limited sampling bias correction in MI measure: Panzeri-Treves [41], linear and quadratic extrapolation [111], the shuffling procedure [32], the Best Upper Bounds (BUB) estimator [112], and the bootstrap correction [113]. An analytical bias correction method is specifically available for the Gaussian method [43]. Interfaces for easy plug-in of user-defined bias correction routines are available. A complete list of the compatibility between information-theoretic measures, bias correction strategies and information estimation methods implemented in NIT is provided in Table 5.

One point of interest that we found while running the NIT on simulated data is that, while the size of the limited sampling bias for mutual information follows well the analytical predictions of analytical polynomial expansions of the bias in terms of the inverse of the numbers of trial (e.g. [32]), the bias of II (which is not a mutual information quantity, but only a part of a mutual information quantity) was in general smaller than that predicted for mutual information with the same numbers of trials and response binning. In measures comparing mutual information with PID or II quantities, we thus recommend (as we did in Figure 10) to evaluate and compare the bias of PID and mutual information quantities in stretches of data in which we know information must be null (e.g. pre-stimulus time windows for stimulus information or II) and use those as estimates of bias values.

When analyzing multi-dimensional data (e.g. the simultaneous responses of neurons in a population), the number of possible responses of the population increases exponentially with the

size of the population. For example, the binary activity of a population of 10 neurons recorded simultaneously can take $2^{10}$ states, which would require an unrealistic number ($\sim$ 10000) of trials for accurate limited sampling correction. This makes it impossible to compute directly information from large populations [32, 110]. Dimensionality reduction and neural decoding algorithms, several of which are embedded as modules in NIT (Figure 3) embedded in NIT allow to analyze highly multi-dimensional data with a limited amount of trials.

### 2.2.7 Dimensionality reduction and neural decoding

Dimensionality Reduction (DR) methods are a precious tool for performing information-theoretical analyses of multi-dimensional neural data, as they allow to reduce the dimensionality of the response space $R$ in a meaningful way at the expenses of small information losses.

Within NIT we implemented, and coupled with the information theoretic calculation, many such DR methods that have been popular in the analysis of neural activity. The pipeline first maps the multi-variate neuronal response $R$ to a lower-dimensional space $\hat{R}$, then NIT computes the mutual information $MI(\hat{R};S)$ between the reduced neural variables $\hat{R}$ and $S$. The compression of the neural response space cannot increase the information and may lead to some information loss because of the data processing inequality [114]. However, it allows a more reliable sampling of the probability space with the limited number of experimental trial available.

The first class of DR methods implemented in NIT can be described as supervised decoding methods. These methods predict in each trial the most likely value of the stimulus $S$ that was presented given the observation of the neural response $R$ in that trial. This data compression for information calculations is popular [55, 56, 61] as effectively it reduces the response $R$ to the smallest space that can in principle preserve all information about $S$ (that is, the $S$ space itself). Two modules for neural decoding, implementing high popular decoding methods in neuroscience, are provided in NIT. The first one is based on linear, logistic or multinomial regression through elastic-net penalized Generalized Linear Models (GLM). The core of the GLM regression functionalities are provided by the GLMnet [115] library, directly interfaced with NIT. This ensures fast and reliable decoding on large datasets characterized by sparse

neuronal activity. Such types of decoders have been popular for neural activity analysis [56, 116, 117]. A second method for neural decoding applies a Support Vector Machines (SVM) for multi-class classification, which is also popular in neuroscience [118–120]. The back-end for SVM classification in NIT relies on the LIBSVM [121] package, providing fast implementation for multi-class Support Vector Classification and Regression.

NIT contains two modules for applying dimensionality reduction strategies that compress the space of neural responses in an unsupervised way without relation to the structure of the stimulus. The first one performs Principal Component Analysis (PCA), often used in neuroscience [78], through a custom-built fast MATLAB implementation. A second method is based on a Space-Time Non-negative Matrix Factorization (STNMF) [122]. The method, specifically designed for the analysis of spike trains, allows to decompose the neuronal response through a space-by-time tensor factorization. Moreover, it identifies ensembles of simultaneously active neurons and the temporal profiles of their activity. STNMF has been successfully used to extract information-rich features from the neural activity [122].

### 2.2.8 Hypothesis testing

NIT also provides algorithms to test the hypothesis that the measured information values are significantly different from a null hypothesis distribution of null information. While plug-in values of information for asymptotically large number of trials follow a chi-square distribution and their significance could be tested parametrically, no parametric null hypothesis distribution is known for finite number of trials (as it always the case in real calculation) and for methods different from plug-in. The well-established method to test for the significance of mutual information is the non-parametric permutation test in which all or part of the data structure is randomized to remove its information content [43, 47, 55, 123, 124]. This test computes, from many different random permutations of the data, a null-hypothesis distribution and a significance threshold to test the hypothesis that a measured value of information (which could be non-zero because of sampling bias or statistical fluctuations even if the data contain no information) for significance of information given the number of trials available and computational method used.

Significance for the value of $MI(R;S)$ is computed by randomly permuting (or "shuffling") the

neural response $R$ across experimental trials to destroy all information they carry about $S$. When computing multivariate information measures, it is sometimes of interest to test the significance of values of information between two variables conditioned on the value of other variables. For example, whether the activities of two neurons $R_1$ and $R_2$ have statistical dependencies beyond the one induced by the common tuning to the stimulus $S$, can be tested by computing the significance of $MI(R_1; R_2|S)$, the conditional mutual information between $R_1$ and $R_2$ given $S$. Whether $R_2$ carries stimulus information not carried already by $R_1$ can be tested by computing the significance of $MI(R_2; S|R_1)$, the stimulus information of $R_2$ conditioned on $R_1$ [125]. Significance testing of information values conditioned or partialized on values of other variables can be more precisely done by shuffling the statistical relationship between the variables we compute information about at fixed value of the variables we condition upon [125, 126]. This conditioned shuffling destroys the relations between the variables we compute information about while preserving the relationship that each of them individually has with the variables we condition upon.

In NIT, we implemented routines that easily create null-hypothesis distributions and significance thresholds for both standard and conditioned mutual information values, performing shuffling of any variable possibly at fixed values of other variables, with the number of different shuffles created a parameter of the analysis.

## 2.3 Extensive validation of NIT on simulated 2P data

NIT is a general-purpose toolbox, usable on any kind of neuroscientific data. The above-described algorithms implemented for computing information from neural activity have been extensively used and highly validated over the years with electrophysiological recording of spiking activity of single neurons and populations and with aggregate electrical measures of neural activity such as LFPs and EEG [32, 43, 44, 127–130]. As a result, we know well how to set the parameters of information theoretic calculations with such signals. However, studies of how best to apply these methods to 2P calcium imaging data are still limited, and no systematic validation is available.

Thus, we next validated the capabilities of NIT to extract stimulus information from 2P calcium imaging experiments through extensive simulations of synthetic 2P traces. In the analysis, we

strived to cover a wide range of experimental conditions, relating both to the neuronal response and its modulation by the stimulus as well as the experimental apparatus. We first detail the model for the generation of imaging traces, followed by testing the algorithms in NIT in an extensive parametric sweep across all conditions examined. Aim of this effort was to offer a solid validation on how to analyze 2P data using information theory, highlighting the difference between the information content in imaging data compared to traditional electrophysiology analysis, as well as the advantages of non-parametric copula over binned estimators when applied to imaging data.

### 2.3.1 Forward model for the generation of synthetic fluorescence traces

To quantify the extent to which we can extract, from 2P imaging data, all or most neural information available in the underlying spike trains, we first implemented a realistic forward model for the generation of synthetic fluorescence data from ground truth spike trains. This forward model is available within NIT and can be used by users to perform their own simulated experiments to match their own experimental conditions. We implemented and compared two models for the generation of synthetic two-photon calcium imaging traces.

The first one (Figure 4A, left panel) defines the spike to fluorescence transfer function through a linear convolution with a double-exponential kernel [131–133]. This model is a good approximation of the fluorescence evoked by action potentials in a low spike rate regime, but fails to account for non-linear effects present at high firing rates [134].

The second model (Figure 4A, right panel) is based on a single compartment model (SCM) of calcium dynamics in the cytoplasm [135]. Generation of fluorescence from a given spike train is obtained in three successive steps. The first step models the concentration of unbound calcium within the cell membrane. Every action potential elicits a step influx of calcium ions. The free calcium intake accounts, in a non-linear way, for the effects of both endogenous and exogenous (indicator) calcium buffers in the cytoplasm. The extraction of free calcium from the cell is modelled through a linear leak term combined with a non-linear extrusion term for the membrane calcium pumps. Non-linear effect of the release of free calcium from internal buffers in the cell is also included in the model. A second step in the model allows to calculate the fraction of calcium

indicator that is bound to calcium to the one that is not. This is performed through integration of the indicator binding/unbinding kinetics. A linear model converts the fraction of bound and unbound indicator to fluorescence values. This biophysically plausible model for fluorescence generation includes four forms of non-linearity, which cannot be obviously present in the linear convolution model. Those are related to: calcium intake after every action potential, free calcium release from endogenous and exogenous buffers, calcium extraction from membrane pumps and saturation of calcium indicator. A sample train of action potential and the resulting traces for free cytoplasmatic calcium, indicator-bound calcium and fluorescence is shown in Figure 11.

In both models, we added Gaussian white noise to the generated fluorescence to account for experimental noise and manipulate the SNR of simulated recordings (see Materials and Methods for details). We assessed the accuracy of the two methods in generating realistic calcium imaging traces by comparing synthetic traces with experimental ones. The experimental dataset we used [136, 137] contains simultaneous calcium imaging time series and juxtasomal electrophysiological recording in neurons expressing both GCaMP6f and GCaMP6s. We used the experimentally recorded action potentials as inputs for both forward models. The levels of noise in the synthetic traces were tuned so that each synthetic $\Delta F/F$ signal had the same signal-to-noise ratio (SNR) than the corresponding experimental trace. The sample experimental and synthetic $\Delta F/F$ traces, on both indicators, are reported in (Figure 4B).

For each acquisition in the dataset, both Root Mean Square Error (RMSE) (Figure 4C) and Pearson's correlation coefficient (Figure 4D) between experimental and synthetic $\Delta F/F$ traces were calculated. The single compartment model showed significantly better performance than the linear convolution model, both in terms of RMSE and correlation for both considered calcium indicators. To further compare the performance of the two methods, we assessed their performance in reproducing realistically high levels of fluorescence. To this end, we compared the distribution of synthetic $\Delta F/F$ values against real values reported by experimental 2P calcium imaging traces (Figure 4E). The SCM shows a longer tail of high $\Delta F/F$ values – especially evident for GCaMP6s – which is closer to the distribution of the experimental data. This shows that the SCM model allows to generate synthetic 2P calcium imaging traces covering a broader part of the dynamic range of the indicator with respect to a linear convolution kernel. Overall, these results show that the SCM generates more realistic synthetic calcium imaging

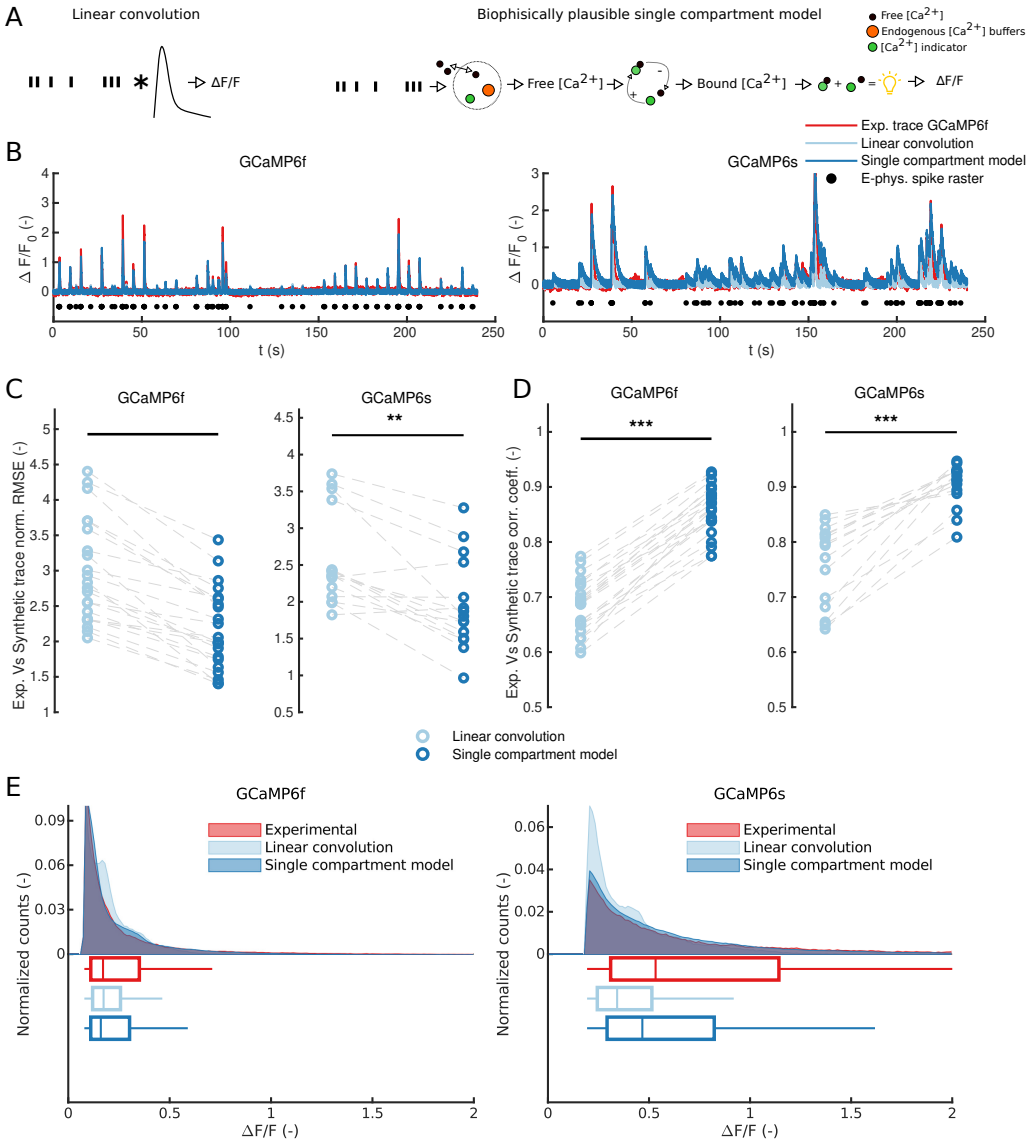


**Fig. 4: Comparison of methods for the generation of synthetic GCaMP6 traces given a spike train.** **(A)** Schematics of the two methods considered: a linear convolution of the spike train with a double exponential kernel (left) and a biophysically plausible Single Compartment Model (SCM) of calcium dynamics (right). The SCM considers the presence of endogenous (orange) and exogenous (green) calcium buffers in the cytoplasm to predict the concentration of free calcium within the cell membrane. Binding/unbinding dynamics of free calcium to the indicator is simulated to generate time traces of bound and unbound fluorophore concentrations. Synthetic GCaMP6 fluorescence traces are then generated through a linear combination of the concentration of bound and unbound indicator concentrations. **(B)** Sample two-photon GCaMP6 experimental traces (red) recorded with simultaneous loose-seal cell-attached electrophysiology (black scatter). Experimental data from [136, 137]. The panel also shows synthetic traces generated using both a linear convolution (light blue) and SCM (dark blue) given the experimentally recorded spike train, under the same SNR than the experimental GCaMP6 trace. **(C)** RMSE of synthetic Vs experimental GCaMP6 traces for both models considered (**: $p < 0.01$, one-tailed Kruskal-Wallis test). **(D)** Correlation coefficient of synthetic Vs experimental GCaMP6 traces for both models considered (***: $p < 0.001$, one-tailed Kruskal-Wallis test). **(E)** Distribution of the upper 30$^{\text{th}}$ percentile of $\Delta F/F$ values across all frames in experimental data and both linear convolution and SCM models.

traces. Thus, in all subsequent NIT information algorithm testing, we used calcium traces generated with the SCM.

### 2.3.2 Effect of neuronal firing and experimental conditions on information available from calcium imaging traces

Recording somatic calcium concentration in neurons through fluorescent two-photon imaging is widely used to infer the neuronal supra-threshold activity [137–143]. However, we still lack a systematic appreciation of the consequences of the limitations of calcium imaging for information-theoretic measures of neural activity and of how best to deal with them. For this reason, we investigated the effect of a series of variables on calculations of information from 2P calcium imaging traces. These include factors related to the underlying neurobiology, such as the shape of post-stimulus time histogram (PSTH), mean spiking rate (SR) to different stimuli, or technical characteristics of the experimental setup, such as imaging frame rate (FR), signal-to-noise ratio (SNR), and calcium indicator. We performed a parametric sweep over those parameters as follows.

We simulated activity in response to two different categorical "stimuli" (the variable $S$, $s = 1$ or $s = 2$, in the MI calculation, Equation 1). These simulated stimuli elicit a different neuronal response over a 1 second post-stimulus window. Differences in stimuli are modeled as differences in the strength and time pattern of the neural responses they elicit, as explained next. The two stimuli could elicit a time-averaged spike rate (SR) along the trial of either 1 or 2 Hz (we termed those cases as Low MI, low SR), 12 Hz and 13 Hz (Low MI, high SR) and 2 Hz and 12 Hz (High MI). For each mean firing rate response, we considered two different temporal shapes of elicited Post-Stimulus-Time-Histograms (PSTHs): tonic (i.e. uniform over time) and phasic (i.e. Gaussian-shaped time dependency, peaking at 0.25 s, standard deviation 0.01 s). Given a time-averaged SR, both phasic and tonic responses have the same integral over time, i.e. the same expected number of spikes. The shapes of the PSTH are plotted Figure 5A, top panels. Spike trains were generated through an inhomogeneous Poisson process with an instantaneous rate equal to stimulus-evoked PSTH. We simulated situations with three different frame rates for the imaging set-up: 5 Hz (representative of galvanometric imaging with raster scanning), 30 Hz (representative of imaging with resonant scanners) and 100 Hz (representative of alternative high acquisition frequency methods, e.g., smart line scanning imaging [141]). Spike trains and $\Delta F/F$ traces were

always generated at a sampling rate of 1 kHz, and the latter were then subsampled to the desired sampling rate. SNR was varied systematically across simulations by varying the amplitude of the noise added to the calcium imaging traces.

Sample spike trains and $\Delta F/F$ traces (30 Hz frame rate, SNR $= 15$, two sample trials per each mean firing rate) for both GCaMP6f and GCaMP6s are shown in Figure 5B. In this part of the analysis, information calculation parameters were as follows. We used the plug-in direct method, discretizing these neural responses in 4 equi-spaced bins. We used peak $\Delta F/F$ over the trial as response $R$, as it is a widely used approach for the analysis of two-photon imaging data [81, 144]. For each combination of parameters (SNR, FR, calcium indicator, PSTH and levels of stimulus-modulated firing rate), 50 independent MI calculations (each with 400 trials per stimulus) were performed. No limited sampling bias correction was used, because the number of trials was large enough for the MI to be bias-free [32].

We first investigated the effect of varying the imaging FR and SNR on the mutual information computed from the somatic calcium imaging signal for phasic and tonic PSTH shapes (Figure 5C, results of the statistical tests are summarized in Table 6). In Figure 5C we used peak $\Delta F/F$ of GCaMP6f to compute information from the calcium traces, but we obtained similar results (not shown) using other calcium imaging metrics (e.g. mean $\Delta F/F$). Both FR and SNR have a limited effect size on the information contained in the peak $\Delta F/F$. The notable exception was the case of phasic PSTH shapes and high neural information, in which case increasing SNR led to a notable increase of stimulus information with SNR (Figure 5C and Table 6). The effect of using either a slower (GCaMP6s) or faster (GCaMP6f) calcium indicator is explored in Figure 5D and Table 7 (with $SNR = 15$ $FR = 30$ Hz). In most cases the information obtained from the calcium traces with peak $\Delta F/F$ was approximately the same with either indicator, with the exception of the high information, phasic PSTH case. In this case using the GCaMP6s led to higher information extracted from the calcium traces, due to its slower dynamics and higher dynamic range compared to GCaMP6f.

Because calcium imaging measures indirectly the neural activity, with a lower SNR and lower temporal resolution than direct electrophysiological recording of spikes, it is commonly assumed that the information reported by a calcium indicator will be smaller than that encoded in neural

activity. To evaluate this information loss we computed, the average fraction of information present in peak $\Delta F/F$, relative to the one present in a spike rate code. We found that the percentage of spike rate information extracted on average from the calcium traces varied widely, from 50% to 100% (Figure 5E), depending in particular on the features of neuronal firing. More stimulus information is lost when computing it from the calcium traces rather than from the spike rate when the simulated neuron fires tonically than when it fires in a phasic way. This is because, as apparent from the individual traces in Figure 5B, the phasic PSTHs with a stronger and more concentrated spike rate elicit more repeatable and less noisy calcium traces than those obtained with the tonic PSTHs having a similar number of spikes randomly distributed over time.

In sum, our simulations suggest that the NIT information theoretic analysis of calcium traces recovers a good fraction (between 50% and 100%) of the information encoded in electrophysiological spike rates, with the extraction being particularly efficient for high-rate phasic responses and high dynamic range indicators.

Spike rate information is not an upper bound for stimulus information contained in $\Delta F/F$ traces. Since as discussed above calcium imaging reports an indirect measure of neural spiking activity, the information about stimuli computed from $\Delta F/F$ traces will miss out on some of the information carried by the temporal spike pattern as measured from electrophysiology recordings. However, this does not necessarily imply that in all cases the information computed from the calcium traces will be lower than the information carried by the underlying spike rate code.

From the mathematical point of view, the data processing inequality [114] ensures that stimulus information cannot be increased, but can only be lost or remain equal, every time a transformation of $R$ not dependent on $S$ is applied to the data. This implies that information in the spike rate is always lower than or equal to the information contained in the full spike train. However, because the transformation that maps the spike train into a calcium trace is not a direct consequence, in Markovian terms, of the transformation that links a spike train to spike rate, the stimulus information in the calcium trace may either be higher, equal or lower than the stimulus information in a rate code.

From the intuitive neurobiological point of view, the fluorescence traces can have more

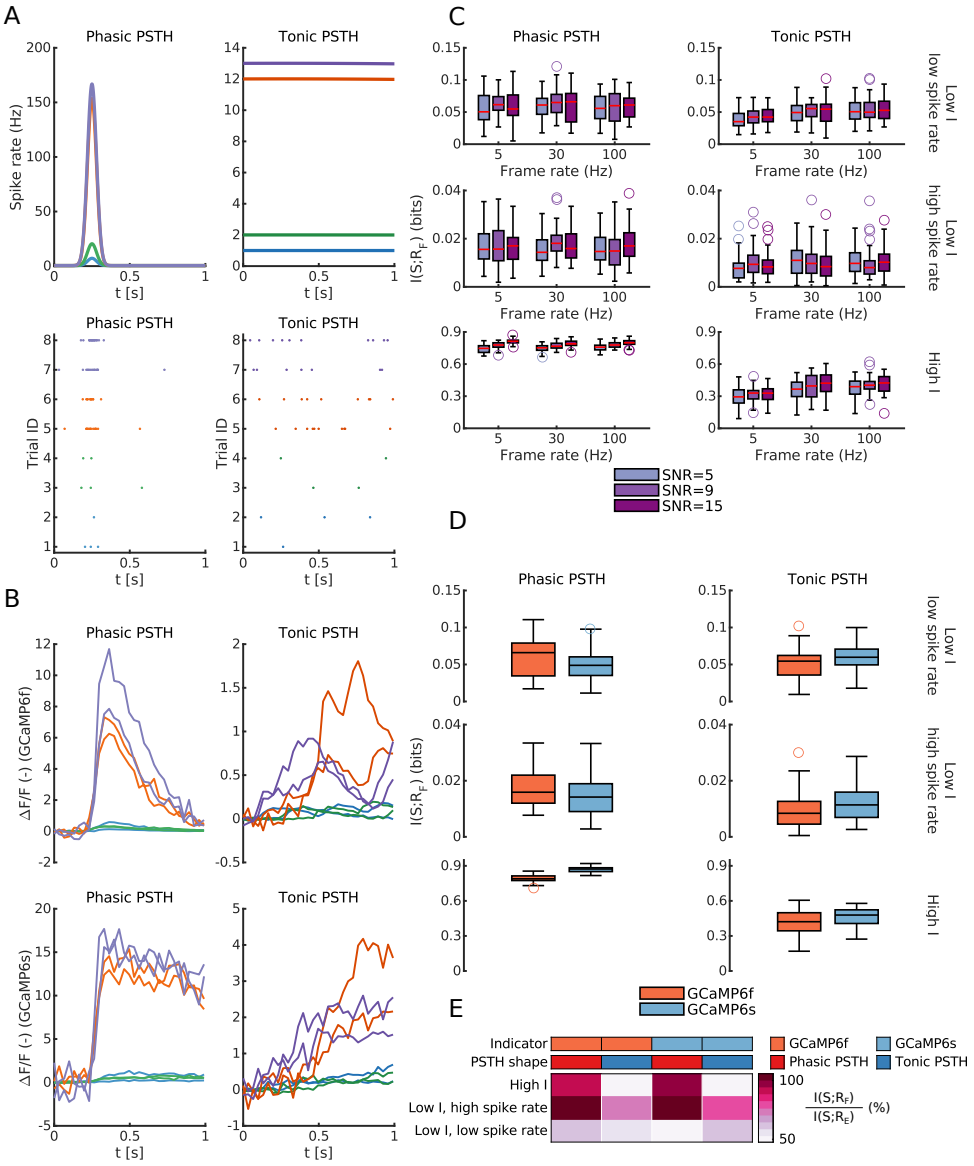


**Fig. 5: Effect of neuronal firing regime and experimental conditions on stimulus information retrieved from calcium imaging signals. (A)** Instantaneous neuron spiking rate (SR) for phasic and tonic post-stimulus time histogram (PSTH) responses (top row), average firing rates over the trial duration are identical between the two conditions at fixed stimulus. Corresponding Poisson spike rasters for two sample trials per each stimulus (bottom row). **(B)** Synthetic GCaMP6f (top row) and GCaMP6s (bottom row) traces (SNR 9, frame rate 30 Hz) relative to spike rasters in panel (A). **(C)** Distributions of stimulus information in GCaMP6f $\Delta F/F$ traces at various information levels and for both tonic and phasic PSTH. Effect of SNR and imaging frame rate on stimulus information. All calculations of MI consider two stimuli. In Low MI, low SR the neuron responds to the two stimuli with 1 Hz and 2 Hz average spiking rate (blue and green curves panel (A)). In Low MI, high SR the neuron responds to the two stimuli with 12 Hz and 13 Hz average spiking rate (orange and violet curves panel (A)). In High MI the neuron responds to the two stimuli with 2 Hz and 12 Hz average spiking rate (green and orange curves panel (A)). Each box plot reports data from 50 simulations. Results of the statistical analysis for the data in this panel are reported in Table 7. **(D)** Effect of calcium indicator on stimulus information at different PSTH shapes and information levels. Each box plot reports data from 50 simulations. Results of the statistical analysis for the data in this panel are reported in Table 7. **(E)** Percent of stimulus information in max $\Delta F/F$ with respect to MI encoded in spike rate at the same conditions. Values are average values over 50 simulations. All data in the figure refer to simulated traces. Mutual information is evaluated using plug-in method. All MI calculations consider max $\Delta F/F$ across the trial as a metric of neuronal response.

information than the spike rate in cases in which the latter loses some of the information encoded in the spike timing that the former captures. Indeed, owing to the slow dynamics of the indicator, $\Delta F/F$ traces contain not only information about how many spikes are emitted by a neuron, but also how close they are in time. The contribution of this effect to the information content of calcium traces is amplified as the ratio between the decay constant of the indicator and the stimulus-modulated inter-spike interval increases, and as the informative content of a spike-rate code alone decreases. As such, it becomes particularly evident for phasic PSTH when stimulus information is encoded at high mean firing rates and rate information is low (Figure 6A). Data in Figure 4 are from a limited portion of the full parametric sweep ($FR = 5$ Hz, $SNR = 15$, GCaMP6f), but similar conclusions can be drawn when considering the full range of parameters investigated (Figure 14). As an example, we have considered one of the points (green scatter in Figure 6A, central panel) showing more information in peak $\Delta F/F$ than in SR.

In this case, because of the different stimulus-modulated inter-spike interval, even when the two stimuli elicit an identical spike rate in two different trials, the $\Delta F/F$ traces will still show stimulus-related differences (e.g. different peak activity as show in Figure 6B, top row) similar to their trial-averages (Figure 6B, bottom row). Additionally, for the case of a phasic PSTH, the only stimulus informative spikes are time located in the narrow window around the peak of phasic activity (Figure 6C). All other spikes emitted in the baseline activity period (baseline firing rate set at 0.5 Hz in all simulations reported) are non-informative and thus degrade the SR information. On the contrary, given the high stimulus-modulated firing rate of the neurons, and the slow dynamics of calcium indicators, spikes outside of the stimulus-modulated window have little effect on $\Delta F/F$ traces, contributing to increase its stimulus information compared to a spike rate code.

Thus, an ideal decoder of neural activity would use the spike times to consider only those spikes in the informative window and discard the others, together with weighting spikes in the informative window proportionally to the instantaneous inter-spike interval. We implemented such decoder by projecting the neural activity in each trial on a template based on the difference between the trial averaged PSTH when responding to the two stimuli (Figure 6C, bottom). We have then used the GLM decoder implemented in NIT to calculate the MI between the real and decoded stimulus when using peak $\Delta F/F$, spike rate (SR) or the template projected activity and spike

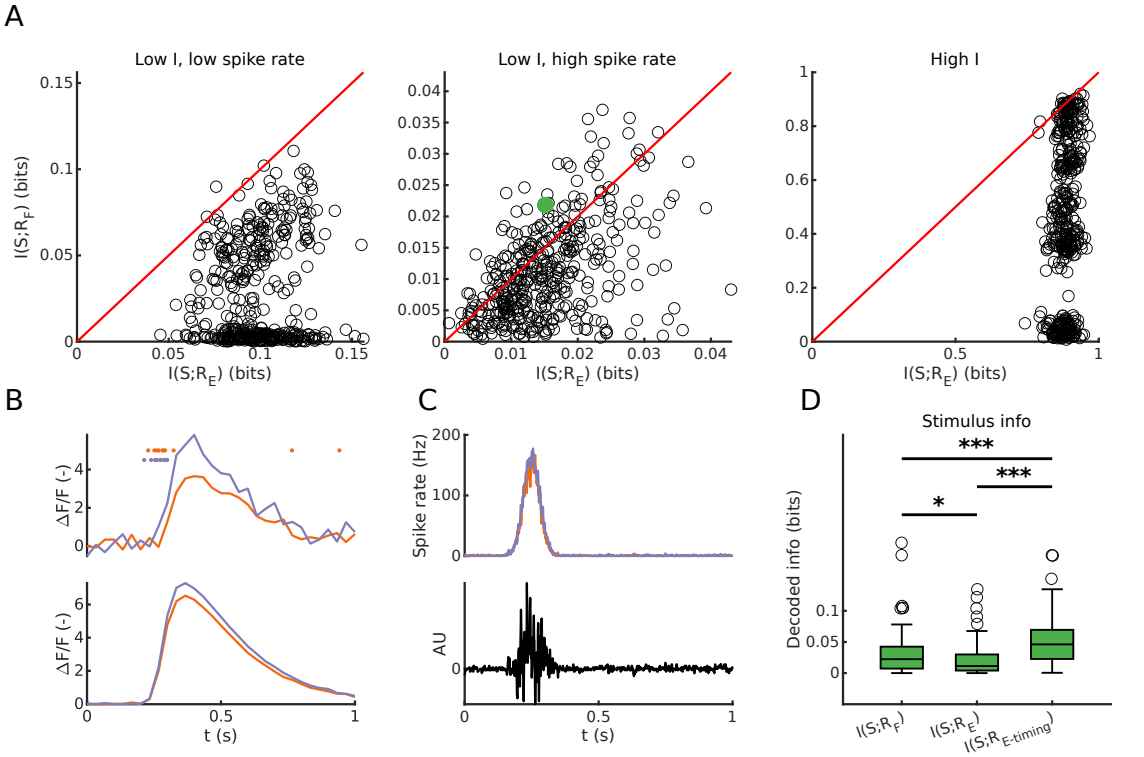


**Fig. 6: Information in $\Delta F/F$ can be higher than spike rate informations. (A)** Scatter plots of stimulus information in SR vs stimulus information in peak $\Delta F/F$. Each scatter results from one over 50 MI calculations across the following parametric sweep: $SNR = 15$, $FR = 30$ Hz, GCaMP6f, phasic PSTH. Red lines are the quadrant bisectors. The green scatter point refers to the point analyzed in panels (B-D). **(B)** Top: stimulus-evoked spike rasters and corresponding $\Delta F/F$ traces for two specific trials with an identical trial-averaged spike rate (10 Hz) but responding to two different stimuli (color-coded). Bottom: trial-averaged stimulus-evoked $\Delta F/F$ traces. **(C)** Top: trial-averaged PSTH for the response to the two stimuli. Bottom: spike-timing template used in the decoding analysis in panel (D). **(D)** Values of MI between true and decoded stimulus calculated when considering: max $\Delta F/F$, SR and simultaneous contribution of SR and spike timing (ST). The analysis is performed on the data corresponding to the green point in panel (A). Box plots report 100 cross-validated runs of GLM decoder (*: $p < 0.05$, ***: $p < 0.001$, Bonferroni corrected Kruskal-Wallis multiple comparison test). All data in the figure refer to simulated traces. Mutual information is evaluated using plug-in method.

rate (SR+ST), to compare their information content. Results are summarized in Figure 6D. Each box plot in the figure shows the distributions of MI between the real stimulus and the decoded one across 100 cross-validated runs of the GLM classifier. While the stimulus information in the calcium trace is lower than the one present when considering both spike rate and spike timing, it is significantly higher than the mere SR information. This shows how the calcium dynamics captures some properties of the optimal spike timing decoder and that spike timing contributes to the informative content represented in $\Delta F/F$.

While cases like the above example – in which more information is available in the calcium traces than in the time-averaged spike rates – may not happen frequently with real data, it should be noted that calcium traces will always contain a mix of spike rate and spike timing information, which is important to keep in mind when interpreting empirical results.

### 2.3.3 Dependence of stimulus information on the metric used to quantify single-trial calcium fluorescence responses

In the previous sections, we quantified information from calcium traces using the peak $\Delta F/F$ as a metric of single-trial responses based on two-photon fluorescence. This measure is widely used in the analysis of calcium imaging data [81, 144–146], but is not the only possible choice. Several other metrics are commonly used to quantify single-trial activity in a post-stimulus window from calcium imaging signals. These metrics include: mean $\Delta F/F$ [81], integral $\Delta F/F$ [147–149], linear deconvolution using an exponential kernel [150], and spike inference algorithms [142, 151–153]. Among spike inference methods, we focused on OASIS [151] due its competitive performance [132].

To inform future information-theoretic analyses of calcium imaging traces, we investigated on simulated data how well the different metrics listed above performed in extracting stimulus information. All listed metrics have advantages and disadvantages. The peak $\Delta F/F$ captures the strength of the calcium transient responses but can be heavily influenced by noise and does not capture the temporal structure of the fluorescence. Mean and integral $\Delta F/F$ are less influenced by noise, but they are less effective in capturing the strength of transient activations. Both linear deconvolution and OASIS quantify aspects of calcium signal potentially closer to spiking activity

but assume a linear relation between spikes and measured fluorescence. In addition to the methods listed above, we propose a novel non-linear metric, that we termed estimated calcium, that inverts the biophysically plausible non-linear forward model to estimate the concentration of intracellular free calcium from $\Delta F/F$ traces (see Materials and Methods).

We have thus used the same five-dimensional sweep of simulation parameters (FR, SNR, indicator, PSTH shape and stimulus modulation of SR) used in Figure 5 to calculate the levels of stimulus information contained in each of the above-mentioned measures of neural activity in the 1-second-long post-stimulus window. We computed stimulus MI in both SR and $\Delta F/F$ metrics using the direct method with equally-spaced binning in 4 bins. Fifty independent runs are performed in each of the coordinate points of the parametric sweep. The distribution of $\Delta F/F$ metrics showing the highest mean amount of stimulus information across the parametric sweep is shown in Figure 7A (actual levels of MI across all conditions in the parametric sweep are reported in Figure 7B, together with the value of stimulus information in the spike rate code). Overall, peak $\Delta F/F$ extracts most stimulus information when the stimulus is encoded at high rates, mostly when the neuronal response has a tonic PSTH. In these conditions the stimulus will, in fact, modulate mostly the amplitude of the calcium imaging response. In other conditions, most of the stimulus information contained in the calcium imaging response was retrieved by estimated calcium. OASIS shows good performance at high imaging frame rates, though it suffers particularly low rates (Figure 13). When looking at the absolute levels of information retrieved across all conditions Figure 7B, estimated calcium performs on average better than the other metrics considered by recovering about 65% of the underlying SR code.

Statistical significance of the results was assessed through Kruskal-Wallis test with Bonferroni correction for post-hoc comparisons. In all conditions of the parametric sweep, the best performing calcium imaging metric, together with the others being non statistically different from it ($p > 0.05$), were marked as best for that condition (stars in Figure 13). Figure 7C reports the percentage of cases, across all the conditions examined, where each metric was part (light grey) – or was the only component (dark grey) – of the best performing group. Both the linear deconvolution and the newly proposed estimated [Ca] showed to be the most versatile spiking activity metrics based on $\Delta F/F$. Estimated [Ca] is among the best performing metrics in more than 80% of the conditions examined in our parametric sweep and is the only best performing

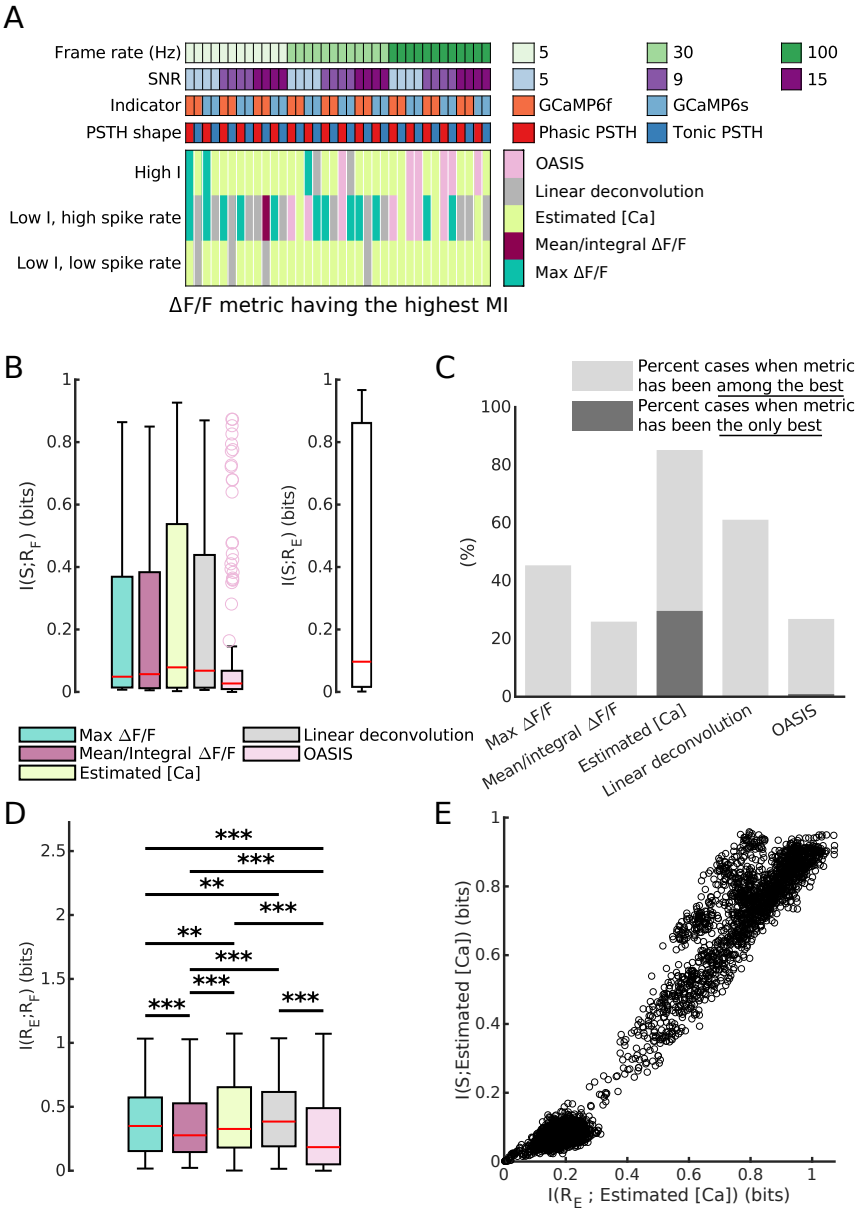


**Fig. 7: Appropriate processing of $\Delta F/F$ signal increases the retrieved stimulus information from calcium imaging traces.** **(A)** Best performing metric based on $\Delta F/F$ signal for each of the conditions explored in the parametric sweep. Best performing metric at each condition is defined as the one retrieving the highest value of stimulus information. See Materials and Methods for detailed definitions of each of the metrics. **(B)** Distributions of values of stimulus information reported by each metric (left) and by a spike rate code (right) across all the calculations performed in the parametric sweep shown in panel (A). **(C)** Percent of cases, across the whole parametric sweep shown in panel (A), where each $\Delta F/F$ metric has been among the best performing metrics (light grey bars) or the single best performing one (dark grey bars). Best metrics are defined as the ones recovering the highest amount of stimulus information ($p < 0.05$ Bonferroni corrected Kruskal-Wallis multiple comparison test). Full data for this figure are reported in Figure 13. **(D)** Distributions of values of spike rate information reported by each metric across all the calculations performed in the parametric sweep shown in panel (A). **(E)** Scatter plot of stimulus information in Inferred [Ca] against spike rate information carried by the same metric. Data in this panel include All data in the figure refer to simulated traces. Mutual information is evaluated using plug-in method using 4 equally-spaced bins do discretize spike rate and the calcium metrics.

one in around 25% of cases considered. Linear deconvolution works well in retrieving stimulus information in around 60% of conditions. Mean/integral $\Delta F/F$ and OASIS, on the other side, are only among the best performing groups in around 25% of the cases, showing poorer performance in reconstructing spiking information. (Note that the poorer performance of OASIS was not due to incorrect set-up of the algorithm as we have verified (Figure 12) that the deconvolved activity we obtained through OASIS had similar correlation with ground-truth spike recordings as reported previously using this algorithm on the same dataset we use here for validation, see [154]). Linear regression of the average z-scored deconvolved activity using OASIS and the underlying ground truth SR shows, however, how the levels of z-scored deconvolved activity predicted by OASIS have a relatively high variability that cannot be explained by a linear fit ( $R^2 = 0.52$ GCaMP6f, $R^2 = 0.34$ GCaMP6s). This suggests that, while OASIS matches the timing of neuronal activity with reasonable accuracy, the magnitude of the deconvolved calcium trace reflects less well the underlying firing rate, limiting the applicability of the method for information-theoretic measures of neuronal activity. The poorer performance of OASIS becomes especially noteworthy given that spike inference algorithms are typically performing better on synthetic data than in real experimental conditions, and the assumption of Poisson spiking used in our synthetic data should favor the method's accuracy [151].

In addition to considering which calcium metrics are better for computing single-trial information about external stimuli, we consider another, and perhaps equally important question, of which metric of calcium activity best reconstructs the underlying spike rate of the same cell. We computed the mutual information between the spike rate during the 1s post-stimulus window in our simulated trials and the calcium metric. This result (Figure 7D) confirms that estimated calcium and a linear deconvolution are, on average, carrying more information about the spike rate code than the other calcium metrics analyzed.

An explanation of why calcium metrics that carry higher stimulus information also carry higher information about the spike rate is that stimulus information is carried by the spiking activity of neurons and these calcium metrics reconstruct its value well. In support of this explanation, we found that the levels of stimulus information extracted from the $\Delta F/F$ activity with a given set of simulation parameters correlated with the levels of information present between the calcium imaging signal and the electrophysiology in the same simulation, as shown by the scatterplot of the

two information values across different simulations for the case of the estimated calcium (Figure 7E).

### 2.3.4 A comparison of non-parametric copula and binned plug-in methods for computing information from calcium imaging traces

All above examples computed information using the plug-in binned methods, a choice that has been widely used due to its ease of implementation, robustness and fast computational time [43, 44, 55, 71]. However, other more computational demanding but potentially more accurate methods are also available to compute information from limited experimental samples. NIT implements the recently developed Non-Parametric-Copula information estimation [88]. Here we test the advantages for computation of information from calcium imaging of this more computationally expensive method.

We first investigated whether the NPC offers advantages in terms of reduction of limited sampling bias in case limited datasets are available. To this end, we introduced, in the multidimensional sweep over the simulation parameter space outlined in the previous sections, a further parameter: the available number of trials per stimulus (here varied in the range 5 to 400). We found (Figure 8A) that, for both copula and direct plugin method, and consistent with previous studies [32], the information had a big upward bias for low numbers of trial per stimulus (5 to 20), and then converged to the asymptotic value for larger number of trials (several tens). To quantify how quickly the information estimate in individual simulations reached the asymptotic values across methods, we repeated the above analysis over a large number of simulations with different parameters according to our 5-dimensional parameter sweep. For each individual set of simulation parameters, we compared the distribution of calcium information values for different numbers of trials against the asymptotic (400 trials per stimulus) distribution. The lowest number of trials giving a distribution not significantly different from asymptotic (t-test, $p < 0.05$) was considered the minimum required by the method to provide a bias-free estimate of MI. We repeated the process for the whole parametric sweep, computing the ratio between the trials needed by the copula and by the binned methods. The distribution of the ratio is shown in Figure 8B. In this figure, values lower than 1 imply that the copula method is performing better than binned methods for bias free information estimations, while values higher than 1 imply that the

binning method works better. For the vast majority of simulations, the non-parametric copula needed less trials to reach asymptotic values of information. Thus, the non-parametric copula should be favored when analyzing smaller datasets.

Non-parametric copula is particularly suited to be applied on continuous variables. This suggests that larger amounts of information can be extracted from calcium signals, which are continuous, with non-parametric copulas than with binned estimators for MI. We thus examined the asymptotic information values provided by the copula against binned methods for both simulated spike trains and calcium imaging traces (Figure 8C). For the electrophysiology, the non-parametric copula performed better than binned methods only in the cases which information content is not high. However, for calcium imaging, the advantage of the copula was accentuated and was also present in high information cases. This underlies the specify usefulness of the non-parametric copula for calcium imaging. Note that we did not find comparably high performance when using parametric Gaussian copulas (also implemented in NIT), rather than non-parametric copulas. This is because responses of individual neurons carry non-gaussian dependencies with the stimulus (statistics is of neurons approximately Poisson, which differs from Gaussians for low spike numbers typically observed in a trial) and this translates in non-gaussian dependence between stimuli and calcium traces, which make the use of Gaussian copulas not generally applicable.

Despite the advantages that the copula has compared to the binned methods, there also exist drawbacks. The main limitation is the computational time required to fit the copula based on the data. As an example, the computations reported in Figure 8A required approximately 200 more CPU time with the non-parametric copula than the direct plug-in method.

## 2.4 Analysis of experimental data validates findings on synthetic traces

Our information theoretic analysis of realistic simulations of calcium imaging traces generated by neural spiking activity indicates that the calcium imaging traces are able to extract sizeable amounts information about both external stimuli and about the levels of the underlying spike rates. It also suggests that certain metrics of single-trial activity for calcium traces are better than others for extracting such information. Here, we tested some of the above predictions from simulated activity on real empirical data. We used NIT to analyze four independent datasets with

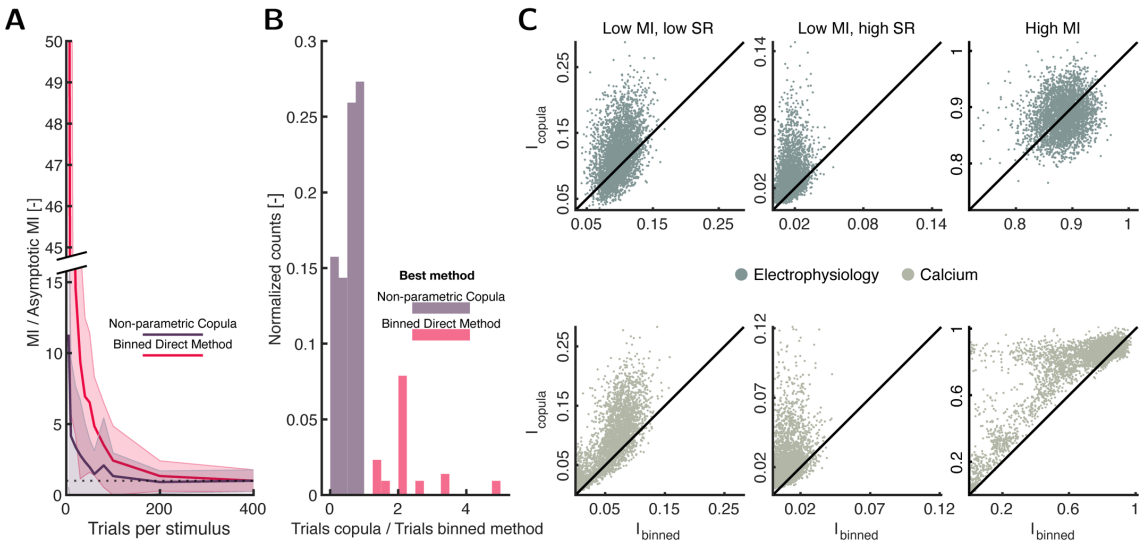


**Fig. 8: Comparison between binned methods and non-parametric copula. (A)** MI values (mean $\pm$ SD) for a single coordinate point in the considered parametric sweep (GCaMP6f, FR $=$ 5 Hz, SNR $=$ 5, Low MI, High SR, tonic PSTH) using NPC and binned direct method with an increasing number of trials per stimulus. The dotted horizontal line represents the y-axis value of one (when the information estimation reaches its asymptotic value). **(B)** Distribution of ratio between number of trials needed by the copula and binned method to reach asymptotic information values. Note that a ratio lower than 1 implies that the copula retrieves asymptotic values with less trials than binned method. **(C)** Information values provided by the copula against values given by the binned method for three different information levels (Low MI, low spike rate; Mid MI, high spike rate; and High MI) and both electrophysiology and calcium data. All data in the figure refer to simulated traces. Note that the samples included in this figure correspond only to the deconvolved calcium.

simultaneous cell-attached electrophysiological and two-photon imaging recordings from both GCaMP6f and GCaMP6s-labelled neurons during spontaneous activity [134, 137, 155, 156]. We focused on using NIT to compute how much information about the spike rate each calcium metric provides. We divided the experimental time traces in padded windows of 0.5s, and then computed the mutual information between the spike rate in a considered window and the calcium metric in the given window. We used the NPC information calculation method as it performs more reliably as shown in the previous section. Similar conclusions, however, would have been reached using the direct binned method (not shown).

Results of this information calculation on all neurons with calcium traces with SNR higher than 9 are reported in Figure 9. These results confirm that, as with the simulated data, sizeable amount of information about the underlying spike rate can be obtained from the underlying traces. These information values are of the order of 0.2 bits, which corresponds with significant but far from perfect spike train reconstruction from the calcium metrics. Comparison of how the amount of

information varies between $\Delta F/F$ (Figure 9) confirms the results emerging from the parametric sweep on simulated traces. Estimated calcium and linear deconvolution were, on average, better at reconstructing spike train information that other calcium imaging metrics.

The publicly available datasets were designed to test the correspondence between spike rates and calcium traces and not to study sensory coding, thus had no or insufficient data with responses to sensory stimuli to study sensory information. However, as shown by our simulations (Figure 7E), metrics that are appropriate for inferring spike rate values are also expected to be appropriate to extract stimulus information.

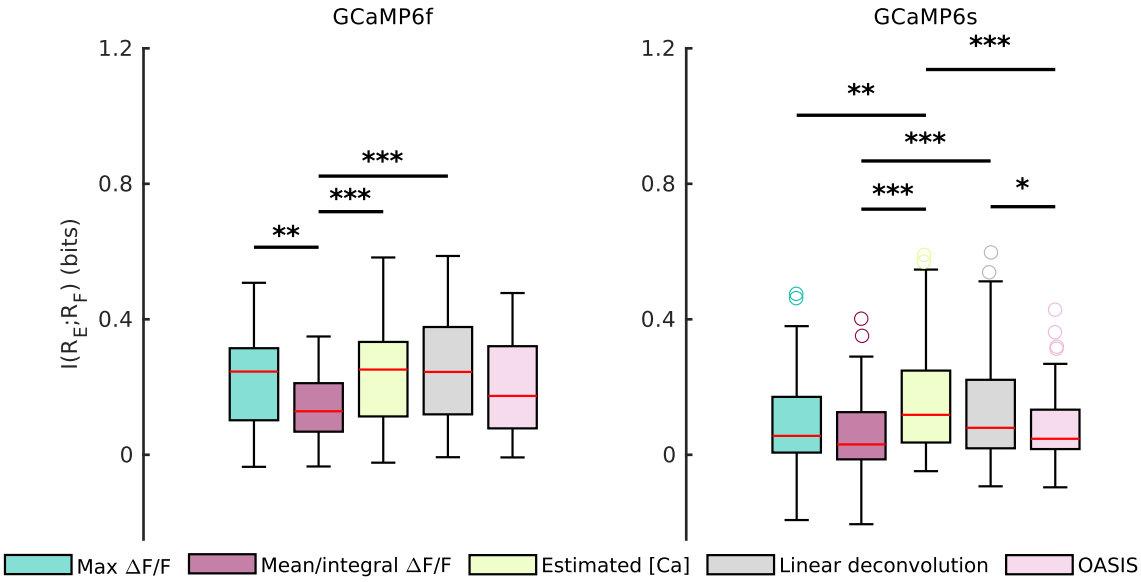


**Fig. 9: Validation of performance of spiking activity metrics based on $\Delta F/F$ in recovering stimulus information on experimental data.** **(A)** Box plots of mutual information between different spiking activity metrics based on $\Delta F/F$ and spike rate. Data in this panel refer to simultaneous cell-attached electrophysiology and two-photon imaging recordings from previous publications [134, 137, 155, 157]. Traces in the original datasets have been filtered for $SNR > 9$.

## 2.5 Examples of use of intersection information to find pure, stimulus unrelated choice signals as markers of preparatory activity

We finally exemplify, on real data, possible uses of the PID tools within NIT. In particularly, we exemplify possible and novel uses of Intersection Information (II) [99, 100], a formalism developed specifically for the analysis of neural recordings in perceptual decision tasks. As reviewed in the Intersection Information section above, II measures that amount of information

carried by neural activity that is shared by both stimulus and choice. Thus, II can be interpreted as the part of stimulus information carried by neural activity that is also choice information. In this interpretation, II has been applied to sensory neuron to investigate the extent to which the information encoded in sensory areas is relevant to form behavioral choices [56, 71, 100]. For example, it has been used to investigate whether in primary and secondary somatosensory cortices the behavioral discrimination of texture of surfaces is supported by the texture information encoded in millisecond-precise spike times or in spike rates [100, 158]. The authors found that on average similar amounts of texture information were encoded by the millisecond precise spike times and by the spike rate of neurons. However, the behavioral discrimination performance of the rat was higher when spike times provided correct texture information than when spike times provided incorrect information, whereas behavioral performance did not depend much on the correctness of the information provided in spike rates [158]. As a consequence, the amount II carried by spike times was 3 times larger than that carried by spike rates [100], demonstrating that the texture information carried by spike timing has a much larger impact on forming correct behavioral choices than the information carried by spike rates. This type of reasoning is helpful informing hypotheses about the neural code used for sensory perception [99], as it takes into account not only the amount of information encoded in neural activity but also its impact on trial-to-trial behavioral discriminations.

Here, to demonstrate the usefulness of this approach also in contexts different from sensory perception, we use II implemented in NIT to uncover the presence of preparatory motor activity in motor cortices. We applied NIT to a publicly available dataset [159] of 2P calcium-imaging recordings in anterolateral (ALM) and medial motor (MM) cortex of Thy1-GCaMP6s transgenic mice collected during a tactile delayed two alternative forced choice (2AFC) discrimination task (see Figure 10A and B). Mice were trained to discriminate a pole in an anterior or posterior location using their whiskers. The stimulus was presented for 1.2 seconds during the Sample epoch, followed by a Delay epoch of 3s for the mice to plan the action. A Go Cue indicated the Response epoch for mice to report their guess. In the original publication [159], the authors analyze these recordings with a 3-way ANOVA, including as factors selectivity to the sensory stimulus, the choice reported by the animal, and the trial outcome (correct vs incorrect discrimination). The authors found earlier choice signal in ALM than in MM, suggesting

therefore that preparatory motor activity arises first in ALM than in MM. The ANOVA analysis does not include non-linear tuning effects, and does not per se provide a quantification of the values available for single trial discrimination. These issues can be better addressed with information theory. We first computed, using Shannon Information (Equation 1), the amount of stimulus and choice information carried by the activity of each neuron in short time windows (1 imaging frame, 70 ms) as function of time during the task. Such information values, averaged over all neurons imaged in each area, are reported in Figure 10C. We were particularly interested in signals at the beginning of the trial, because they inform more about preparatory activity. In the initial part of the trial (the end of the sample period and the early delay phase), neurons in both areas carried information about both stimulus and choice, with comparable values of stimulus and choice information in ALM and much higher values of stimulus information in MM. Neural activity related to movement preparation can be identified as an early genuinely choice-selective neural signal. However, given that choice and stimulus in each trial are correlated (because the animal performed the task 74% correct, it is possible to predict choice from stimulus), the presence of choice information in neural activity may reflect in full or in part the fact that neurons are actually selective to the stimulus and this in turns make neurons choice selective. To establish the presence of preparatory activity it is thus important to compute presence of pure choice information that cannot be explained by the tuning of stimuli. The formalism of II allows a principled and powerful definition of such pure choice information. II, as explained above, quantifies the amount of information carried by neural activity that is shared by both stimulus and choice. Thus, it quantifies the part of choice information carried by neural activity that is also stimulus information. As a consequence, the difference between II and choice information can be taken as a pure choice information measure, that is a measure of the amount of choice information in neural activity that cannot be explained by the tuning of neurons to stimulus. Figure 10D plots the time course of the average amount of instantaneous pure choice information carried on average by the activity of a neuron in a short time window. These results show that, compatible with the results of [159], the pure choice information is present (that is, larger than zero) at approximately 2 s after the pole removal in ALM, but it is not present until 2 seconds later (end of delay epoch) in MM. These results confirm those reported by [159] in a new way that also incorporates the effect of possible non-linearities of tuning of individual neurons.

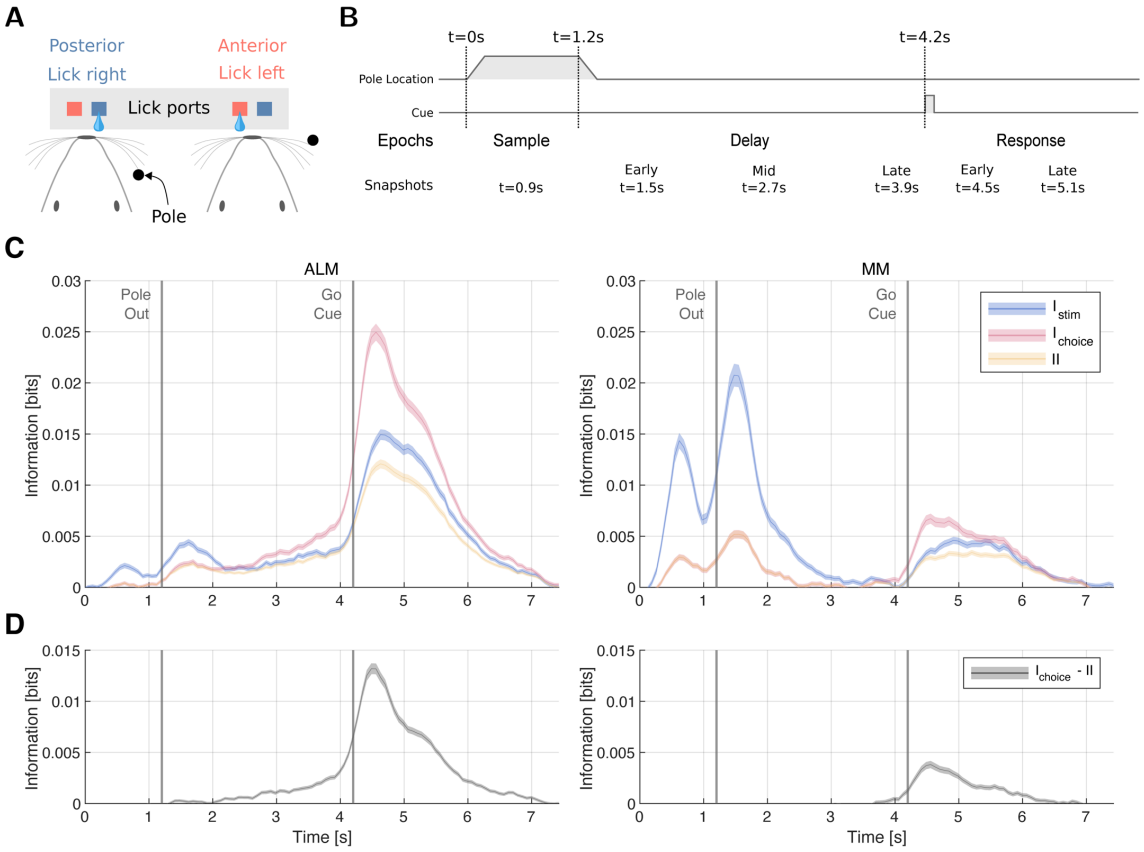


**Fig. 10: Identifying pure choice information with intersection information. Validation of performance of spiking activity metrics based on $\Delta F/F$ in recovering stimulus information on experimental data.** **(A)** Sketch of task. Mice had to lick the right port when the pole was in a posterior location while when in an anterior location, they had to lick the left pole. **(B)** Trial was structured into three different epochs. During the sample epoch (1.2 seconds), the stimulus was provided to the mice. A subsequent delay epoch (3 seconds) without stimulus preceded the Go Cue auditory signal, that initiates the response epoch, in which the mice must report by licking. **(C)** Stimulus, choice, and intersection information over time averaged across neurons computed using 2 bins. Values are bias corrected. Note that we estimated the bias using the average information values found in the pre-stimulus window. **(D)** The difference between choice and intersection information is reported as a proxy of pure choice information measure. Panels (A) and (B) redrawn from Ref [159].

# 3 Discussion

The high relevance of information theory for the analysis of neural data calls for open-source, comprehensive, and well documented software packages tailored for neuroscience applications. Here we provide a new such toolbox, NIT, constructed to meet the requirements of the contemporary systems-level neuroscience community. In what follows, we discuss the specific advances of NIT with respect to existing toolboxes and the implications and relevance of our work for neuroscience.

## 3.1 The breadth of algorithms implemented in NIT can address timely questions in systems neuroscience

Analysis of activity of populations of neurons recorded during the presentation of sensory stimuli and/or performance of cognitive tasks is central to the study of neural coding. Over the last decade, the emphasis of neural coding has shifted from considering purely encoding of sensory information to studying how the encoded information informs choices and behavior [99]. Other prominent current area of investigation include the study of the transmission of information between different brain areas, and the investigation of how functions of the brain emerge from interactions among neurons in larger and larger populations [52]. Compared to current information toolboxes, our toolbox adds several important elements to tackle these problems.

NIT supports research on the relevance of neural activity to inform behavioral choices by implementing measures of Intersection Information (II) [99, 100]. II has been proposed and used principally as a measure of how much of the sensory information encoded in neural activity is used to inform choices [56, 71, 99, 100]. This has led to redefine the concept of neural code as the set of features not only carrying sensory information, but also used to drive appropriate behavior [99]. Here, in our application to calcium imaging data (Figure 10), we showed how II can be used to address more questions about neural coding than originally proposed. We showed how II can be used to individuate pure choice signals which are not related to stimulus coding. This is of importance in tasks in which sensory signals are associated with the request to executed specific motor programs, such as turning or licking in a certain direction upon the presentation of a certain sensory stimulus.

NIT supports research on transmission of information across areas by implementing directed measures of information transfer, including both Transfer Entropy and Directed Information [101, 102] and it allows the computation of more refined recent measures based on PID [107, 108].

NIT supports research on the emergent properties of population codes by implementing tools that quantify the role of correlations for creating redundancies and synergies, such as those based on interaction information and the information breakdown [37, 91, 92] and those based on PID [66, 160]. Moreover, NIT implements tools that make analyses scalable to large populations, including

unsupervised and supervised advanced dimensionality reduction tools, such as regularized GLM classifiers [56, 115, 116], regularized SVM classifiers [118, 121], and space-by-time Non-Negative Matrix Factorization [122, 161]).

Our public, open source, release of the full NIT code will also contribute to the broad effort towards more effective and reproducible neuroscience, through standardization of tools and methods [162] of which open source analysis software is a core component [163, 164]. In this respect, the integration of NIT with other well established analysis pipelines is facilitated by the MATLAB front-end, which can be directly interfaced with Python through the MATLAB Engine API for Python.

### 3.1.1 Comparisons with existing information theoretic toolboxes for neuroscience

The breadth of use of information theory in neuroscience have been supported by several excellent and impactful toolboxes. It is thus of interest to discuss what NIT adds to this existing toolset. Recent work by Timme and Lapish [46] offers an extensive review of existing IT analysis software packages. We have further complemented their work with an updated overview (Table 1). Of the 12 packages reviewed in Timme and Lapish [46], none satisfied simultaneously the following requirements: being applicable to both discrete and continuous data, providing means for significance testing and correction for limited sampling bias, and implementing calculation of information-theoretic measures beyond MI and transfer entropy (e.g., those based on PIDs). NIT simultaneously implements all these features.

The NITT Neuroscience Information Theory Toolbox [46] is, among those previously available, one of the most complete in terms of information quantities offered. However, like others listed in Table 1, it lacks limited sampling bias correction. This is not a problem when considering quantities that do not require the computation of stimulus specific distributions of neural responses, such as entropy and TE. Lack of bias corrections instead becomes a major problem for studies of coding of sensory or choice variables, as they require estimation of stimulus-related information variables that are based on calculations of stimulus-specific response probabilities. In such cases, stimulus-specific information values are dominated by the bias, if not bias corrected. A lack of bias corrections makes it impossible to meaningfully compare the amount of information carried

by neural representations with different dimensionality such as spike times vs spike rates [35, 165] or single neurons vs population responses. The JIDT toolbox [48] also offers extensive sets of IT measures, although (like the NITT) it lacks methods for dimensionality reduction that are useful e.g. to apply IT to large populations. Other toolboxes [106, 166] are specialized on transfer entropy and are thus suitable for study information communication but not information encoding. Finally, some other toolboxes [47] are effective for specific distributions of neural activity, such as the case of Gaussian interactions which are relevant for mass measures of activity, but are difficult to apply to measures with single cell resolution for which statistics and interactions are not well described by Gaussian distributions.

We made an effort to improve computational performance in NIT, designing it to maximize efficiency and scalability. This optimized design strategy resulted in fast computational times compared with other state- of-the-art open access codes. We benchmarked our toolbox against NITT [46] on a single MI calculation, with bootstrap null distribution estimation, obtaining on average 50 times faster computation times with NIT compared to NITT.

NIT does have limitations, which we plan to address in ongoing and future updates. NIT still lacks computation of useful quantities, such as maximum entropy (ME) models, which are useful to determine the order of interactions among neurons [52, 167]. ME models are present in some specialized toolboxes [168]. Further, NIT includes standard and widely used non-parametric hypothesis testing methods, but does not yet include group statistics, which to the best of our knowledge among information theoretic toolboxes has been only implemented in FRITES [49]. However, the output of NIT analyses can be easily used as input to group statistics toolboxes [49]. Further, the study of PID is a burgeoning field with many measures and advances being elaborated [66, 97, 167, 169]. While NIT implements some of the most established PID quantities, it will be important to keep it updated to include more PID developments and to interface with new PID software.

### 3.1.2 Validations and recommendations for the analysis of calcium imaging

The methods presented in NIT are applicable to any kind of neuroscience recordings, both discrete and continuous. Given that the plug-in binning estimators presented here have been extensively

| Toolbox | Information Measure | Data Types | Significance Testing | Probability Estimation Methods | Bias Correction | Dimensionality Reduction Methods | Language |
|---|---|---|---|---|---|---|---|
| NIT – this paper | Entropy<br>Mutual information<br>Transfer entropy<br>Information breakdown<br>Partial information decomposition<br>Intersection information<br>Feature information transfer | Discrete and continuous | Non-parametric | Binning (several methods)<br>Gaussian fit<br>Parametric copula (Gaussian, Clayton, student)<br>Non-parametric copula | Yes | Yes | MATLAB front-end interfaceable with Python through MATLAB Engine API for Python |
| Information Breakdown Toolbox [43] | Entropy<br>Mutual information<br>Transfer entropy<br>Information breakdown | Discrete and continuous | Non-parametric | Binning (several methods)<br>Gaussian fit | Yes | No | MATLAB |
| Gaussian copula mutual information [47] | Entropy<br>Mutual information | Discrete and continuous | No | Gaussian Copula | Yes | No | MATLAB and Python |
| Neuroscience information theory toolbox [46] | Entropy<br>Mutual information<br>Transfer entropy<br>Partial information decomposition<br>Information transmission | Discrete and continuous | No | Binning (several methods) | No | No | MATLAB |
| JIDT [48] | Entropy<br>Mutual information<br>Transfer entropy | Discrete and continuous | Non-parametric | Binning<br>Kernel-based<br>Gaussian fit | No | No | JAVA (with Python and MATLAB wrappers) |
| FRITES [49] | Entropy<br>Mutual information<br>Transfer entropy | Discrete and continuous | Non-parametric<br>Group stats | Binning (equi-spaced)<br>Gaussian copula | Yes | No | Python |
| Inform [170] | Entropy<br>Mutual information<br>Transfer entropy | Discrete | No | Binning (several methods) | No | No | C (with Python, Julia, R and Mathematica wrappers) |
| Transfer entropy toolbox [106] | Transfer entropy | Spike trains | No | No | No | No | MATLAB |
| TRENTOOL [166] | Transfer Entropy | Continuous | Non-parametric<br>Group stats | Kernel-based | Yes | No | MATLAB |
| MuTE [171] | Transfer Entropy | Continuous | Non-parametric | Binning (equi-spaced)<br>Gaussian fit<br>Kernel-based | Yes | No | MATLAB |
| ToolConnect [172] | Entropy<br>Transfer entropy | Spike trains | No | No | No | No | C |
| STAToolkit [173] | Entropy<br>Mutual information | Spike trains | Non-parametric | Binning | Yes | No | MATLAB (with .mex files) |
| PyEntropy [168] | Entropy<br>Mutual information<br>Maximum entropy models | Discrete and continuous | No | Binning (several methods)<br>Shrink estimator | Yes | No | Python |
| ITE Toolbox [174] | Entropy<br>Mutual information | Discrete and continuous | No | Kernel-based | No | No | MATLAB and Python |
| DIT [175] | Entropy<br>Mutual information<br>Partial information decomposition | Discrete | No | No | No | No | Python |
| Climer and Dombeck [23] | SMGM Information [87] | Discrete and continuous | No | No | No | No | MATLAB |

**Table 1: Comparison with existing information theoretic toolboxes.** If the toolbox computes quantities that are defined as simple linear combinations of entropies or mutual information, for brevity we list them under entropy or mutual information.

and successfully validated on electrophysiological data (from spike trains, to LFP and EEG), in this study we focused on validating the information-theoretical analysis of 2P calcium imaging data. 2P imaging signals are potentially more challenging than electrophysiological ones to analyze with information theory, because of the lower SNR and temporal resolution. Moreover, the problem of how to recover from calcium traces as much information as possible about external stimuli or about the underlying spiking activity of the imaged neurons has not been systematically studied yet.

We addressed these issues using a thorough analysis of synthetic calcium imaging traces, generated through a biophysically plausible single-compartment model of cytosolic calcium dynamics. Specifically, we assessed the effect of the calcium indicator (GCaMP6f vs GCaMP6s),

imaging frame rate, SNR, response profile shape, and spike rate modulation by the stimulus on the stimulus information computed from the simulated calcium signal. We found that estimates of MI from the $\Delta F/F$ signal depended relatively weakly on the imaging frame rate and SNR. However, the amount of MI that could be obtained from calcium fluorescence traces is the temporal shape of the neuronal response. A tonic neuronal response transfers more information in the calcium signal compared to a phasic one, particularly when using an indicator with slow decay time and high dynamic range (GCaMP6s). We have further observed that, when the neuron encodes the stimulus in a phasic way at high firing rates, the calcium signal can occasionally encode more stimulus information than the time-averaged spike rate (Figure 6). The reason for this counterintuitive finding is that in this condition spiking activity is concentrated within a limited time interval and thus knowledge of when spike times are more informative adds information, and that the nonlinearities of calcium dynamics emphasize the signal in this high-firing high-information region and deemphasize the signal in the low-firing low information region, thereby achieving more information than the time-average spike rate which instead weighs all spikes equally regardless of when they were fired.

Furthermore, we have proposed a new single-trial calcium metric, based on the inversion of the forward model that we have used for the generation of synthetic calcium traces, for the estimation of calcium concentration in the cell given a $\Delta F/F$ trace. This approach was inspired previous work [176] inferring action potentials by building an inverse model of membrane potential from calcium imaging signals. We assessed the performance of this single-trial calcium metric for computing information from calcium data, and we compared it with other widely used strategies for quantification of single trial $\Delta F/F$ responses. We found that, across all simulation conditions examined, the newly proposed estimated calcium and the linear deconvolution of the $\Delta F/F$ trace with a decaying exponential were the two single trial calcium response quantification that allowed to extract more information (about external stimuli or about the underlying spike rates). Other considered quantifications of single trial calcium responses (max $\Delta F/F$, mean/integral $\Delta F/F$, OASIS) extracted less information. These results were confirmed on experimental data coming from four independent datasets – including both GCaMP6f and GCaMP6s signals simultaneously acquired on individual cells together with juxtasomal electrophysiological recordings. Careful choice of single-trial quantifications of calcium signals can, thus,

significantly increase the amount of information retrieved, and we propose a new and efficient metric to do so. Importantly, we compared different information computation methods, all implemented in NIT, to compute information from calcium data. We found that the non-parametric copula-based estimator for mutual information [88] was the one working best, outperforming both binned estimators and parametric Gaussian copulas in terms of data robustness and accuracy of the estimation. While the non-parametric copula comes at the expense of major increase of computing time, it should be recommended for calcium data whenever its computation is practically feasible.

A result of importance of our simulations and real data analysis was that, when proper quantification and algorithms were applied, we could recover surprisingly large amounts of information from calcium imaging. In simulations, the amount of stimulus information obtained from realistically simulated calcium imaging traces was > 50% of the stimulus information encoded in the simulated spike trains when effective single-trial calcium metric were applied (Fig 7B). In both simulated and real data, a relatively large amount of information about the underlying spike rate could be recovered from the calcium traces when using appropriate calcium metrics and algorithms (Figs 7D,9). These results illustrate the power of calcium imaging for studying population activity and the importance of coupling it with advanced information theoretic and signal extraction methods.

Climer and Dombeck [23] have recently discussed the application to calcium imaging of a specific information metric termed SMGM. This metric has been first introduced by Skaggs et al. [87] for electrophysiological data and is often used in the literature for hippocampal place field quantification. It has been shown [177] that, when applied to spike trains, the SMGM metric approximates well the full information content of a spike train only when the average number of spikes per trials is much smaller than 1 (i.e. very low firing rates or very short time windows) and that the correlations between spikes are small enough so that the firing statistics is close to that of a Poisson process. Using the SMGM metric with the $\Delta F/F$ signal as a proxy of the information carried by the underlying spike rates rate additionally assumes that a constant proportionality exists between the firing rate and fluorescence signal for a given indicator. However, there are known non-linearities between spike rate and fluorescence. Using MI to extract information from calcium traces as a proxy of information from spike rates does not require the assumption of a

linearity between spike rates and calcium fluorescence, because MI is insensitive to monotonic non-linearities in the transformation between variables, and it does not require the assumption that neuron fire at very low rates with Poisson statistics. Based on these considerations, we recommend application of SMGM to estimate information from calcium imaging data only when there is an expectation of linearity between spike rates and calcium responses and of very low firing rates of neurons. Estimations made using MI are instead valid and applicable under more general circumstances.

# 4 Materials and Methods

## 4.1 Details of the performed parametric simulation sweep

Below are listed the values considered for each of the variables considered in the parametric sweep of simulations of neural activity and calcium imaging traces.

- Imaging frame rate: 5, 10, 100 Hz.
- SNR: 5, 9, 15.
- PSTH shape: Tonic (gaussian-shaped with peak at 0.25s over a 1s trial duration, standart deviation 0.01 s), phasic (uniform distribution over time).
- Stimulus modulation of neuron mean firing rate:
  - 1Hz–2Hz: LowMI, LowSR
  - 12Hz–13Hz: LowMI, HighSR
  - 2Hz–12Hz: HighMI
- Indicator: GCaMP6f, GCaMP6s.
- Number of trials per stimulus: [5, 10, 20, 30, 40, 50, 60, 80, 100, 200, 400].

## 4.2 Mutual Information (Direct plug-in method)

$MI(S;R)$ has been calculated using Equation 1, where the marginal and joint probabilities have been calculated by simply counting the number of occurrences of the discrete values of $R$ and $S$

across repeated presentations of the stimulus. If variables $R$ and $S$ were continuous, they were discretized using binning routines. The binning strategy and number of bins used for each specific analysis using direct plug-in method are reported in the main text, together with the use of bias correction method used for the specific analysis.

### 4.3 Mutual Information (Non-parametric copula)

We estimated the mutual information between two variables $R$ and $S$ using the non-parametric copula approached presented in [88]. Copula is defined as the probability function between the CDF's of the marginal variables $U_R \sim \text{CDF}(R)$ and $U_S \sim \text{CDF}(S)$ and it captures the general correlation structure of the joint density function between variables. To compute the mutual information $MI(S;R)$, we use the fact that it is related to the copula entropy as:

$$MI(R;S) = -H(C(U_R, U_S)) \tag{6}$$

Where $C(U_R, U_S)$ is the joint density function of CDF variables $U_R$ and $U_S$ . To compute the copula density, we used the same analytic solution for a local likelihood kernel estimation of the CDF values after optimizing the bandwidth using a genetic optimization developed in Safaai et al. [88].

We then estimated the copula density over the whole space of CDF's $(U_R, U_S)$ using the optimized kernels and on a grid of size $k$ which defines the resolution of density estimation. We normally used $k = 50$ or $k = 100$ in our calculation and the change did not make significant difference on our results.

After estimating the copula density on the grid, we generated correlated samples of data by first computing the conditional cumulative copula density by integrating the copula density over the grid:

$$C(U_R|u_S) = \int_0^{u_S} C(v, u_S)dv \tag{7}$$

Which is a uniform distribution. Using the fact that the marginal distribution of a CDF distribution

is uniform, the 2-dimensional correlated samples can be generated as follows:

$$u_S = v_S \tag{8}$$

$$U_R = C^{-1}(v_R|v_S) \tag{9}$$

Where $v_R$ and $v_S$ are independent samples from the uniform distribution $(v_R, v_S) \sim \mathcal{U}$.We then used these samples to estimate the copula entropy, using classical Monte-Carlo approach after expressing the entropy as the expectation over copula density $H(C) = -E\left[\log C(V_R, V_S)\right]$. For the case in which one of the variables is discrete, we first transform the variable into the continuous domain by adding an appropriate noise which as it was shown in Safaai et al. [88].

## 4.4 Mutual Information (Parametric copula)

We implemented several algorithms for mutual information estimation using parametric copulas that have already been introduced in neuroscience [47, 87]. Full details are contained in the software documentation. In brief, we adapted our algorithms from those in [87]. For continuous margins, we provide implementations of the normal and the gamma distributions. For discrete margins, we provide the Poisson, binomial and negative binomial distributions. We provide the Gaussian, student and Clayton bivariate copula families as well as rotation transformed Clayton families.

## 4.5 Generation of synthetc calcium imaging traces

### 4.5.1 Convolution with a double exponential kernel

Fluorescent signal was generated as a convolution of the input spike train with a double exponential kernel in the form:

$$A\left(1 - e^{\frac{-\tau}{\tau_{\text{on}}}}\right) e^{\frac{-\tau}{\tau_{\text{off}}}} \tag{10}$$

| | GCaMP6f | GCaMP6s |
|---|---|---|
| A | 0.39 | 0.51 |
| $\tau_{\text{on}}$ | 0.03 | 0.14 |
| $\tau_{\text{off}}$ | 0.09 | 0.37 |

**Table 2: Used constants for the synthetic trace generation through a double exponential kernel.**

Chen et al. [137] report values of peak amplitude, peak time and half decay time for both GCaMP6f and GCaMP6s in mouse V1 in vivo experiments. Those values are related to the constants $A$, $\tau_{\text{on}}$ $\tau_{\text{off}}$ defined above, and have been defined through an iterative optimization to generate a double exponential kernel with the same peak amplitude, peak time and half decay time than reported in literature. Values used of the three constants for the two indicators are reported in Table 2.

Gaussian white noise with given standard deviation is added to the convolved trace to generate the synthetic calcium imaging trace with given SNR.

### 4.5.2 Biophysically plausible single compartmental model

Evolution of cytosolic calcium concentration [Ca] is modelled trough the following differential equation [135]:

$$\frac{d[Ca(t)]}{dt} = \frac{-v_{\text{max}}\frac{A}{V}\left(\frac{[Ca(t)]}{[Ca(t)]+K_M} - \frac{[Ca]_{\text{rest}}}{[Ca]_{\text{rest}}+K_M}\right) + \frac{\Delta[Ca]_{\text{AP}}\delta(t-t_{\text{AP}})}{dt}}{1+k_s+k_B(t)} \tag{11}$$

Where $v_{\text{max}}$ is the maximum efflux rate per unit area of the cell membrane, $A$ is the membrane area, $V$ is the compartment volume, $K_M$ is the concentration at which extrusion is half maximal, $\Delta[Ca]_{\text{AP}}$ is the amount of calcium intake following an action potential, $\delta$ is Dirac's delta, $t_{\text{AP}}$ are the times of action potentials, $k_s$ is the binding ratio of the endogenous [Ca] buffers, and $k_B$ is the binding ratio of the exogenous buffers (the indicator itself). The latter is not a model constant and, for the case of cooperative binding, is defined as [178]:

$$k_B = [B]_T \frac{n[Ca(t)]^{n-1}K_d^n}{\left([Ca(t)]^n + K_d^n\right)^2} \tag{12}$$

Where $[B]_T$ is the concentration of the indicator, $n$ is the Hill coefficient, $K_d$ is the dissociation

constant of the indicator.

Equation 11 contains two non-linear terms: a saturable mechanism for calcium extrusion from the cytoplasm (first term at the numerator on the right-hand side). Measured values of $v_{\text{max}}$ are hardly available in literature. It is more common to find estimates of the extrusion rate $\gamma$ in case of a linear extrusion mechanism $Ca(t)_{\text{out}} = \gamma\left([Ca(t)] - [Ca]_{\text{rest}}\right)$ [178]. We have thus specified $v_{\text{max}}$ so that the extrusion rate would match $\gamma = 1200\ [1/s]$ in the surroundings of $[Ca(t)] = [Ca]_{\text{rest}}$.

Time integration of Equation 11 allows to obtain the time trace of free cytosolic calcium in the cell. The concentration of indicator bound calcium $[CaB(t)]$ has been obtained through integration of:

$$\frac{d[CaB(t)]}{dt} = k_{\text{on}}[Ca(t)]^n\left([B]_T - [CaB(t)]\right) - k_{\text{off}}[CaB(t)] \tag{13}$$

Where $k_{\text{on}}$ and $k_{\text{off}}$ are the association/dissociation rates.

Once known the fraction of calcium-bound indicator, fluorescence is generated through a linear model [178]:

$$F = \left([B]_T - [CaB(t)]\right) + \phi[CaB(t)] \tag{14}$$

Where the constant $\phi$ is indicator specific and has been tuned to experimental data.

The value of baseline fluorescence $F_0$ , in resting state, steady conditions, is calculated from the resting state indicator-bound concentration using Equation 14 [178]:

$$[CaB]_{\text{rest}} = \frac{[B]_T[Ca]^n_{\text{rest}}}{[Ca]^n_{\text{rest}} + K^n_d} \tag{15}$$

The model then returns the normalized fluorescence, with the addition of white noise term:

$$\frac{\Delta F}{F_0} = \frac{F - F_0}{F_0} + WN(\sigma) \tag{16}$$

The standard deviation of the white noise has been specified to match the desired SNR for a given

| Constant | Units | Value | Method | Reference |
|---|---|---|---|---|
| $\Delta[Ca]_{AP}$ | $\mu M$ | 7.6 | From reference | [83, 135] |
| $k_s$ | $[-]$ | 110 | From reference (L2/3 pyr neuron) | [135] |
| $[B]_T$ | $\mu M$ | 10 | From reference | [86] |
| $v_{\max}$ | $\left[\frac{pMol}{cm^2 s}\right]$ | 1.8E-1 | Specified to match linear extrusion rate far from saturation in reference | [178] |
| $r$ | $\mu M$ | 5 | rom reference (L2/3 pyr neuron) | [179] |
| $A$ | $m^2$ | $A = \pi r^2$ | Equation | |
| $V$ | $m^3$ | $V = 4/3\pi r^3$ | Equation | |
| $K_M$ | $\mu M$ | 0.8 | From reference | [180] |
| $[Ca]_{\text{rest}}$ | $nM$ | 50 | From reference | [181] |

**Table 3: Model constants used in the SCM.** These constants were independent on the indicator.

| Constant | Units | Value GCaMP6f | Value GCaMP6s | Method | Reference |
|---|---|---|---|---|---|
| $n$ | $[-]$ | 2,47 | 293 | Fit to experimental data | |
| $K_d$ | $[n]$ | 375 | 144 | From reference | [137] |
| $k_{\text{on}}$ | $\text{Hz}/M^n$ | $k_{\text{on}} = k_{\text{off}}/K_d^n$ | | From reference | [178] |
| $k_{\text{off}}$ | [Hz] | 5.16 | 0.5 | Fit to experimental data | |
| $\phi$ | $[-]$ | 15.01 | 62.72 | Fit to experimental data | |

**Table 4: Indicator specific constant used in the SCM.** These constants were indicator-specific and have been determined through fitting the model on experimental data.

synthetic trace.

### 4.5.3 Fitting of the SCM to experimental data

Fitting of the single-compartment model is done in the following way (separately for each indicator considered). Among the three variables that are fit to data ($\phi, n, k_{\text{off}}$), the first one is optimized first – and independently from the other two – so that saturated indicator reaches the dynamic range reported in [137]. This is possible due to the fact that $n$ and $k_{\text{off}}$ do not impact the steady state brightness of the indicator, but only its dynamics. Simultaneous 2-photon imaging and cell-attached electrophysiology data [182] are then used to define the kinetics of the indicator binding/unbinding and its cooperativity. Given the experimentally measured spike train, and SNR of the experimental fluorescent trace, we have optimized $n$ and $k_{\text{off}}$ to reduce the root square error between the generated synthetic calcium trace and experimental data. Dataset 'data_20120521_cell5_007.mat' has been used for GCaMP6f tuning, while 'data_20120515_cell1_006.mat' has been used for GCaMP6s.

## 4.6 Definition of spiking activity metrics based on $\Delta F/F$

### 4.6.1 Max $\Delta F/F$

Values of peak $\Delta F/F$ over a defined post stimulus time interval have been calculated as follows:

$$\max(\Delta F/F) = \max(\Delta F/F(t) - \Delta F/F(0)) \tag{17}$$

### 4.6.2 Mean/integral $\Delta F/F$

Values of mean $\Delta F/F$ over a defined post stimulus time interval have been calculated as follows:

$$\text{mean}(\Delta F/F) = \text{mean}(\Delta F/F(t) - \Delta F/F(0)) \tag{18}$$

It should be noted that, throughout the text, we refer to this metric as Mean/integral $\Delta F/F$. The reason for this is that the mean and integral are related by a constant linear scaling and are de facto equivalent in information-theoretical terms. The full dataset attached to this paper contains also separate analysis for integral$(\Delta F/F)$, showing identical performance to mean$(\Delta F/F)$.

### 4.6.3 Estimated calcium

This metric of spiking activity based on the two photon imaging recordings is based on the inversion of the forward model detailed in section Biophysically plausible single compartmental model. The inversion, calculating thus [Ca] from the $\Delta F/F$ assumes that the binding/unbinding happens at chemical equilibrium. In this condition, for cooperative binding, we can write the relation between [CaB] and [Ca] as:

$$\frac{[CaB(t)]}{[B]_T} = \frac{[Ca(t)]^n}{[Ca(t)]^n + K_d^n} \tag{19}$$

Deriving both left and right-hand sides:

$$\frac{d[CaB(t)]}{dt} = \frac{nK_d^n[Ca(t)]^{n-1}[B]_T}{([Ca(t)]^n + K_d^n)^2}\frac{d[Ca(t)]}{dt} \tag{20}$$

Assuming that the generated fluorescence is a linear combination of the fractions of calcium-free [B] and calcium-bound [CaB] indicator we can write the following:

$$F(t) = [B(t)] + \phi[CaB(t)] = [B]_T - [CaB(t)] + \phi[CaB(t)] = [B]_T + \alpha[CaB(t)] \quad (21)$$

Where $\alpha = \phi - 1$. Baseline state fluorescence, thus, is:

$$F_0 = [B(t)] + \alpha[CaB]_0 \quad (22)$$

Combining equations 21 and 22 we have that:

$$\frac{\Delta F}{F}(t) = \frac{\alpha\left([CaB(t)] - [CaB]_0\right)}{[B]_T + \alpha[CaB]_0} \quad (23)$$

Deriving both left and right-hand side of equation 23 with respect to time:

$$\frac{\Delta FF(t)}{dt} = \frac{\alpha}{[B]_T + \alpha[CaB]_0}\frac{d[CaB(t)]}{dt} \quad (24)$$

Combining equations 24 and 20:

$$\frac{\Delta FF(t)}{dt} = \frac{\alpha}{[B]_T + \alpha[CaB]_0}\frac{nK_d^n[Ca(t)]^{n-1}[B_T]}{\left([Ca(t)]^n + K_d^n\right)^2}\frac{d[Ca(t)]}{dt} \quad (25)$$

Given the time trace of fluorescence, equation 23 can be used to solve for $[Ca(t)]$ once $[Ca(0)]$ and $[CaB]_0$ are known. These values have been defined through the following educated guesses. The baseline calcium-bound indicator concentration $[CaB]_0$ is taken as the steady state equilibrium concentration when $[Ca] = [Ca]_{\text{rest}}$ (using Equation 19).

In order to estimate the initial concentration of free calcium in the cell we used the following approach. Combining equations 23 and 19 we obtain:

$$\Delta F/F = \frac{\alpha \left( \frac{[B]_T [Ca(t)]^n}{[Ca(t)]^n + K_d^n} - [CaB]_0 \right)}{[B]_T + \alpha [CaB]_0} \tag{26}$$

Given $\Delta F/F$ at time zero, iterative solution of equation 26 for $[Ca(0)]$. This sets the initial conditions for time integration of equation 20.

The obtained time trace is finally deconvolved through a single decaying exponential kernel with time constant equal to the reciprocal of the unbinding rate of the indicator $k_{\text{off}}$. The mean of the deconvolved trace is reported as the estimated [Ca].

### 4.6.4 Linear deconvolution

The $\Delta F/F$ trace has been deconvolved with a decaying exponential with a decaying time constant $\tau_{\text{off}}$. The reported value of the deconvolved signal over the post stimulus time interval has been calculated as:

$$\text{Linear deconvolution} = \text{mean} \left( \frac{d\Delta F/F(t)}{dt} + \frac{\Delta F/F(t)}{\tau_{\text{off}}} \right) \tag{27}$$

Where the values of $\tau_{\text{off}}$ ($\tau_{\text{off}} = 2s$ for GCaMP6s and $\tau_{\text{off}} = 0.5s$ for GCaMP6f) have been estimated from the decay of time traces for GCaMP6 indicator reported in Chen et al. [137].

### 4.6.5 OASIS

Time trace of $\Delta F/F$ has been deconvolved using MATLAB implementation of OASIS [151] https://github.com/zhoupc/OASIS_matlab. We have used the second order auto-regressive thresholded implementation of the algorithm. This implementation imposes a minimum threshold for the deconvolved trace, effectively filtering out spurious deconvolved activity. The parameters of the auto-regressive model, the value of the threshold, as well as the SNR levels were estimated by internal functions of the toolbox. The returned value of OASIS metric over a post-stimulus window has been calculated as:

$$\text{OASIS} = \text{mean} \left( \text{OASIS deconvolved } \Delta F/F \right) \tag{28}$$

In order to avoid potential issues in using OASIS to deconvolve traces of limited duration, the time traces of $\Delta F/F$ extended for a total duration of 10s, of which the first second was stimulus modulated and the remaining part had a constant baseline SR of 0.5 Hz.

## 4.7 Definition of preparatory activity in motor cortex

Stimulus and choice instantaneous information were computed using mutual information between those variables and the neural activity over time, resulting in values of information over the trial duration. Mutual information and intersection information were computed using the direct plug-in method for computational tractability of such a large dataset. Neural activity was binned in 2 equally populated bins for every timestep.

## 4.8 Software availability

NIT source code, documentation, installation instructions and tutorials can be downloaded from the following repository: https://gitlab.com/rmaffulli/nit. Software for the realistic calcium imaging simulations can be downloaded from the following repository: https://gitlab.com/rmaffulli/casim.

# Supporting information

| Information quantity | Allowed bias correction methods |
|---|---|
| Mutual Information (direct method) | Quadratic extrapolation, Panzeri-Treves, Bootstrap correction, BUB |
| Mutual Information (non-parametric copula) | Bootstrap correction |
| Mutual Information Breakdown | Quadratic extrapolation, Panzeri-Treves, Bootstrap correction |
| Transfer Entropy | Quadratic extrapolation, Panzeri-Treves, Bootstrap correction |
| Partial Information Decomposition | Linear extrapolation, Quadratic extrapolation, Bootstrap correction |
| Intersection Information | Linear extrapolation, Quadratic extrapolation, Bootstrap correction |
| Feature Information Transfer | Linear extrapolation, Quadratic extrapolation, Bootstrap correction |

**Table 5: Compatibility matrix between information-theoretic quantities in NIT and applicable bias correction strategies.**

| | PSTH shape | FR | SNR |
|---|---|---|---|
| Low MI, low SR | $p = 2.24e-16$<br>$\omega^2 = 7.00e-2$ | $p = 3.97e-4$<br>$\omega^2 = 1.40e-2$ | $p = 7.21e-2$<br>$\omega^2 = 3.32e-3$ |
| Low MI, high SR | $p = 8.11e-48$<br>$\omega^2 = 2.08e-1$ | $p = 4.05e-1$<br>$\omega^2 = -1.70e-4$ | $p = 4.09e-1$<br>$\omega^2 = -1.85e-4$ |
| High MI | $p = 0$<br>$\omega^2 = 8.89e-1$ | $p = 9.30e-17$<br>$\omega^2 = 7.99e-3$ | $p = 5.00e-14$<br>$\omega^2 = 6.54e-3$ |

**Table 6: Table of p-values and effect sizes $\omega^2$ for data in Figure 5C.** Data have been analyzed using a separate three-ways ANOVA (considering PSTH shape, FR and SR as grouping variables) for each information level.

| | PSTH shape | Indicator |
|---|---|---|
| Low MI, low SR | $p = 4.97e-1$<br>$\omega^2 = 2.69e-3$ | $p = 4.89e-1$<br>$\omega^2 = -2.61e-3$ |
| Low MI, high SR | $p = 5.61e-1$<br>$\omega^2 = -1.66e-3$ | $p = 6.47e-1$<br>$\omega^2 = -1.98e-4$ |
| High MI | $p = 1.5e-7$<br>$\omega^2 = 4.34e-2$ | $p = 4.18e-11$<br>$\omega^2 = -5.45e-4$ |

**Table 7: Table of p-values and effect sizes $\omega^2$ for data in Figure 5D.** Data have been analyzed using a separate three-ways ANOVA (considering PSTH shape and calcium indicator as grouping variables) for each information level.

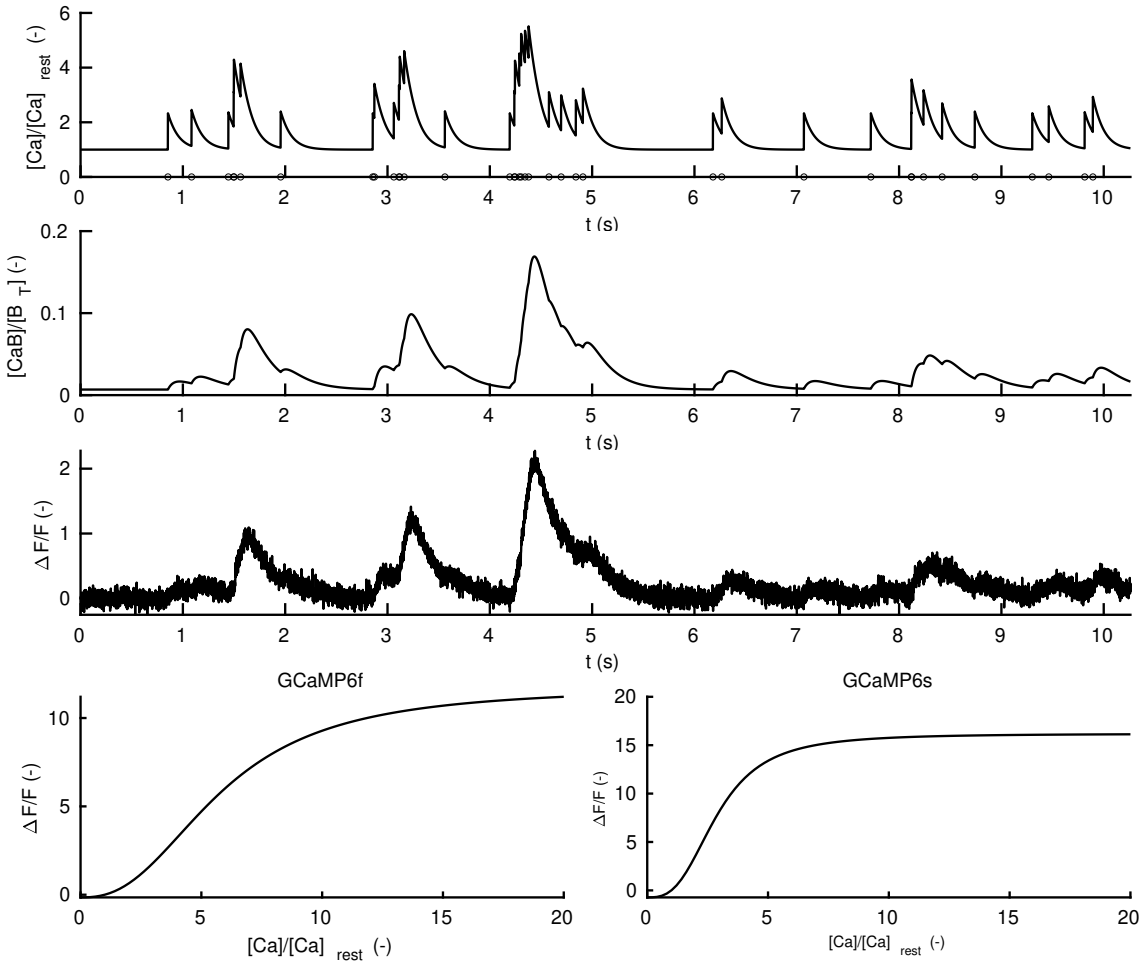


**Fig. 11: Generation of fluorescence trace in the Single Compartment Model. (A)** Top: simulated trace of relative levels of free calcium concentration in the cytoplasm with respect to resting state levels. Circles represent action potentials. Middle: simulated trace of the fraction of GCaMP indicator bound to calcium. Bottom: fluorescent trace resulting from the fractions of calcium-bound and calcium-free indicator. **(B)** Relation between generated fluorescence and free calcium concentration in the cytoplasm in chemical equilibrium conditions for both GCaMP6f and GCaMP6s in the used model.

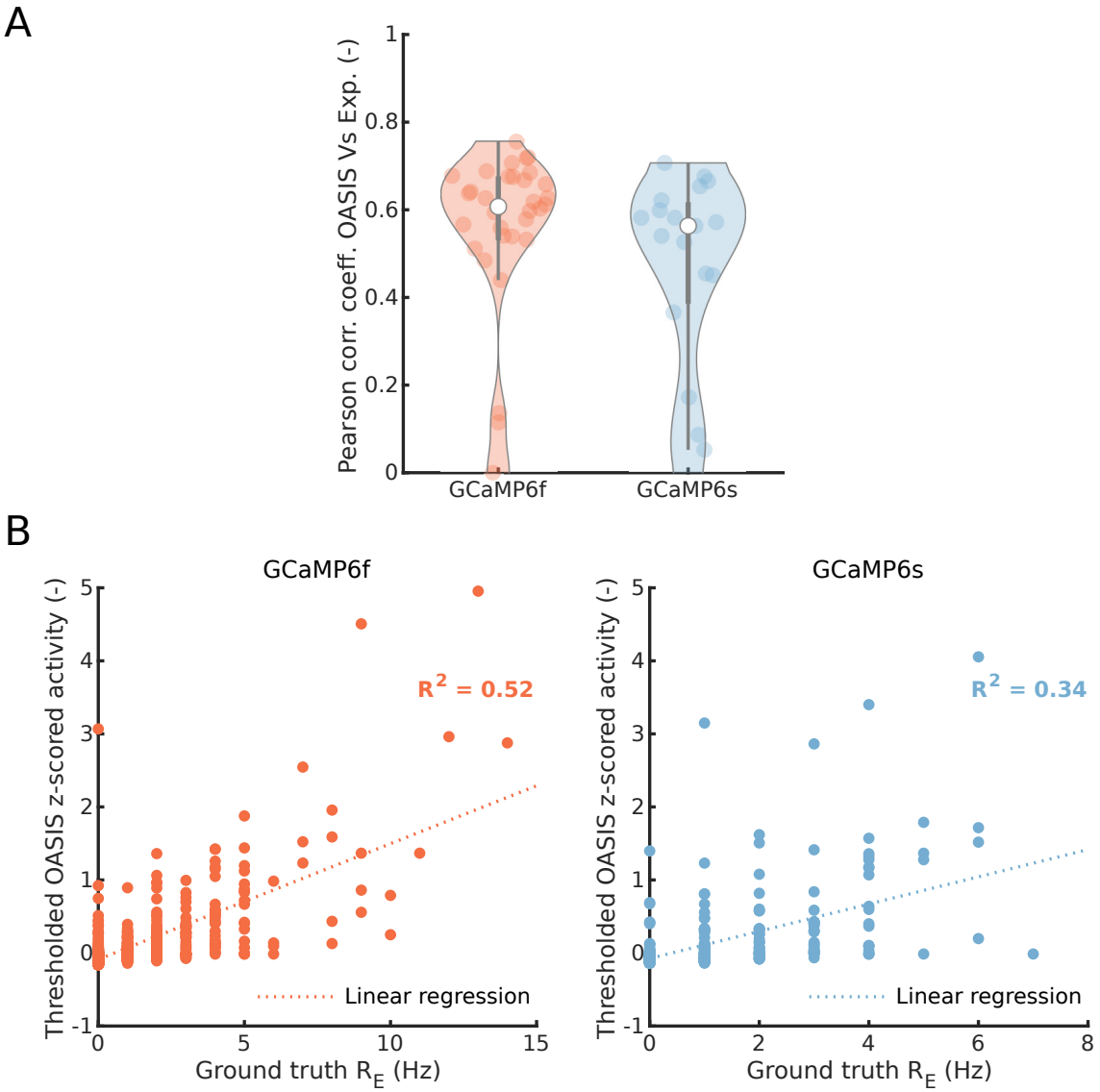


**Fig. 12: Performance of OASIS on experimental calibration dataset [182] with simultaneous calcium imaging and electrophysiology. (A)** Pearson's correlation coefficient between real and inferred spiking activity using 2nd order auto-regressive (AR) thresholded OASIS [151] (see Materials and Methods). ($N = 34$ for GCaMP6f, $N = 19$ for GCaMP6s). **(B)** Relation between z-scored inferred spiking activity in OASIS and ground truth spike rate on 1 s long windows selected randomly over the entire experimental acquisition (50 random windows per each experimental trace $N = 1700$ for GCaMP6f, $N = 950$ for GCaMP6s). Experimental data for this dataset are publicly available at: https://crcns.org/data-sets/methods/cai-1

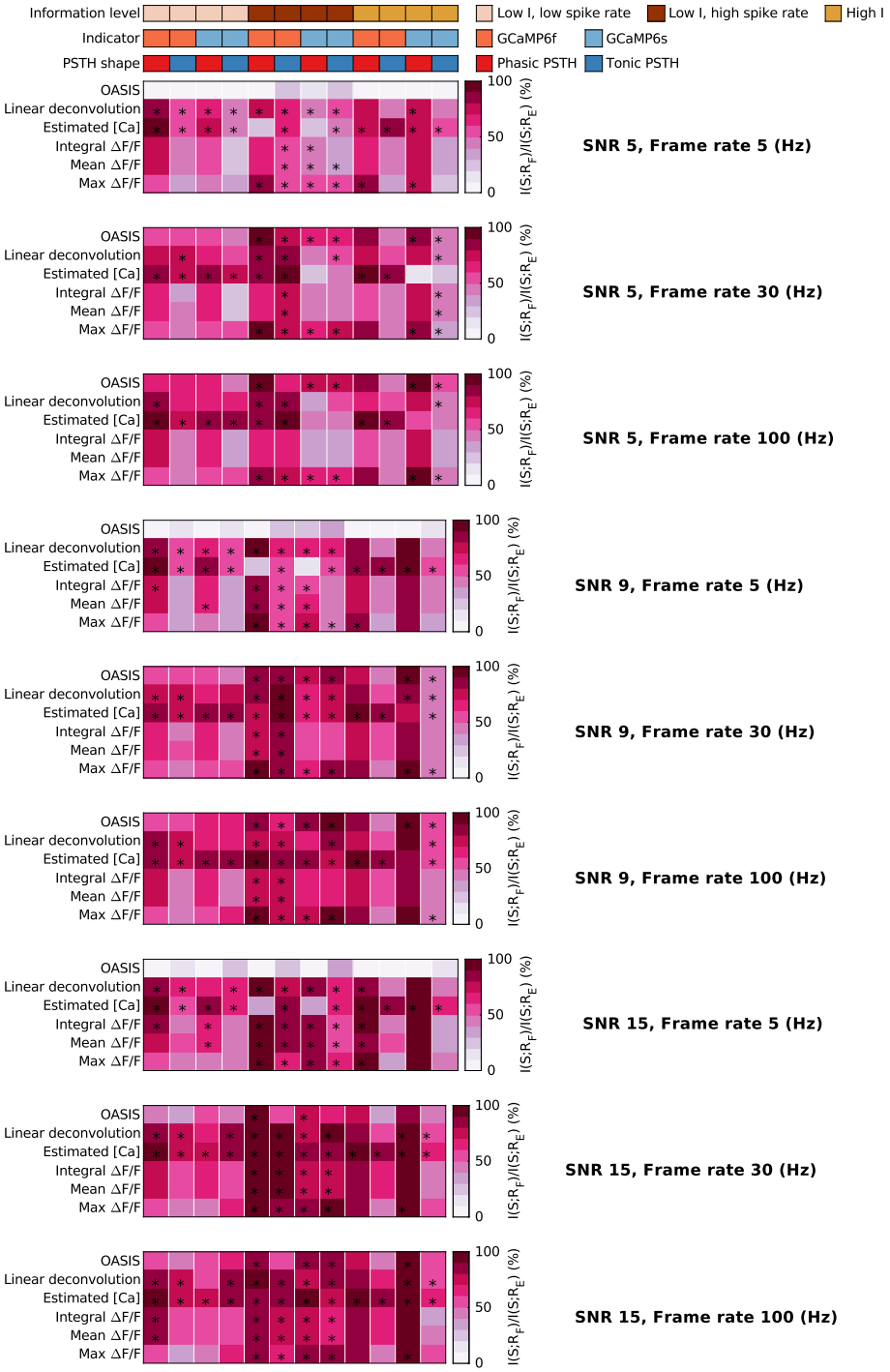


**Fig. 13: Information content in $\Delta F/F$ traces with respect to SR code.** Percentage of stimulus information retrieved by each $\Delta F/F$ metric with respect to the one contained in spike rate, in all conditions of the parametric sweep considered in the study. Values represent the average over 50 simulations. For each combination of frame rate, SNR, information level, indicator and PSTH shape, the * symbol marks the metrics with non statistically different mean ($p > 0.05$ Bonferroni corrected Kruskal-Wallis multiple comparison test) from the best performing metric at those conditions. Best performing metric is defined as the one returning the highest mean stimulus information. All data in the figure refer to simulated traces. Mutual information is evaluated using plug-in method.

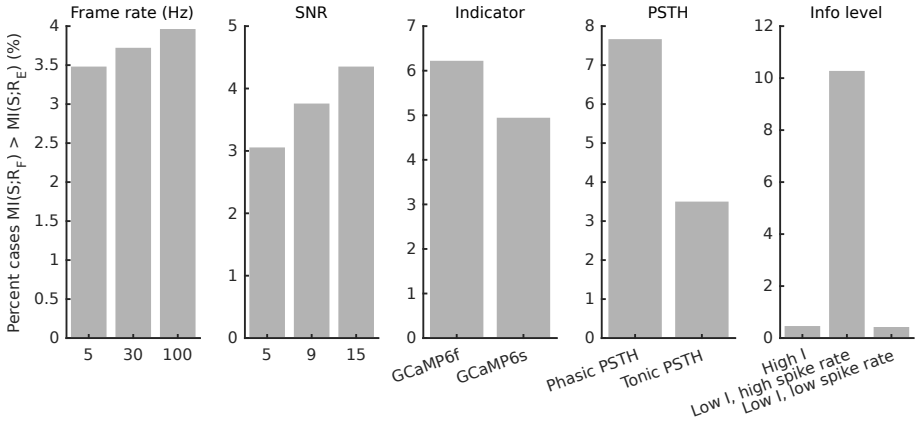


**Fig. 14: Where is MI in max $\Delta F/F$ higher than MI in SR.** Percentage of cases, across all conditions investigated in the parametric sweep, where MI in max $\Delta F/F$ has been found to be higher than the stimulus information in the spike rate code.

# References

[19] C. E. Shannon, "A mathematical theory of communication," *The Bell system technical journal*, vol. 27, no. 3, pp. 379–423, 1948.

[20] A. G. Dimitrov, A. A. Lazar, and J. D. Victor, "Information theory in neuroscience," *Journal of computational neuroscience*, vol. 30, no. 1, pp. 1–5, 2011.

[21] A. Borst and F. E. Theunissen, "Information theory and neural coding," *Nature Neuroscience*, vol. 2, no. 11, pp. 947–957, 1999. [Online]. Available: https://doi.org/10.1038/14731

[22] V. Lopes-dos Santos, S. Panzeri, C. Kayser, M. E. Diamond, and R. Q. Quiroga, "Extracting information in spike time patterns with wavelets and information theory," *Journal of Neurophysiology*, vol. 113, no. 3, pp. 1015–1033, 2015. [Online]. Available: https://journals.physiology.org/doi/abs/10.1152/jn.00380.2014

[23] J. R. Climer and D. A. Dombeck, "Information theoretic approaches to deciphering the neural code with functional fluorescence imaging," *eNeuro*, vol. 8, no. 5, pp. ENEURO.0266–21.2021, 2021. [Online]. Available: https://pubmed.ncbi.nlm.nih.gov/34433574https://www.ncbi.nlm.nih.gov/pmc/articles/PMC8474651/

[24] R. R. de Ruyter van Steveninck, G. D. Lewen, S. P. Strong, R. Koberle, and W. Bialek, "Reproducibility and variability in neural spike trains," *Science*, vol. 275, no. 5307, pp. 1805–1808, 1997. [Online]. Available: https://www.science.org/doi/abs/10.1126/science.275.5307.1805

[25] F. Rieke, D. Warland, R. d. R. Van Steveninck, and W. Bialek, *Spikes: exploring the neural code*. MIT press, 1999.

[26] R. Azeredo da Silveira and F. Rieke, "The geometry of information coding in correlated neural populations," *Annual Review of Neuroscience*, vol. 44, pp. 403–424, 2021.

[27] J. J. Atick and A. N. Redlich, "Towards a theory of early visual processing," *Neural Computation*, vol. 2, no. 3, pp. 308–320, 1990. [Online]. Available: https://doi.org/10.1162/neco.1990.2.3.308

[28] H. B. Barlow, "Possible principles underlying the transformation of sensory messages," *Sensory communication*, vol. 1, no. 01, 1961.

[29] F. Attneave, "Some informational aspects of visual perception," *Psychological Review*, vol. 61, no. 3, pp. 183–193, 1954.

[30] D. M. MacKay and W. S. McCulloch, "The limiting information capacity of a neuronal link," *The bulletin of mathematical biophysics*, vol. 14, no. 2, pp. 127–135, 1952.

[31] W. F. Młynarski and A. M. Hermundstad, "Efficient and adaptive sensory codes," *Nature Neuroscience*, vol. 24, no. 7, pp. 998–1009, 2021.

[32] S. Panzeri, R. Senatore, M. A. Montemurro, and R. S. Petersen, "Correcting for the sampling bias problem in spike train information measures," *Journal of neurophysiology*, vol. 98, no. 3, pp. 1064–1072, 2007.

[33] A. L. Fairhall, G. D. Lewen, W. Bialek, and R. R. de Ruyter van Steveninck, "Efficiency and ambiguity in an adaptive neural code," *Nature*, vol. 412, no. 6849, pp. 787–792, 2001.

[34] S. Panzeri, R. S. Petersen, S. R. Schultz, M. Lebedev, and M. E. Diamond, "The role of spike timing in the coding of stimulus location in rat somatosensory cortex," *Neuron*, vol. 29, no. 3, pp. 769–777, 2001.

[35] S. Panzeri, N. Brunel, N. K. Logothetis, and C. Kayser, "Sensory neural codes using multiplexed temporal scales," *Trends in neurosciences*, vol. 33, no. 3, pp. 111–120, 2010.

[36] S. Panzeri, S. R. Schultz, A. Treves, and E. T. Rolls, "Correlations and the encoding of information in the nervous system," *Proceedings of the Royal Society of London. Series B: Biological Sciences*, vol. 266, no. 1423, pp. 1001–1012, 1999.

[37] G. Pola, A. Thiele, K. Hoffmann, and S. Panzeri, "An exact method to quantify the information transmitted by different mechanisms of correlational coding," *Network: Computation in Neural Systems*, vol. 14, no. 1, p. 35, 2003.

[38] S. Nigam, S. Pojoga, and V. Dragoi, "Synergistic coding of visual information in columnar networks," *Neuron*, vol. 104, no. 2, pp. 402–411. e4, 2019.

[39] A. Belitski, A. Gretton, C. Magri, Y. Murayama, M. A. Montemurro, N. K. Logothetis, and S. Panzeri, "Low-frequency local field potentials and spikes in primary visual cortex convey independent visual information," *Journal of Neuroscience*, vol. 28, no. 22, pp. 5696–5709, 2008.

[40] M. A. Montemurro, M. J. Rasch, Y. Murayama, N. K. Logothetis, and S. Panzeri, "Phase-of-firing coding of natural visual stimuli in primary visual cortex," *Current biology*, vol. 18, no. 5, pp. 375–380, 2008.

[41] S. Panzeri and A. Treves, "Analytical estimates of limited sampling biases in different information measures," *Network: Computation in neural systems*, vol. 7, no. 1, p. 87, 1996.

[42] J. D. Victor, "Approaches to information-theoretic analysis of neural activity," *Biological theory*, vol. 1, no. 3, pp. 302–316, 2006.

[43] C. Magri, K. Whittingstall, V. Singh, N. K. Logothetis, and S. Panzeri, "A toolbox for the fast information analysis of multiple-site lfp, eeg and spike train recordings," *Bmc Neuroscience*, vol. 10, 2009, 538gz Times Cited:148 Cited References Count:80.

[44] C. Kayser, N. K. Logothetis, and S. Panzeri, "Visual enhancement of the information representation in auditory cortex," *Current Biology*, vol. 20, no. 1, pp. 19–24, 2010. [Online]. Available: https://www.sciencedirect.com/science/article/pii/S096098220901940X

[45] A. Belitski, S. Panzeri, C. Magri, N. K. Logothetis, and C. Kayser, "Sensory information in local field potentials and spikes from visual and auditory cortices: time scales and frequency bands," *Journal of Computational Neuroscience*, vol. 29, no. 3, pp. 533–545, 2010. [Online]. Available: https://doi.org/10.1007/s10827-010-0230-y

[46] N. M. Timme and C. Lapish, "A tutorial for information theory in neuroscience," *eneuro*, vol. 5, no. 3, 2018.

[47] R. A. Ince, B. L. Giordano, C. Kayser, G. A. Rousselet, J. Gross, and P. G. Schyns, "A statistical framework for neuroimaging data analysis based on mutual information estimated via a gaussian copula," *Human Brain Mapping*, vol. 38, no. 3, pp. 1541–1573, 2017. [Online]. Available: https://onlinelibrary.wiley.com/doi/abs/10.1002/hbm.23471

[48] J. T. Lizier, "Jidt: An information-theoretic toolkit for studying the dynamics of complex systems," *Frontiers in Robotics and AI*, vol. 1, 2014. [Online]. Available: https://www.frontiersin.org/articles/10.3389/frobt.2014.00011

[49] E. Combrisson, M. Allegra, R. Basanisi, R. A. A. Ince, B. L. Giordano, J. Bastin, and A. Brovelli, "Group-level inference of information-based measures for the analyses of cognitive brain networks

from neurophysiological data," *NeuroImage*, vol. 258, p. 119347, 2022. [Online]. Available: https://www.sciencedirect.com/science/article/pii/S1053811922004669

[50] T. D. Pereira, J. W. Shaevitz, and M. Murthy, "Quantifying behavior to understand the brain," *Nature Neuroscience*, vol. 23, no. 12, pp. 1537–1549, 2020. [Online]. Available: https://doi.org/10.1038/s41593-020-00734-z

[51] N. C. Rust and M. R. Cohen, "Priority coding in the visual system," *Nature Reviews Neuroscience*, vol. 23, no. 6, pp. 376–388, 2022. [Online]. Available: https://doi.org/10.1038/s41583-022-00582-9

[52] S. Panzeri, M. Moroni, H. Safaai, and C. D. Harvey, "The structures and functions of correlations in neural population codes," *Nature Reviews Neuroscience*, vol. 23, no. 9, pp. 551–567, 2022. [Online]. Available: https://doi.org/10.1038/s41583-022-00606-4

[53] A. T. Reid, D. B. Headley, R. D. Mill, R. Sanchez-Romero, L. Q. Uddin, D. Marinazzo, D. J. Lurie, P. A. Valdés-Sosa, S. J. Hanson, B. B. Biswal, V. Calhoun, R. A. Poldrack, and M. W. Cole, "Advancing functional connectivity research from association to causation," *Nature Neuroscience*, vol. 22, no. 11, pp. 1751–1760, 2019. [Online]. Available: https://doi.org/10.1038/s41593-019-0510-4

[54] S. Tafazoli, H. Safaai, G. De Franceschi, F. B. Rosselli, W. Vanzella, M. Riggi, F. Buffolo, S. Panzeri, and D. Zoccolan, "Emergence of transformation-tolerant representations of visual objects in rat lateral extrastriate cortex," *Elife*, vol. 6, 2017.

[55] S. Curreli, J. Bonato, S. Romanzi, S. Panzeri, and T. Fellin, "Complementary encoding of spatial information in hippocampal astrocytes," *PLoS biology*, vol. 20, no. 3, p. e3001530, 2022.

[56] C. A. Runyan, E. Piasini, S. Panzeri, and C. D. Harvey, "Distinct timescales of population coding across cortex," *Nature*, vol. 548, no. 7665, pp. 92–96, 2017.

[57] E. Froudarakis, P. Berens, A. S. Ecker, R. J. Cotton, F. H. Sinz, D. Yatsenko, P. Saggau, M. Bethge, and A. S. Tolias, "Population code in mouse v1 facilitates readout of natural scenes through increased sparseness," *Nature neuroscience*, vol. 17, no. 6, pp. 851–857, 2014.

[58] A. Giovannucci, A. Badura, B. Deverett, F. Najafi, T. D. Pereira, Z. Gao, I. Ozden, A. D. Kloth, E. Pnevmatikakis, L. Paninski, C. I. De Zeeuw, J. F. Medina, and S. S. H. Wang, "Cerebellar granule cells acquire a widespread predictive feedback signal during motor learning," *Nature Neuroscience*, vol. 20, no. 5, pp. 727–734, 2017. [Online]. Available: https://doi.org/10.1038/nn.4531

[59] N. K. Kühn and T. Gollisch, "Activity correlations between direction-selective retinal ganglion cells synergistically enhance motion decoding from complex visual scenes," *Neuron*, vol.

101, no. 5, pp. 963–976.e7, 2019, doi: 10.1016/j.neuron.2019.01.003. [Online]. Available: https://doi.org/10.1016/j.neuron.2019.01.003

[60] T. O. Sharpee and J. A. Berkowitz, "Linking neural responses to behavior with information-preserving population vectors," *Current Opinion in Behavioral Sciences*, vol. 29, pp. 37–44, 2019. [Online]. Available: https://www.sciencedirect.com/science/article/pii/S2352154618302092

[61] G. Iurilli and S. R. Datta, "Population coding in an innately relevant olfactory area," *Neuron*, vol. 93, no. 5, pp. 1180–1197.e7, 2017. [Online]. Available: https://www.sciencedirect.com/science/article/pii/S0896627317300946

[62] R. Rossi-Pool, A. Zainos, M. Alvarez, G. Diaz-deLeon, and R. Romo, "A continuum of invariant sensory and behavioral-context perceptual coding in secondary somatosensory cortex," *Nature Communications*, vol. 12, no. 1, p. 2000, 2021. [Online]. Available: https://doi.org/10.1038/s41467-021-22321-x

[63] E. Granot-Atedgi, G. Tkačik, R. Segev, and E. Schneidman, "Stimulus-dependent maximum entropy models of neural population codes," *PLOS Computational Biology*, vol. 9, no. 3, p. e1002922, 2013. [Online]. Available: https://doi.org/10.1371/journal.pcbi.1002922

[64] M. Wibral, R. Vicente, and J. T. Lizier, *Directed information measures in neuroscience*. Springer, 2014, vol. 724.

[65] M. Besserve, S. C. Lowe, N. K. Logothetis, B. Schölkopf, and S. Panzeri, "Shifts of gamma phase across primary visual cortical sites reflect dynamic stimulus-modulated information transfer," *PLOS Biology*, vol. 13, no. 9, p. e1002257, 2015. [Online]. Available: https://doi.org/10.1371/journal.pbio.1002257

[66] A. I. Luppi, P. A. Mediano, F. E. Rosas, N. Holland, T. D. Fryer, J. T. O'Brien, J. B. Rowe, D. K. Menon, D. Bor, and E. A. Stamatakis, "A synergistic core for human brain evolution and cognition," *Nature Neuroscience*, vol. 25, no. 6, pp. 771–782, 2022.

[67] N. Colenbier, F. Van de Steen, L. Q. Uddin, R. A. Poldrack, V. D. Calhoun, and D. Marinazzo, "Disambiguating the role of blood flow and global signal with partial information decomposition," *NeuroImage*, vol. 213, p. 116699, 2020. [Online]. Available: https://www.sciencedirect.com/science/article/pii/S1053811920301865

[68] D. Gutierrez-Barragan, N. A. Singh, F. G. Alvino, L. Coletta, F. Rocchi, E. De Guzman, A. Galbusera, M. Uboldi, S. Panzeri, and A. Gozzi, "Unique spatiotemporal fmri dynamics in the awake mouse brain," *Current Biology*, vol. 32, no. 3, pp. 631–644.e6, 2022. [Online]. Available: https://www.sciencedirect.com/science/article/pii/S0960982221016912

[69] P. L. Williams and R. D. Beer, "Nonnegative decomposition of multivariate information," *arXiv preprint arXiv:1004.2515*, 2010.

[70] G. Pica, E. Piasini, D. Chicharro, and S. Panzeri, "Invariant components of synergy, redundancy, and unique information among three variables," *Entropy*, vol. 19, no. 9, p. 451, 2017.

[71] N. A. Francis, S. Mukherjee, L. Koçillari, S. Panzeri, B. Babadi, and P. O. Kanold, "Sequential transmission of task-relevant information in cortical neuronal networks," *Cell Reports*, vol. 39, no. 9, p. 110878, 2022. [Online]. Available: https://www.sciencedirect.com/science/article/pii/S2211124722006532

[72] F. Helmchen and W. Denk, "Deep tissue two-photon microscopy," *Nature Methods*, vol. 2, no. 12, pp. 932–940, 2005. [Online]. Available: https://doi.org/10.1038/nmeth818

[73] W. Denk, J. H. Strickler, and W. W. Webb, "Two-photon laser scanning fluorescence microscopy," *Science*, vol. 248, no. 4951, pp. 73–76, 1990. [Online]. Available: https://www.science.org/doi/abs/10.1126/science.2321027

[74] W. Denk and K. Svoboda, "Photon upmanship: why multiphoton imaging is more than a gimmick," *Neuron*, vol. 18, no. 3, pp. 351–357, 1997.

[75] W. Denk, K. R. Delaney, A. Gelperin, D. Kleinfeld, B. W. Strowbridge, D. W. Tank, and R. Yuste, "Anatomical and functional imaging of neurons using 2-photon laser scanning microscopy," *Journal of Neuroscience Methods*, vol. 54, no. 2, pp. 151–162, 1994. [Online]. Available: https://www.sciencedirect.com/science/article/pii/0165027094901899

[76] D. Huber, D. A. Gutnisky, S. Peron, D. H. O'Connor, J. S. Wiegert, L. Tian, T. G. Oertner, L. L. Looger, and K. Svoboda, "Multiple dynamic representations in the motor cortex during sensorimotor learning," *Nature*, vol. 484, no. 7395, pp. 473–478, 2012. [Online]. Available: https://doi.org/10.1038/nature11039

[77] J. N. D. Kerr, C. P. J. de Kock, D. S. Greenberg, R. M. Bruno, B. Sakmann, and F. Helmchen, "Spatial organization of neuronal population responses in layer 2/3 of rat barrel cortex," *The Journal of Neuroscience*, vol. 27, no. 48, pp. 13 316–13 328, 2007. [Online]. Available: https://www.jneurosci.org/content/jneuro/27/48/13316.full.pdf

[78] L. Carrillo-Reid, S. Han, W. Yang, A. Akrouh, and R. Yuste, "Controlling visually guided behavior by holographic recalling of cortical ensembles," *Cell*, vol. 178, no. 2, pp. 447–457.e5, 2019, doi: 10.1016/j.cell.2019.05.045. [Online]. Available: https://doi.org/10.1016/j.cell.2019.05.045

[79] C. D. Harvey, P. Coen, and D. W. Tank, "Choice-specific sequences in parietal cortex during a virtual-navigation decision task," *Nature*, vol. 484, no. 7392, pp. 62–68, 2012, 22419153[pmid] PMC3321074[pmcid] nature10918[PII]. [Online]. Available: https://pubmed.ncbi.nlm.nih.gov/22419153https://www.ncbi.nlm.nih.gov/pmc/articles/PMC3321074/

[80] R. N. Ramesh, C. R. Burgess, A. U. Sugden, M. Gyetvan, and M. L. Andermann, "Intermingled ensembles in visual association cortex encode stimulus identity or predicted outcome," *Neuron*, vol. 100, no. 4, pp. 900–915, 2018.

[81] A. Banerjee, G. Parente, J. Teutsch, C. Lewis, F. F. Voigt, and F. Helmchen, "Value-guided remapping of sensory cortex by lateral orbitofrontal cortex," *Nature*, vol. 585, no. 7824, pp. 245–250, 2020. [Online]. Available: https://doi.org/10.1038/s41586-020-2704-z

[82] R. Hattori and T. Komiyama, "Longitudinal two-photon calcium imaging with ultra-large cranial window for head-fixed mice," *STAR Protocols*, vol. 3, no. 2, p. 101343, 2022. [Online]. Available: https://www.sciencedirect.com/science/article/pii/S2666166722002234

[83] H. Lütcke, D. J. Margolis, and F. Helmchen, "Steady or changing? long-term monitoring of neuronal population activity," *Trends in Neurosciences*, vol. 36, no. 7, pp. 375–384, 2013. [Online]. Available: https://www.sciencedirect.com/science/article/pii/S0166223613000556

[84] L. N. Driscoll, N. L. Pettit, M. Minderer, S. N. Chettih, and C. D. Harvey, "Dynamic reorganization of neuronal activity patterns in parietal cortex," *Cell*, vol. 170, no. 5, pp. 986–999.e16, 2017. [Online]. Available: https://www.sciencedirect.com/science/article/pii/S0092867417308280

[85] R. Hattori, B. Danskin, Z. Babic, N. Mlynaryk, and T. Komiyama, "Area-specificity and plasticity of history-dependent value coding during learning," *Cell*, vol. 177, no. 7, pp. 1858–1872, 2019.

[86] A. Song, J. L. Gauthier, J. W. Pillow, D. W. Tank, and A. S. Charles, "Neural anatomy and optical microscopy (naomi) simulation for evaluating calcium imaging methods," *Journal of Neuroscience Methods*, vol. 358, p. 109173, 2021.

[87] A. Onken and S. Panzeri, "Mixed vine copulas as joint models of spike counts and local field potentials," *Advances in Neural Information Processing Systems 29 (Nips 2016)*, vol. 29, 2016, bm0pg Times Cited:0 Cited References Count:25 Advances in Neural Information Processing Systems. [Online]. Available: <GotoISI>://WOS:000458973700033

[88] H. Safaai, A. Onken, C. D. Harvey, and S. Panzeri, "Information estimation using nonparametric copulas," *Physical Review E*, vol. 98, no. 5, 2018, gz3oq Times Cited:9 Cited References Count:58. [Online]. Available: <GotoISI>://WOS:000449296300013

[89] T. J. Gawne and B. J. Richmond, "How independent are the messages carried by adjacent inferior temporal cortical neurons?" *Journal of Neuroscience*, vol. 13, no. 7, pp. 2758–2771, 1993.

[90] G. Rothschild, I. Nelken, and A. Mizrahi, "Functional organization and population dynamics in the mouse primary auditory cortex," *Nature neuroscience*, vol. 13, no. 3, pp. 353–360, 2010.

[91] E. Schneidman, W. Bialek, and M. J. Berry, "Synergy, redundancy, and independence in population codes," *Journal of Neuroscience*, vol. 23, no. 37, pp. 11 539–11 553, 2003.

[92] S. Nirenberg and P. E. Latham, "Decoding neuronal spike trains: How important are correlations?" *Proceedings of the National Academy of Sciences*, vol. 100, no. 12, pp. 7348–7353, 2003. [Online]. Available: https://www.pnas.org/doi/abs/10.1073/pnas.1131895100

[93] S. Nirenberg, S. M. Carcieri, A. L. Jacobs, and P. E. Latham, "Retinal ganglion cells act largely as independent encoders," *Nature*, vol. 411, no. 6838, pp. 698–701, 2001.

[94] R. S. Petersen, S. Panzeri, and M. E. Diamond, "Population coding of stimulus location in rat somatosensory cortex," *Neuron*, vol. 32, no. 3, pp. 503–514, 2001.

[95] H. D. Golledge, S. Panzeri, F. Zheng, G. Pola, J. W. Scannell, D. V. Giannikopoulos, R. J. Mason, M. J. Tovée, and M. P. Young, "Correlations, feature-binding and population coding in primary visual cortex," *Neuroreport*, vol. 14, no. 7, pp. 1045–1050, 2003.

[96] F. Montani, A. Kohn, M. A. Smith, and S. R. Schultz, "The role of correlations in direction and contrast coding in the primary visual cortex," *Journal of Neuroscience*, vol. 27, no. 9, pp. 2338–2348, 2007.

[97] N. Bertschinger, J. Rauh, E. Olbrich, J. Jost, and N. Ay, "Quantifying unique information," *Entropy*, vol. 16, no. 4, pp. 2161–2183, 2014.

[98] A. Makkeh, D. O. Theis, and R. Vicente, "Broja-2pid: A robust estimator for bivariate partial information decomposition," *Entropy*, vol. 20, no. 4, 2018, gj3hb Times Cited:4 Cited References Count:14. [Online]. Available: <GotoISI>://WOS:000435181600060

[99] S. Panzeri, C. D. Harvey, E. Piasini, P. E. Latham, and T. Fellin, "Cracking the neural code for sensory perception by combining statistics, intervention, and behavior," *Neuron*, vol. 93, no. 3, pp. 491–507, 2017.

[100] G. Pica, E. Piasini, H. Safaai, C. Runyan, C. Harvey, M. Diamond, C. Kayser, T. Fellin, and S. Panzeri, "Quantifying how much sensory information in a neural code is relevant for behavior," *Advances in Neural Information Processing Systems*, vol. 30, 2017.

[101] T. Schreiber, "Measuring information transfer," *Physical review letters*, vol. 85, no. 2, p. 461, 2000.

[102] J. Massey, "Causality, feedback and directed information," in *Proc. Int. Symp. Inf. Theory Applic.(ISITA-90)*, Conference Proceedings, pp. 303–305.

[103] R. Vicente, M. Wibral, M. Lindner, and G. Pipa, "Transfer entropy—a model-free measure of effective connectivity for the neurosciences," *Journal of computational neuroscience*, vol. 30, no. 1, pp. 45–67, 2011.

[104] B. L. Giordano, R. A. A. Ince, J. Gross, P. G. Schyns, S. Panzeri, and C. Kayser, "Contributions of local speech encoding and functional connectivity to audio-visual speech perception," *eLife*, vol. 6, p. e24763, 2017. [Online]. Available: https://doi.org/10.7554/eLife.24763

[105] M. Besserve, B. Schölkopf, N. K. Logothetis, and S. Panzeri, "Causal relationships between frequency bands of extracellular signals in visual cortex revealed by an information theoretic analysis," *Journal of computational neuroscience*, vol. 29, no. 3, pp. 547–566, 2010.

[106] S. Ito, M. E. Hansen, R. Heiland, A. Lumsdaine, A. M. Litke, and J. M. Beggs, "Extending transfer entropy improves identification of effective connectivity in a spiking cortical network model," *PLOS ONE*, vol. 6, no. 11, p. e27431, 2011. [Online]. Available: https://doi.org/10.1371/journal.pone.0027431

[107] J. Bím, V. De Feo, D. Chicharro, I. Hanganu-Opatz, A. Brovelli, and S. Panzeri, "A non-negative measure of feature-specific information transfer between neural signals," 2019.

[108] R. D. Beer and P. L. Williams, "Information processing and dynamics in minimally cognitive agents," *Cognitive Science*, vol. 39, no. 1, pp. 1–38, 2015. [Online]. Available: https://onlinelibrary.wiley.com/doi/abs/10.1111/cogs.12142

[109] A. Treves and S. Panzeri, "The upward bias in measures of information derived from limited data samples," *Neural Computation*, vol. 7, no. 2, pp. 399–407, 1995.

[110] A. M. Ramos and E. E. Macau, "Minimum sample size for reliable causal inference using transfer entropy," *Entropy*, vol. 19, no. 4, p. 150, 2017.

[111] S. P. Strong, R. Koberle, R. R. D. R. Van Steveninck, and W. Bialek, "Entropy and information in neural spike trains," *Physical review letters*, vol. 80, no. 1, p. 197, 1998.

[112] L. Paninski, "Estimation of entropy and mutual information," *Neural computation*, vol. 15, no. 6, pp. 1191–1253, 2003.

[113] M. J. Tovee, E. T. Rolls, A. Treves, and R. P. Bellis, "Information encoding and the responses of single neurons in the primate temporal visual cortex," *Journal of Neurophysiology*, vol. 70, no. 2, pp. 640–654, 1993.

[114] T. M. Cover, *Elements of information theory*. John Wiley Sons, 1999.

[115] J. Friedman, T. Hastie, and R. Tibshirani, "Regularization paths for generalized linear models via coordinate descent," *Journal of Statistical Software*, vol. 33, no. 1, pp. 1–22, 2010, 564hf Times Cited:6844 Cited References Count:49. [Online]. Available: <GotoISI>://WOS:000275203200001

[116] J. W. Pillow, J. Shlens, L. Paninski, A. Sher, A. M. Litke, E. Chichilnisky, and E. P. Simoncelli, "Spatio-temporal correlations and visual signalling in a complete neuronal population," *Nature*, vol. 454, no. 7207, pp. 995–999, 2008.

[117] V. Lawhern, W. Wu, N. Hatsopoulos, and L. Paninski, "Population decoding of motor cortical activity using a generalized linear model with hidden states," *Journal of neuroscience methods*, vol. 189, no. 2, pp. 267–280, 2010.

[118] M. Valente, G. Pica, G. Bondanelli, M. Moroni, C. A. Runyan, A. S. Morcos, C. D. Harvey, and S. Panzeri, "Correlations enhance the behavioral readout of neural population activity in association cortex," *Nature neuroscience*, vol. 24, no. 7, pp. 975–986, 2021.

[119] D. Raposo, M. T. Kaufman, and A. K. Churchland, "A category-free neural population supports evolving demands during decision-making," *Nature Neuroscience*, vol. 17, no. 12, pp. 1784–1792, 2014. [Online]. Available: https://doi.org/10.1038/nn.3865

[120] R. Bartolo, R. C. Saunders, A. R. Mitz, and B. B. Averbeck, "Information-limiting correlations in large neural populations," *The Journal of Neuroscience*, vol. 40, no. 8, pp. 1668–1678, 2020. [Online]. Available: https://www.jneurosci.org/content/jneuro/40/8/1668.full.pdf

[121] C.-C. Chang, "" libsvm: a library for support vector machines," acm transactions on intelligent systems and technology, 2: 27: 1–27: 27, 2011," *http://www. csie. ntu. edu. tw/ cjlin/libsvm*, vol. 2, 2011.

[122] A. Onken, J. K. Liu, P. C. R. Karunasekara, I. Delis, T. Gollisch, and S. Panzeri, "Using matrix and tensor factorizations for the single-trial analysis of population spike trains," *PLoS computational biology*, vol. 12, no. 11, p. e1005189, 2016.

[123] M. Pachitariu, D. R. Lyamzin, M. Sahani, and N. A. Lesica, "State-dependent population coding in primary auditory cortex," *Journal of Neuroscience*, vol. 35, no. 5, pp. 2058–2073, 2015.

[124] N. Montgomery and M. Wehr, "Auditory cortical neurons convey maximal stimulus-specific information at their best frequency," *Journal of Neuroscience*, vol. 30, no. 40, pp. 13 362–13 366, 2010.

[125] R. A. A. Ince, A. Mazzoni, A. Bartels, N. K. Logothetis, and S. Panzeri, "A novel test to determine the significance of neural selectivity to single and multiple potentially correlated stimulus features," *Journal of Neuroscience Methods*, vol. 210, no. 1, pp. 49–65, 2012. [Online]. Available: https://www.sciencedirect.com/science/article/pii/S0165027011006893

[126] A. M. Winkler, M. A. Webster, D. Vidaurre, T. E. Nichols, and S. M. Smith, "Multi-level block permutation," *NeuroImage*, vol. 123, pp. 253–268, 2015. [Online]. Available: https://www.sciencedirect.com/science/article/pii/S105381191500508X

[127] J. Gross, N. Hoogenboom, G. Thut, P. Schyns, S. Panzeri, P. Belin, and S. Garrod, "Speech rhythms and multiplexed oscillatory sensory coding in the human brain," *PLOS Biology*, vol. 11, no. 12, p. e1001752, 2014. [Online]. Available: https://doi.org/10.1371/journal.pbio.1001752

[128] P. G. Schyns, G. Thut, and J. Gross, "Cracking the code of oscillatory activity," *PLOS Biology*, vol. 9, no. 5, p. e1001064, 2011. [Online]. Available: https://doi.org/10.1371/journal.pbio.1001064

[129] K. M. M. Walker, J. K. Bizley, A. J. King, and J. W. H. Schnupp, "Multiplexed and robust representations of sound features in auditory cortex," *The Journal of Neuroscience*, vol. 31, no. 41, pp. 14 565–14 576, 2011. [Online]. Available: https://www.jneurosci.org/content/jneuro/31/41/14565.full.pdf

[130] V. Esmaeili and M. E. Diamond, "Neuronal correlates of tactile working memory in prefrontal and vibrissal somatosensory cortex," *Cell Reports*, vol. 27, no. 11, pp. 3167–3181.e5, 2019. [Online]. Available: https://www.sciencedirect.com/science/article/pii/S2211124719306540

[131] J. Tubiana, S. Wolf, T. Panier, and G. Debregeas, "Blind deconvolution for spike inference from fluorescence recordings," *Journal of neuroscience methods*, vol. 342, p. 108763, 2020.

[132] M. Pachitariu, C. Stringer, and K. D. Harris, "Robustness of spike deconvolution for neuronal calcium imaging," *Journal of Neuroscience*, vol. 38, no. 37, pp. 7976–7985, 2018.

[133] M. A. Triplett, Z. Pujic, B. Sun, L. Avitan, and G. J. Goodhill, "Model-based decoupling of evoked and spontaneous neural activity in calcium imaging data," *PLoS computational biology*, vol. 16, no. 11, p. e1008330, 2020.

[134] P. Ledochowitsch, L. Huang, U. Knoblich, M. Oliver, J. Lecoq, C. Reid, L. Li, H. Zeng, C. Koch, J. Waters, S. E. de Vries, and M. A. Buice, "On the correspondence of electrical and optical physiology in in vivo population-scale two-photon calcium imaging," *bioRxiv*, p. 800102, 2019. [Online]. Available: https://www.biorxiv.org/content/biorxiv/early/2019/10/11/800102.full.pdf

[135] F. Helmchen and D. W. Tank, "A single-compartment model of calcium dynamics in nerve terminals and dendrites," *Cold Spring Harbor Protocols*, vol. 2015, no. 2, p. pdb. top085910, 2015.

[136] J. Akerboom, T.-W. Chen, T. J. Wardill, L. Tian, J. S. Marvin, S. Mutlu, N. C. Calderón, F. Esposti, B. G. Borghuis, and X. R. Sun, "Optimization of a gcamp calcium indicator for neural activity imaging," *Journal of neuroscience*, vol. 32, no. 40, pp. 13 819–13 840, 2012.

[137] T.-W. Chen, T. J. Wardill, Y. Sun, S. R. Pulver, S. L. Renninger, A. Baohan, E. R. Schreiter, R. A. Kerr, M. B. Orger, and V. Jayaraman, "Ultrasensitive fluorescent proteins for imaging neuronal activity," *Nature*, vol. 499, no. 7458, pp. 295–300, 2013.

[138] C. Grienberger and A. Konnerth, "Imaging calcium in neurons," *Neuron*, vol. 73, no. 5, pp. 862–885, 2012.

[139] S. Peron, T.-W. Chen, and K. Svoboda, "Comprehensive imaging of cortical networks," *Current opinion in neurobiology*, vol. 32, pp. 115–123, 2015.

[140] F. Ali and A. C. Kwan, "Interpreting in vivo calcium signals from neuronal cell bodies, axons, and dendrites: a review," *Neurophotonics*, vol. 7, no. 1, p. 011402, 2019.

[141] M. Brondi, M. Moroni, D. Vecchia, M. Molano-Mazón, S. Panzeri, and T. Fellin, "High-accuracy detection of neuronal ensemble activity in two-photon functional microscopy using smart line scanning," *Cell reports*, vol. 30, no. 8, pp. 2567–2580. e6, 2020.

[142] L. Theis, P. Berens, E. Froudarakis, J. Reimer, M. R. Rosón, T. Baden, T. Euler, A. S. Tolias, and M. Bethge, "Benchmarking spike rate inference in population calcium imaging," *Neuron*, vol. 90, no. 3, pp. 471–482, 2016.

[143] L. Huang, P. Ledochowitsch, U. Knoblich, J. Lecoq, G. J. Murphy, R. C. Reid, S. E. de Vries, C. Koch, H. Zeng, M. A. Buice *et al.*, "Relationship between simultaneously recorded spiking activity and fluorescence signal in gcamp6 transgenic mice," *Elife*, vol. 10, p. e51675, 2021.

[144] M. Panniello, A. J. King, J. C. Dahmen, and K. M. M. Walker, "Local and global spatial organization of interaural level difference and frequency preferences in auditory cortex," *Cerebral Cortex*, vol. 28, no. 1, pp. 350–369, 2017. [Online]. Available: https://doi.org/10.1093/cercor/bhx295

[145] X. Shi, J. Barchini, H. A. Ledesma, D. Koren, Y. Jin, X. Liu, W. Wei, and J. Cang, "Retinal origin of direction selectivity in the superior colliculus," *Nature neuroscience*, vol. 20, no. 4, pp. 550–558, 2017.

[146] J. Larsch, D. Ventimiglia, C. I. Bargmann, and D. R. Albrecht, "High-throughput imaging of neuronal activity in caenorhabditis elegans," *Proceedings of the National Academy of Sciences*, vol. 110, no. 45, pp. E4266–E4273, 2013. [Online]. Available: https://www.pnas.org/doi/abs/10.1073/pnas.1318325110

[147] T. Dalmay, E. Abs, R. B. Poorthuis, J. Hartung, D.-L. Pu, S. Onasch, Y. R. Lozano, J. Signoret-Genest, P. Tovote, J. Gjorgjieva, and J. J. Letzkus, "A critical role for neocortical processing of threat memory," *Neuron*, vol. 104, no. 6, pp. 1180–1194.e7, 2019. [Online]. Available: https://www.sciencedirect.com/science/article/pii/S0896627319307998

[148] M. B. Pardi, J. Vogenstahl, T. Dalmay, T. Spanò, D.-L. Pu, L. B. Naumann, F. Kretschmer, H. Sprekeler, and J. J. Letzkus, "A thalamocortical top-down circuit for associative memory," *Science*, vol. 370, no. 6518, pp. 844–848, 2020. [Online]. Available: https://www.science.org/doi/abs/10.1126/science.abc2399

[149] N. Doostdar, J. Airey, C. I. Radulescu, L. Melgosa-Ecenarro, N. Zabouri, P. Pavlidi, M. Kopanitsa, T. Saito, T. Saido, and S. J. Barnes, "Multi-scale network imaging in a mouse model of amyloidosis," *Cell Calcium*, vol. 95, p. 102365, 2021. [Online]. Available: https://www.sciencedirect.com/science/article/pii/S0143416021000191

[150] B. Bathellier, L. Ushakova, and S. Rumpel, "Discrete neocortical dynamics predict behavioral categorization of sounds," *Neuron*, vol. 76, no. 2, pp. 435–449, 2012. [Online]. Available: https://www.sciencedirect.com/science/article/pii/S0896627312006575

[151] J. Friedrich, P. Zhou, and L. Paninski, "Fast online deconvolution of calcium imaging data," *PLoS computational biology*, vol. 13, no. 3, p. e1005423, 2017.

[152] A. Giovannucci, J. Friedrich, P. Gunn, J. Kalfon, B. L. Brown, S. A. Koay, J. Taxidis, F. Najafi, J. L. Gauthier, and P. Zhou, "Caiman an open source tool for scalable calcium imaging data analysis," *Elife*, vol. 8, p. e38173, 2019.

[153] T. Deneux, A. Kaszas, G. Szalay, G. Katona, T. Lakner, A. Grinvald, B. Rózsa, and I. Vanzetta, "Accurate spike estimation from noisy calcium signals for ultrafast three-dimensional imaging of large neuronal populations in vivo," *Nature communications*, vol. 7, no. 1, pp. 1–17, 2016.

[154] P. Berens, J. Freeman, T. Deneux, N. Chenkov, T. McColgan, A. Speiser, J. H. Macke, S. C. Turaga, P. Mineault, P. Rupprecht, S. Gerhard, R. W. Friedrich, J. Friedrich, L. Paninski, M. Pachitariu, K. D. Harris, B. Bolte, T. A. Machado, D. Ringach, J. Stone, L. E. Rogerson, N. J. Sofroniew, J. Reimer, E. Froudarakis, T. Euler, M. Román Rosón, L. Theis, A. S. Tolias, and M. Bethge, "Community-based benchmarking improves spike rate inference from two-photon calcium imaging data," *PLOS Computational Biology*, vol. 14, no. 5, p. e1006157, 2018. [Online]. Available: https://doi.org/10.1371/journal.pcbi.1006157

[155] Z. Wei, B.-J. Lin, T.-W. Chen, K. Daie, K. Svoboda, and S. Druckmann, "A comparison of neuronal population dynamics measured with calcium imaging and electrophysiology," *PLoS computational biology*, vol. 16, no. 9, p. e1008198, 2020.

[156] S. Bovetti, C. Moretti, S. Zucca, M. Dal Maschio, P. Bonifazi, and T. Fellin, "Simultaneous high-speed imaging and optogenetic inhibition in the intact mouse brain," *Scientific reports*, vol. 7, no. 1, p. 40041, 2017.

[157] S. Zucca, G. D'Urso, V. Pasquale, D. Vecchia, G. Pica, S. Bovetti, C. Moretti, S. Varani, M. Molano-Mazón, and M. Chiappalone, "An inhibitory gate for state transition in cortex," *Elife*, vol. 6, p. e26177, 2017.

[158] Y. Zuo, H. Safaai, G. Notaro, A. Mazzoni, S. Panzeri, and M. E. Diamond, "Complementary contributions of spike timing and spike rate to perceptual decisions in rat s1 and s2 cortex," *Current Biology*, vol. 25, no. 3, pp. 357–363, 2015.

[159] T.-W. Chen, N. Li, K. Daie, and K. Svoboda, "A map of anticipatory activity in mouse motor cortex," *Neuron*, vol. 94, no. 4, pp. 866–879. e4, 2017.

[160] S. P. Sherrill, N. M. Timme, J. M. Beggs, and E. L. Newman, "Partial information decomposition reveals that synergistic neural integration is greater downstream of recurrent information flow in organotypic cortical cultures," *PLoS computational biology*, vol. 17, no. 7, p. e1009196, 2021.

[161] A. H. Williams, T. H. Kim, F. Wang, S. Vyas, S. I. Ryu, K. V. Shenoy, M. Schnitzer, T. G. Kolda, and S. Ganguli, "Unsupervised discovery of demixed, low-dimensional neural dynamics across multiple timescales through tensor component analysis," *Neuron*, vol. 98, no. 6, pp. 1099–1115, 2018.

[162] Z. F. Mainen, M. Häusser, and A. Pouget, "A better way to crack the brain," *Nature*, vol. 539, no. 7628, pp. 159–161, 2016.

[163] R. D. Peng, "Reproducible research in computational science," *Science*, vol. 334, no. 6060, pp. 1226–1227, 2011.

[164] M. Topalidou, A. Leblois, T. Boraud, and N. P. Rougier, "A long journey into reproducible computational neuroscience," *Frontiers in computational neuroscience*, vol. 9, p. 30, 2015.

[165] G. Foffani, B. Tutunculer, and K. A. Moxon, "Role of spike timing in the forelimb somatosensory cortex of the rat," *Journal of Neuroscience*, vol. 24, no. 33, pp. 7266–7271, 2004.

[166] M. Lindner, R. Vicente, V. Priesemann, and M. Wibral, "Trentool: A matlab open source toolbox to analyse information flow in time series data with transfer entropy," *BMC Neuroscience*, vol. 12, no. 1, p. 119, 2011. [Online]. Available: https://doi.org/10.1186/1471-2202-12-119

[167] E. Schneidman, M. J. Berry, R. Segev, and W. Bialek, "Weak pairwise correlations imply strongly correlated network states in a neural population," *Nature*, vol. 440, no. 7087, pp. 1007–1012, 2006.

[168] R. Ince, R. Petersen, D. Swan, and S. Panzeri, "Python for information theoretic analysis of neural data," *Frontiers in Neuroinformatics*, vol. 3, 2009. [Online]. Available: https://www.frontiersin.org/articles/10.3389/neuro.11.004.2009

[169] M. Wibral, V. Priesemann, J. W. Kay, J. T. Lizier, and W. A. Phillips, "Partial information decomposition as a unified approach to the specification of neural goal functions," *Brain and cognition*, vol. 112, pp. 25–38, 2017.

[170] D. G. Moore, G. Valentini, S. I. Walker, and M. Levin, "Inform: A toolkit for information-theoretic analysis of complex systems," in *2017 IEEE Symposium Series on Computational Intelligence (SSCI)*, Conference Proceedings, pp. 1–8.

[171] A. Montalto, L. Faes, and D. Marinazzo, "Mute: A matlab toolbox to compare established and novel estimators of the multivariate transfer entropy," *PLOS ONE*, vol. 9, no. 10, p. e109462, 2014. [Online]. Available: https://doi.org/10.1371/journal.pone.0109462

[172] V. P. Pastore, D. Poli, A. Godjoski, S. Martinoia, and P. Massobrio, "Toolconnect: A functional connectivity toolbox for in vitro networks," *Frontiers in Neuroinformatics*, vol. 10, 2016. [Online]. Available: https://www.frontiersin.org/articles/10.3389/fninf.2016.00013

[173] D. H. Goldberg, J. D. Victor, E. P. Gardner, and D. Gardner, "Spike train analysis toolkit: Enabling wider application of information-theoretic techniques to neurophysiology," *Neuroinformatics*, vol. 7, no. 3, pp. 165–178, 2009. [Online]. Available: https://doi.org/10.1007/s12021-009-9049-y

[174] Z. Szabó, "Information theoretical estimators toolbox," *The Journal of Machine Learning Research*, vol. 15, no. 1, pp. 283–287, 2014.

[175] Dit-Contributors, "Dit: Discrete information theory," 2018. [Online]. Available: https://dit.readthedocs.io/en/latest/

[176] V. Rahmati, K. Kirmse, D. Marković, K. Holthoff, and S. J. Kiebel, "Inferring neuronal dynamics from calcium imaging data using biophysical models and bayesian inference," *PLoS computational biology*, vol. 12, no. 2, p. e1004736, 2016.

[177] S. Panzeri and S. R. Schultz, "A unified approach to the study of temporal, correlational, and rate coding," *Neural Computation*, vol. 13, no. 6, pp. 1311–1349, 2001.

[178] R. Brette and A. Destexhe, *Handbook of neural activity measurement*. Cambridge University Press, 2012.

[179] K. I. van Aerde and D. Feldmeyer, "Morphological and physiological characterization of pyramidal neuron subtypes in rat medial prefrontal cortex," *Cerebral Cortex*, vol. 25, no. 3, pp. 788–805, 2013. [Online]. Available: https://doi.org/10.1093/cercor/bht278

[180] F. Sala and A. Hernández-Cruz, "Calcium diffusion modeling in a spherical neuron. relevance of buffering properties," *Biophysical Journal*, vol. 57, no. 2, pp. 313–324, 1990. [Online]. Available: https://www.sciencedirect.com/science/article/pii/S0006349590825339

[181] F. Helmchen, K. Imoto, and B. Sakmann, "Ca2+ buffering and action potential-evoked ca2+ signaling in dendrites of pyramidal neurons," *Biophysical journal*, vol. 70, no. 2, pp. 1069–1081, 1996.

[182] H. Svoboda, "Simultaneous imaging and loose-seal cell-attached electrical recordings from neurons expressing a variety of genetically encoded calcium indicators," *GENIE project, Janelia Farm Campus, CRCNS. org*, 2015.

# Population coding strategies in human tactile afferents

G. Corniani, **M. A. Casal**, S. Panzeri and H. P. Saal, "Population coding strategies in human tactile afferents," *PLOS Computational Biology*, vol. 18, no. 12, pp. e1010763, 2022.

DOI: https://doi.org/10.1371/journal.pcbi.1010763

Keywords: *tactile coding* | *population coding* | *mechanoreceptors* | *mutual information*

## Candidate's contribution to the paper

**Conceptualization:** Giulia Corniani, **Miguel A. Casal**, Stefano Panzeri, Hannes P. Saal.

**Formal analysis:** Giulia Corniani, **Miguel A. Casal**.

**Funding acquisition:** Stefano Panzeri, Hannes P. Saal.

**Methodology:** Giulia Corniani, **Miguel A. Casal**.

**Software:** Giulia Corniani, **Miguel A. Casal**.

**Supervision:** Stefano Panzeri, Hannes P. Saal.

**Visualization:** Giulia Corniani, **Miguel A. Casal**.

**Writing – original draft:** Giulia Corniani, **Miguel A. Casal**.

**Writing – review & editing:** Giulia Corniani, **Miguel A. Casal**, Stefano Panzeri, Hannes P. Saal.

## Abstract

Sensory information is conveyed by populations of neurons, and coding strategies cannot always be deduced when considering individual neurons. Moreover, information coding depends on the number of neurons available and on the composition of the population when multiple classes with different response properties are available. Here, we study population coding in human tactile afferents by employing a recently developed simulator of mechanoreceptor firing activity. First, we highlight the interplay of afferents within each class. We demonstrate that the optimal afferent density to convey maximal information depends on both the tactile feature under consideration and the afferent class. Second, we find that information is spread across different classes for all tactile features and that each class encodes both redundant and complementary information with respect to the other afferent classes. Specifically, combining information from multiple afferent classes improves information transmission and is often more efficient than increasing the density of afferents from the same class. Finally, we examine the importance of temporal and spatial contributions, respectively, to the joint spatiotemporal code. On average, destroying temporal information is more destructive than removing spatial information, but the importance of either depends on the stimulus feature analysed. Overall, our results suggest that both optimal afferent innervation densities and the composition of the population depend in complex ways on the tactile features in question, potentially accounting for the variety in which tactile peripheral populations are assembled in different regions across the body.



## Author summary

Touching an object elicits neural responses from hundreds or thousands of individual tactile receptors of different classes embedded within our hand. Information about the extent of contact, the strength of the touch, and its temporal profile are carried jointly in this population response to be processed further by the central nervous system. However, studying the nature of the population code is empirically challenging, as electrophysiological recordings are typically obtained from single or a small number of neurons at most. Here, we make use of a computer simulation to recreate the population activity of large numbers of tactile neurons and examine how information is spread across different neurons. We find that tactile information increases

with afferent density, but the saturation point depends on both the tactile feature and afferent class. Importantly, information is generally spread across multiple afferent classes, such that a combination of afferents from multiple classes yields higher information than the same number of neurons from a single class. These results will be useful to guide future experiments and theoretical work on the processing of tactile information by the central nervous system.

# 1 Introduction

The brain processes information and makes decisions based on the activity of populations of neurons [183]. Studying population activity can reveal aspects of the neural code that are obscured when only individual neurons are considered [184]. For example, the well-known population vector technique has shown that the direction of arm movements can be precisely decoded from a population of cortical motor neurons, even though individual neurons are only broadly tuned to direction [185]. Moreover, some coding strategies will become evident only if the responses of multiple neurons are considered. For example, while a neuron that remains silent to a certain stimulus might not appear to convey any information at all, when it is part of a larger population where other neurons are responding, this silence can be meaningful [186]. Response correlations between neurons also affect decoding (see [187] for an example). Furthermore, populations often consist of heterogeneous classes of neurons, especially in sensory systems, such as the diversity of retinal ganglion cells in the visual pathway [188] or the different classes of tactile neurons in the somatosensory periphery [189]. Theoretical studies have shown how response properties and class membership of individual neurons can be optimized to maximize joint information coding in the population [190–192]. However, because this optimization relies on the full population, predicting how or to what extent an individual neuron contributes to population coding becomes impossible without considering the properties of other neurons that make up the population. Given these findings, it is thus paramount to study the population activity of sensory neurons in order to understand what stimulus information is available at subsequent processing stages.

Tactile interactions are mediated by mechanoreceptive afferents and the glabrous skin of the human hand is innervated by approximately 17,000 fibers [193]. These are divided into different classes based on their response properties and receptive fields. Three classes are mainly involved in discriminative touch: slowly adapting type 1 afferents (SA1) exhibit small receptive fields and respond to static or low-frequency indentations, rapidly adapting afferents (RA) possess slightly larger receptive fields and respond to dynamic flutter stimuli, and Pacinian afferents (PC) exhibit extremely large receptive fields and are most responsive to high frequency vibrations. These classes also differ in the density with which they innervate the skin, both compared to each other

and at different locations on the skin [193]. A stimulus applied to a specific skin area will typically activate hundreds if not thousands of afferents of different classes all responding with distinct spiking responses [194]. However, peripheral neurophysiological measurements are subject to technical limitations, and typically only one or a small number of afferents are recorded at once. Moreover, many studies place the stimulus directly above the targeted afferent's receptive field hotspot, in an effort to maximize neural responses within the limited recording window, but such a setup implies that responses from receptors located away from the contact location will be neglected. Given these constraints, afferent activity on a population level has scarcely been investigated, and, consequently, our understanding of how tactile information is represented in the peripheral population is limited (though see [195] for a summary of tactile population codes).

A particular source of debate in the tactile literature has been the role of different afferent classes. Traditionally, each afferent class was thought to carry information about different and complementary stimulus features [196]. However, more recently, it has become clear that most natural stimuli elicit responses from multiple afferent classes simultaneously (see summary in [197]), for example, in texture perception [198]. Furthermore, both experimental evidence [199] and computational modeling [200] suggest that information from multiple classes of afferents is integrated in cortex, if not before, and psychophysical studies have revealed that the quality of a tactile percept does not necessarily depend on receptor class [201]. However, to what extent peripheral tactile population activity carries complementary information about relevant stimulus features in different afferent classes has not been quantified and it is therefore unclear when and how it would be beneficial to integrate such information.

Here, we investigate the contribution of large neural populations in tactile stimulus coding and examine the interplay of tactile submodalities in this process. Because the lack of population level data currently precludes empirical study, we used a large-scale computational model, Touchsim [202], to simulate the activity of hundreds of peripheral tactile afferents of three classes in response to naturalistic stimuli, similar to those commonly used in experimental settings. First, we parametrically studied the role of afferent density in single-class afferent populations to explore if and how the composition, and particularly the number of afferents, affects the stimulus information encoding. Secondly, we considered the three classes together and asked whether

each class encoded complementary or redundant information regarding stimulus features. Finally, we assessed the importance of temporal and spatial encoding precision when considering afferents on a population level. Overall, our work demonstrates that a population-level view of tactile coding is crucial for a thorough understanding of tactile information processing.

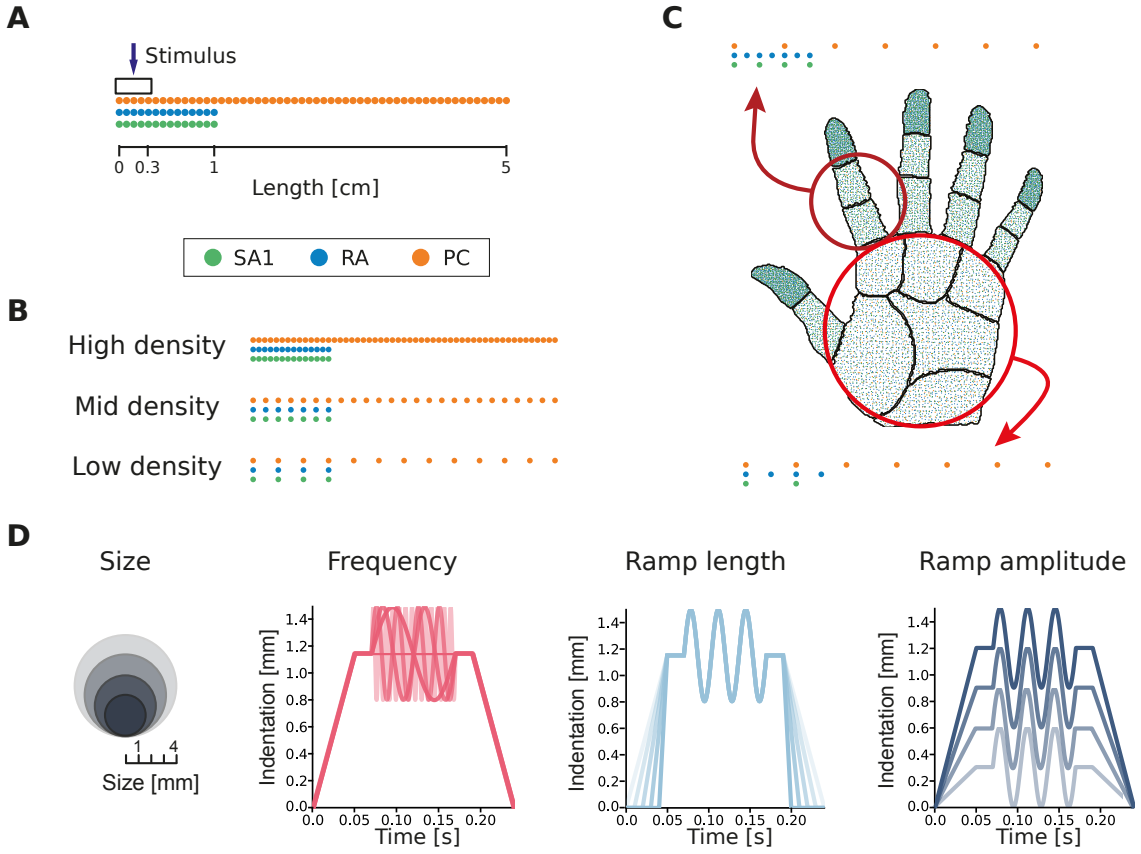


**Fig. 15: Simulation setup.** **(A)** Example of afferents terminating along a line, radiating outwards from the probe centre (indicated by the arrow). The probe has circular shape (of varying size) and is centred on the origin of the line. Dots of different colors correspond to different afferent classes (separated in the illustration to facilitate visualization). **(B)** Example of afferent populations with different densities. **(C)** Representation of afferent densities measured on the human hand and corresponding simulated populations distributed over a line that mimic the densities observed in the palm and finger. **(D)** Illustration of the different stimulus features considered: probe size, vibration frequency, ramp length, and ramp amplitude.

## 2 Results

We used a large-scale neural simulator [202] to simulate the spiking activity of individual afferents belonging to three afferent classes (SA1, RA, PC) jointly spanning the range of tactile sensitivity. In our setup, we simulated the responses of a population of receptors placed along a

line extending outwards from the contact location of the stimulus probe (see Fig 15A). This spatial arrangement of receptors allowed for systematic manipulation of the receptor density in the simulations. Sixteen different afferent populations with a density ranging between 1 and 140 afferents/cm$^2$ were considered for each afferent class. Therefore, we could test the effect of low, medium, and high densities (Fig 15B) on information encoding and also directly examine natural innervation densities, such as those encountered on the palm or finger (Fig 15C). The simulated stimulus was a circular probe indented into the skin and then vibrated. We varied four stimulus features systematically across trials: the probe size (1-4 mm), the ramp amplitude (0.3-1.2 mm), the ramp length (10-50 ms), and the vibration frequency (0-200 Hz) (see Fig 15D and Methods). These parameters were chosen to span the range of tactile stimuli that are typically experienced. They are also similar to stimuli commonly employed in neurophysiological experiments, such as those used to fit the initial Touchsim model [202], and simulated responses can therefore be expected to be a close match to what would be recorded in an actual experiment. Finally, varying the stimulus across multiple parameters simultaneously ensures that the complexity of everyday tactile interactions is reproduced in the resulting population responses.

To analyse the simulated responses, we coupled advanced machine learning techniques with information-theoretic analysis to compute how much information about each stimulus feature was encoded in the activity of different populations of afferents (see Methods). In brief, after simulating the spiking responses (Figure 16A), we first used Non-Negative Matrix Factorization (NMF) [203] to succinctly capture the spatiotemporal patterns of neural responses for each afferent class (Fig 16B). This technique linearly decomposes each single-trial spatiotemporal sequence of spike trains into a sum of non-negative spatiotemporal modules (describing commonly occurring population activity patterns across neurons and time) and non-negative activation coefficients (describing how strongly each pattern is recruited in a given trial). For this first stage, we chose an unsupervised technique that did not take into account the specific stimulus features used to generate the responses in each trial, because this provides an effective and relatively hypothesis-free way to describe neural responses to all possible stimuli. The specific choice of NMF was made because this technique provides a natural decomposition for spike trains, which are by nature non-negative, because it can give accurate single-trial representations of activity even when neural responses are non-orthogonal and overlapping from

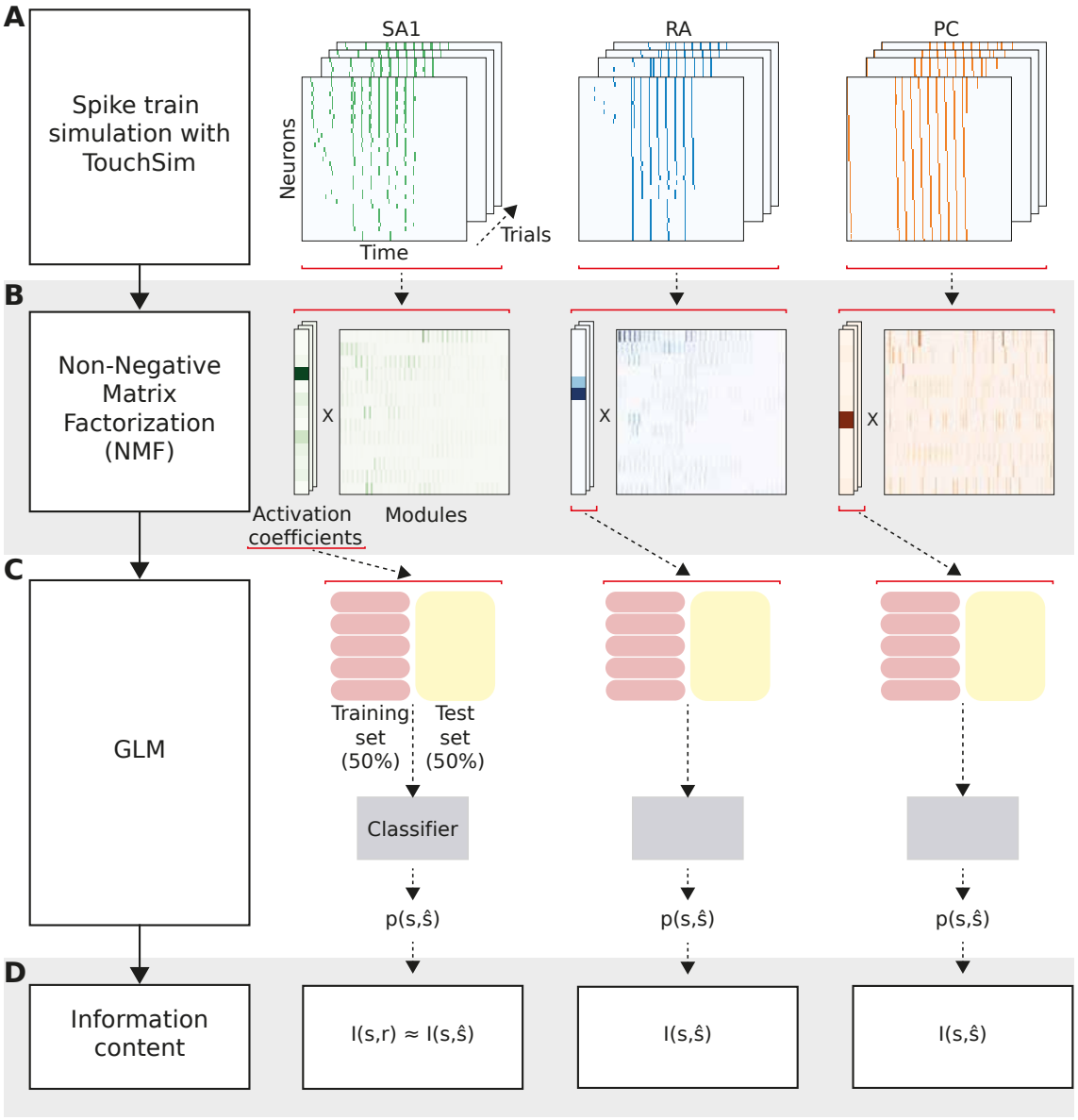


**Fig. 16: Analysis pipeline and calculation of information**. **(A)** Spike trains are generated using the Touchsim simulator. **(B)** The spike matrices are then decomposed using the Non-Negative Matrix Factorization (NMF) method, obtaining a set of non-negative activation coefficients and modules. **(C)** A Generalized Linear Model (GLM) fed with the neural activity captured in the NMF activation coefficients gives the probability of observing each stimulus feature. **(D)** Probabilities are used to compute mutual information (MI), representing the information that the neural activity carries about the stimulus.

trial to trial, and because both its basis functions and coefficients are biologically interpretable in terms of commonly occurring activity patterns and their activation strength in each trial, respectively [204, 205]. We decided on using spatiotemporal decompositions for this stage, as used in previous studies [206–208], rather than e.g. decompositions along only the spatial or

temporal dimension, or tensor decompositions that assume separability in space or time [204, 205], in order to avoid introducing strong hypotheses about the spatiotemporal nature of neural population responses, which may be difficult to test or which may bias comparisons across afferent classes that may have different degrees of interdependence between spatial and temporal structure.

In the second stage, we extracted specific features from the NMF representation using a supervised technique. Following previous work [209], we approximated the probabilities of occurrence of the NMF activation coefficients using a Generalized Linear Model (GLM; see Fig 16C). We then used this probabilistic model to compute the posterior probability of each stimulus feature given the observation of the spatiotemporal population spike train in each trial. Finally, we computed the information using the posterior probabilities between the presented and the decoded stimulus (Fig 16D). This procedure provides a data-robust but effective lower bound to the total information carried by population activity [184]. We also checked the robustness of our main findings using a control analysis employing a simpler decomposition model (see Methods and 22), where the NMF decomposition is only applied along the spatial axis [210], yielding a larger number of coefficients for the classifier. This analysis shifts part of the analysis from unsupervised to supervised and can therefore be expected to extract more information overall, but it makes strong assumptions about the separability of the spatial dimensions (as it decomposes only simultaneous responses across neurons), which may not be suitable for some afferent classes for which spatial and temporal response profiles may be non-separable (see below for some examples).

## 2.1 Information carried by individual afferent populations

In a first analysis, we investigated the information carried by each of the three afferent populations separately. To understand which afferent population best encoded any given feature, and how the information depended on the spatial density of the afferents, we calculated the total information carried by each population (Fig 17A) by simulating responses with different spatial receptor densities.

For encoding stimulus size, we found that SA1 afferents were most informative, with information increasing and then saturating at a density of 40 afferents/cm$^2$. RA afferents provided more

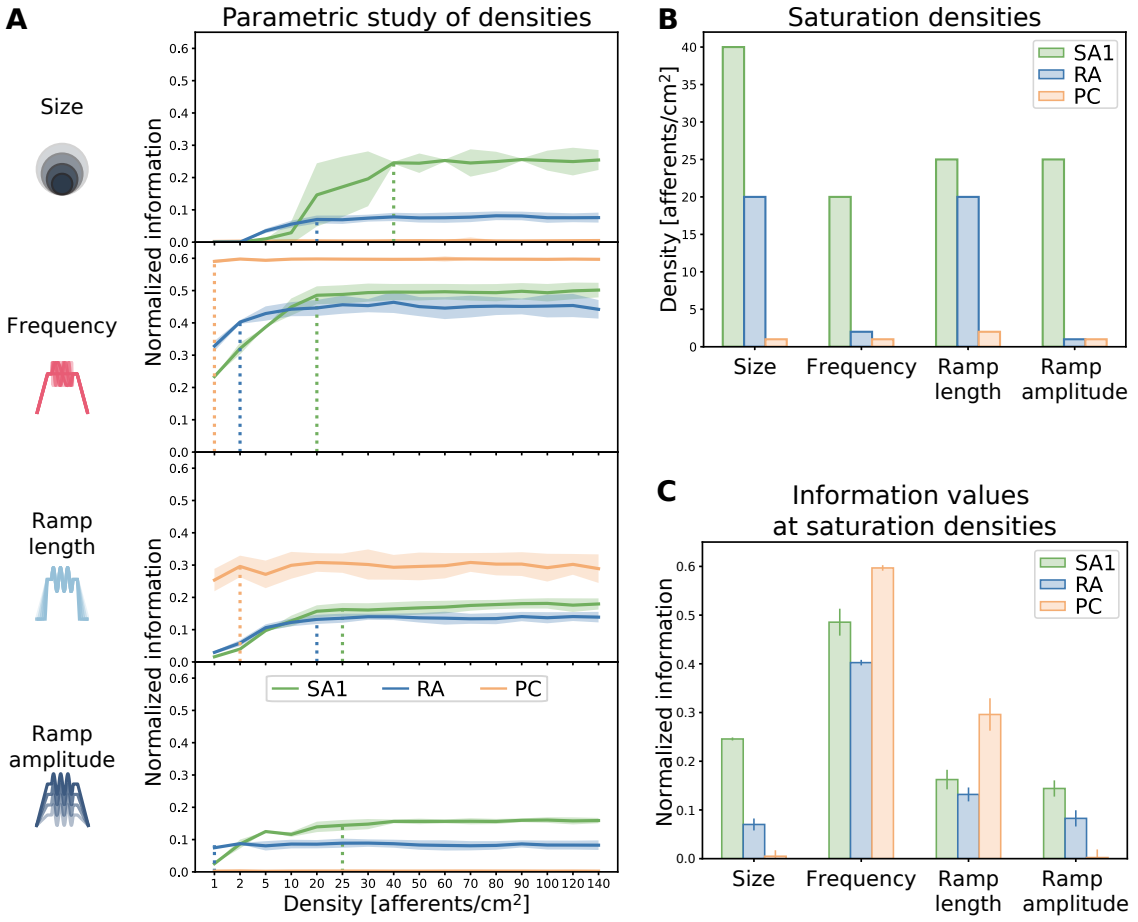


**Fig. 17: Effect of afferent density on stimulus feature coding.** **(A)** Information content (normalized by the stimulus entropy) for different stimulus features provided by single-class afferent populations of varying density. Solid lines represent the average over 40 trials, shaded regions represent standard deviation across NMF instantiations. Dotted vertical lines indicate information saturation points. **(B)** Saturation densities for each feature and afferent class. **(C)** Maximum information content provided by each afferent class at the saturation density for each feature. Error bars represent standard deviation across NMF instantiations.

information at very low densities and saturated at a lower level (20 afferents/cm$^2$). In contrast, PC afferents did not carry any information about stimulus size at any of the densities considered. This result can be explained by the fact that PC afferents exhibit extremely large receptive fields [211], certainly larger than the differences in size between the stimuli we applied.

Next, we considered the encoding of the frequency of stimulation. PC afferents provided the highest frequency information, as predicted by the fact that PC afferents are well known to carry frequency information in vibrotactile stimulation [196]. Given their large receptive field size, frequency information of PC cells already saturated with the lowest density of afferents

considered. In agreement with previous studies, RA afferents also carried considerable information about frequency [196]. SA1 populations carried low amounts of frequency information at small spatial densities, but slightly exceeded the frequency information of RA afferents at higher spatial densities. This result may appear to contradict earlier empirical studies, where SA1 afferents were shown to respond only to the lower extreme of the range examined in our study [212]. However, in our simulations, the sinusoidal wave is superimposed on a ramp-and-hold indentation. This sustained indentation causes low spiking activity in the SA1 afferents, with spikes aligned to the vibration (see panel B in 21). Our finding suggests that this information emerges when taking into account the activity of SA1 afferents on a population level rather than single afferents separately.

PC afferents were also the most informative class about the stimulus ramp length, followed by SA1 and RA afferents, which provided similar levels of information, but required higher densities than PCs to reach saturation. Finally, SA1 afferents carried the highest amounts of information about ramp amplitude, with PC afferents not encoding any information. RA afferents again provided higher information than SA1 ones at the lowest density, but adding more fibers did not increase information for this class.

The information saturation density, which we defined as the smallest value of density at which the population carried the asymptotic value of information reached for the highest simulated density, was the highest across classes for SA1 afferent for all considered stimulus features. Conversely, the information saturation density was the smallest for PC afferents in all cases (Fig 17B). Notably, when considering purely spatial features such as the stimulus size, the population encoding the highest asymptotic information level corresponds to the one with the highest saturation density (Fig 17B and C). Consequently, a high density of afferents is required to extensively innervate a skin area and discriminate between fine differences in the shape of stimulation. On the other hand, when looking at temporal features such as the frequency or the ramp length, sparsely distributed PC afferents overcome the information content encoded by the other more densely packed afferent classes.

Finally, our result shows that the RA class at saturation density always encodes less information than the SA1 and PC populations about any feature considered in this study (Fig 17C). However,

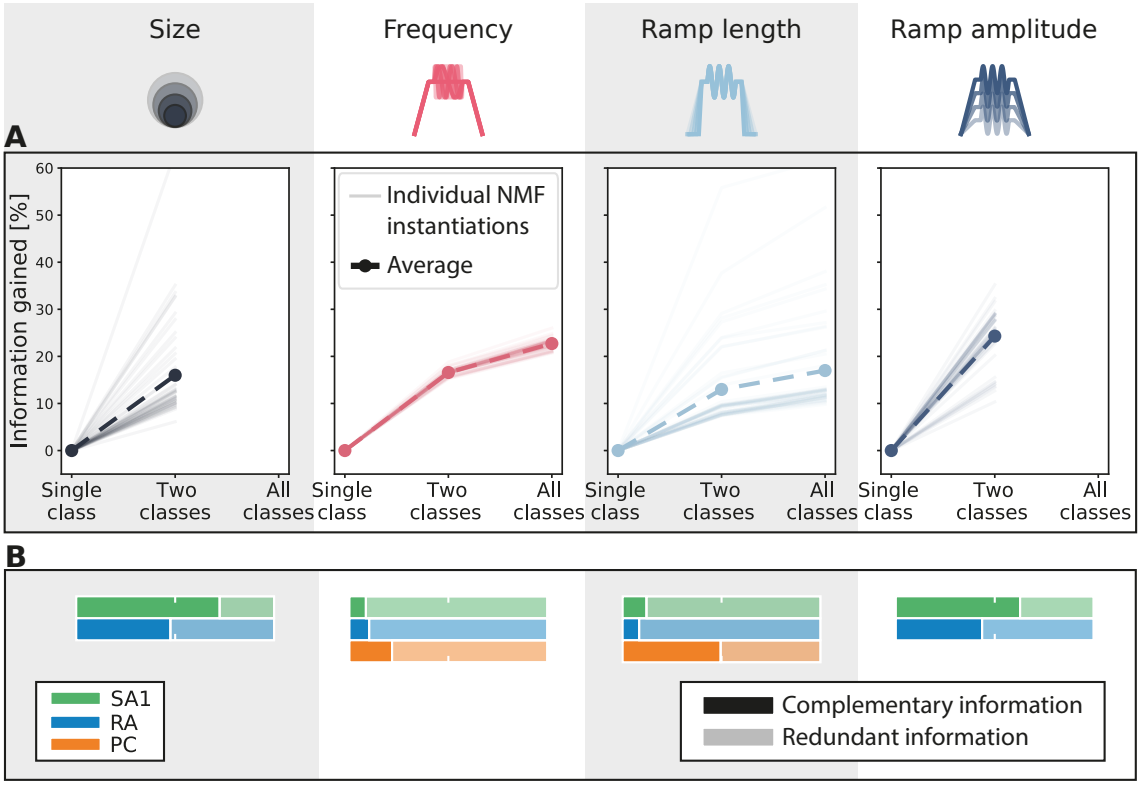


**Fig. 18: Integrating information across afferent classes. (A)** Information gain considering the two and the three most informative classes together with respect to the most informative class alone. The density measured on the human finger was taken for each afferent class. Thin lines correspond to different instantiations of the NMF decomposition, and the thick dashed lines correspond to their averages. **(B)** Decomposition of information into redundant and complementary contributions of each class with respect to the remaining two classes together. Information for each afferent class has been normalized to 100% and was calculated at the density measured on the human finger. Note that in both panels **(A)** and **(B)** only two afferent classes were considered for the analyses regarding stimulus size and ramp amplitude since the third class (PC) was carrying null information (see Fig 17C).

at low densities (<10 afferents/cm$^2$), RA afferents were more informative than SA1 for all features considered, suggesting that the optimal way to encode a tactile feature might depend on the number of neurons available.

## 2.2 Information encoded by multiple afferent classes

Next, we investigated how tactile stimulus information was encoded in the joint activity of multiple afferent classes. In particular, we asked whether the information about stimulus features carried by an afferent class adds to and complements the information carried by other classes or whether the information carried by different afferent classes is redundant. To answer this question, we computed the information carried about each stimulus feature by the joint activity of

populations of two or three afferent classes and compared the resulting values with the single-class information calculated above. Specifically, we used the concept of complementary information [213]: we defined the complementary information carried by additional afferent classes over that of a reference class as the information carried by all considered classes jointly subtracted by the information carried by the reference class alone. All possible combinations of classes were considered. In these calculations, unless otherwise stated, we set the density of each class to the one measured on the glabrous skin of the human finger (see Methods for details). This allowed us to compare the information contribution of different classes in a realistic and biologically relevant setting.

We first considered whether afferent classes that were not the principal source of information about a stimulus feature added information that was complementary to that of the principally contributing afferent class. To do so, for each feature, we quantified the amount of complementary information that the less informative classes add to the information carried by the most informative class (Fig 18A). The amount of this complementary information was normalized to the amount of stimulus information carried by the most informative class. For all features, we found that the second and third most informative classes added information that complements the information carried by the most informative class alone. On average, the second most informative class added between 12 and 25% complementary information, depending on the feature considered. When considered jointly, the second and third most informative classes added, on average, between 15 and 30% of complementary information, compared to the most informative class alone. This result indicates that for each tactile stimulus feature, each class encodes some amount of complementary information about the stimulus that cannot be found in the activity of the other two classes.

Next, we investigated which amount of each afferent class's information contribution was complementary or redundant when considered against the information contribution of the other afferent classes. For each stimulus feature and each individual afferent type, we computed the fraction of the information carried by the considered afferent that is complementary with respect to the information already carried by the other two afferent classes. This fraction is an index of the specific novelty of the information of a given afferent class with respect to all others (Fig 18B). In general, a significant fraction of information carried by each afferent class was complementary to that of other classes. In most cases, however, this fraction was not close to 1,

meaning that there was also redundancy between the information carried by afferent classes. When examining how this fraction varied across stimulus features, interesting patterns emerged.

For vibration frequency and ramp length, the two stimulus features for which all three afferent classes encoded considerable information, we found mostly redundant coding, with relatively small fractions of complementary information (on average 13% for frequency and 23% for ramp length, Fig 18B). All three classes encode vibratory stimuli by locking their spiking activity to the sinusoidal traces, which explains the redundancy across classes. However, the fact that the frequency ranges encoded by each class do not completely overlap explains the existence of significant fractions of complementary information across all three afferent classes. Given that all three classes encoded large amounts of frequency information, the actual amount of complementary information added by each class was surprisingly large (Fig 18B). A similar pattern of complementarity and redundancy of information was observed for ramp length, which like frequency is a dynamic feature that depends on timing.

For stimulus size, the SA1 afferent population carried most of the information (Fig 17), and this information had a high value of complementarity (72%), indicating that it could not be found in other afferent types (Fig 18B). The RA afferent population added less information (Fig 17), but also exhibited a relatively large fraction of complementarity (48%) (Fig 18B). The encoding of size for SA1 and RA afferents seems to depend on the number of afferents that are activated by the stimulus (Fig 21A), and the observed complementarity between RA and SA1 afferents is partly due to differences in spatial sensitivity across the two populations. Information carried by PCs about probe size was negligible and therefore this class was not considered in the complementarity analysis for this feature.

Finally, for ramp amplitude we found results that resemble those for stimulus size. The SA1 population carried most information, which was largely complementary (63%) to that of other classes. RA afferents carried less information than SA1 afferents, but part of this information (43%) was complementary to that of SA1 afferents. In this case, the encoding appears again to depend on the fraction of afferents that are activated by the stimulus, as was the case for stimulus size. This is a genuine form of population coding that would not be evident from single afferent analyses. PCs again provided negligible information (see Fig 17C), and thus were not taken into

account.

## 2.3 Effect of afferent density on complementary information

Having established that information about individual stimulus features is carried by multiple, rather than single, afferent classes and that different afferent classes often carry complementary stimulus information, we next asked how the complementarity of information depends on the spatial density of afferents. We were especially interested in whether, given the functional properties of afferents in each class, it would be more efficient to allocate all receptors to the most informative class or spread the receptors across different classes to take advantage of the complementarity of different classes. To address these questions, we systematically analyzed the information carried by individual afferent classes and their combination at different densities (Fig 19A). We tested the same upper and lower density limits as used previously. For a more realistic comparison with human biology, we also considered two other cases of spatial density arrangements, in which each population has a density equal to that experimentally found either in the palm or in the finger of the human hand (see Methods for precise numbers).

A substantial increase in the amount of encoded information was found for all features when increasing the density from the lower limit to realistic densities. Conversely, increasing the densities from the finger values further to the upper limit did not lead to additional increases of encoded information, neither when considering individual classes nor their combination, suggesting that the information in multi-class population coding saturates similarly to single-class coding. The only exception was probe size, for which information content at the upper limit was higher than at the finger density. As shown in Fig 19B and summarized in Table 8, stimulus size is also the only feature for which increasing the density of the most informative class, SA1, improves the information content more than combining different classes. As discussed previously, stimulus size is a purely spatial feature, and a high density of afferents is necessary to discern small differences in the shape of the stimulus. In contrast, for all other features considered, combining the content of the two most informative afferent classes yields more information than doubling the afferent density of the most informative class alone.

Together, these results show the advantages for information encoding at the population level of

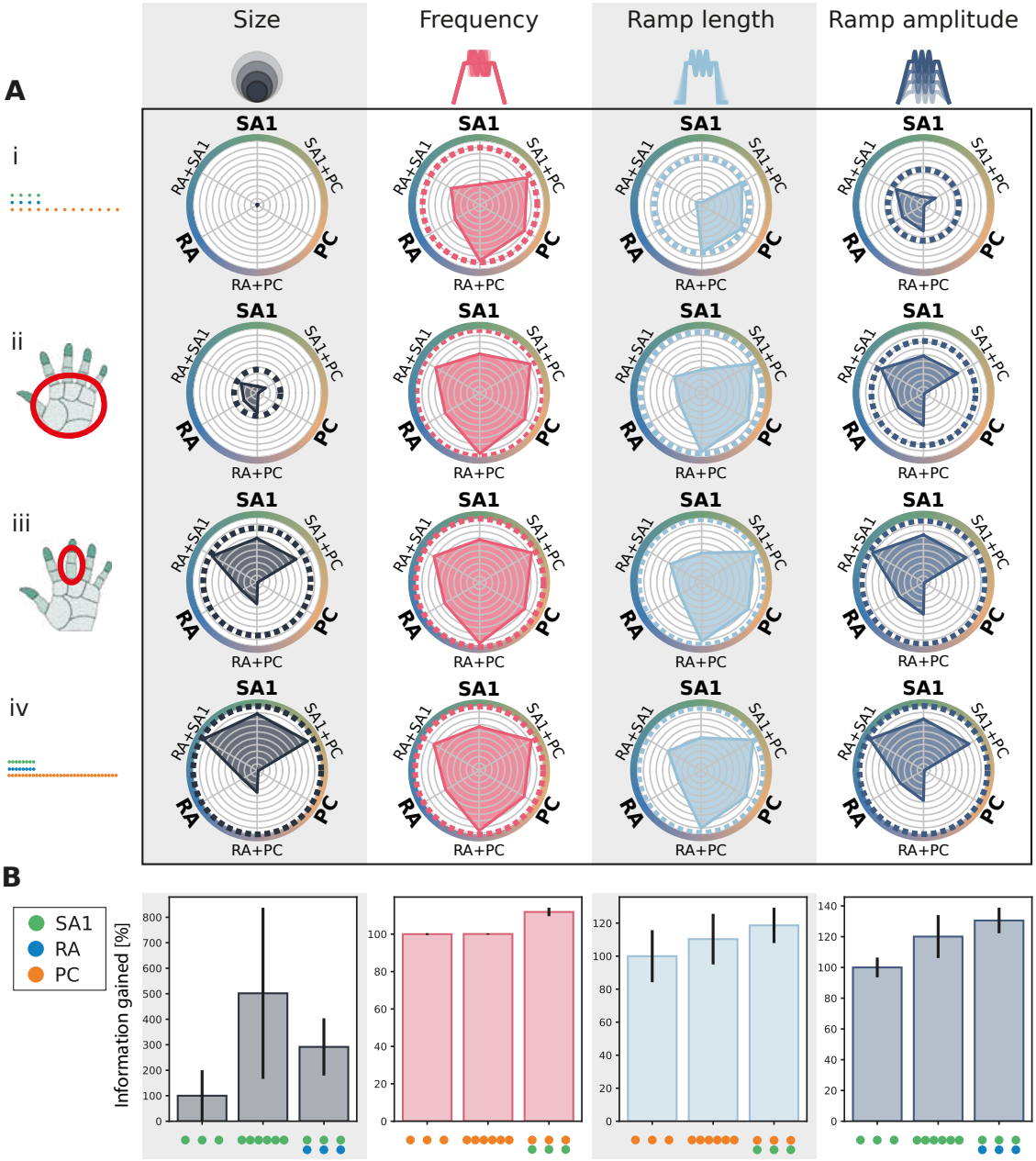


**Fig. 19: Information gain at different afferent densities. (A)** Radar plot of the information content provided by single and combined classes at different densities for individual tactile features. Each radial axis represents the information content of a single afferent class or combination of two classes. Dotted circular lines correspond to the information given by the three afferent classes together. Information is normalized for each stimulus feature with respect to the information provided by the three classes altogether at the upper-limit density (i). Four different density sets were considered: (i) lower limit, (ii) human palm, (iii) human finger, and (iv) upper limit as reported in Table 9. **(B)** Comparison of the information gained when doubling the density of the most informative class (central bar) or when combining with a different population (right bar). The baseline density (left bar) was set at 10 afferents/cm$^2$. Error bars represent standard deviation across different NMF instantiations.

| | Stimulus size | Frequency | Ramp length | Ramp amplitude |
|---|---|---|---|---|
| **Most informative class** | SAI | PC | PC | SAI |
| **Optimal encoding strategy** | Increase density of SAI population | Add SAI population | Add SAI population | Add RA population |
| **Underlying rationale** | Highest gain in information by increasing SAI density, PC provide no information | SAI adds more information than RA, PC information is density independent | SAI adds more information than RA, PC information is density independent | SAI+RA reaches the highest information content, PC provide no information |

**Table 8:** Information maximizing encoding strategies for each stimulus feature trading off increases in innervation density for a single afferent class versus adding fibers from a different class.

spreading information across classes of receptors with complementary information rather than simply packing more receptors of a given class into the skin, even if receptors of this class are highly informative about the stimulus.

## 2.4 Contributions of the spatial and temporal organization of population activity to population coding

After establishing how much information is encoded by each afferent class and their combinations, we investigated the nature of the population coding in more detail. In particular, we asked two questions relevant to understanding the spatial and temporal organization of the population code. First, how important is the precise temporal structure of the population activity for decoding stimuli from spatiotemporal patterns of neural population activity? Second, how important are differences in spatial neuron-to-neuron response profiles to decode stimulus information from spatiotemporal population activity?

The importance of the spatial structure of the afferent population code for information coding, that is, the afferent-to-afferent difference in stimulus tuning properties at different spatial locations, is supported by the finding that natural tactile stimuli elicit specific firing patterns in afferents located in different places [195, 214]. A critical role for the temporal structure of individual afferent activity has been demonstrated in previous studies [198, 215, 216] and is also supported by the fact that thalamic and cortical somatosensory neurons also encode tactile information with millisecond-scale spike timing precision [217–220]. However, it is unknown whether these expectations would hold at the level of afferent population coding. For example, precise spike timing might be less important when considering a full population of afferents rather than a single one. Furthermore, information in the spatial and the temporal structure might

be redundant, such that for example information contributed by the spike timing of the population may be redundant with the information encoded in the spatial structure, or vice versa. Addressing these questions, therefore, requires a direct test with a large population.

First, we evaluated whether the distribution of afferents in space, parameterized in the simulation as the distance of the afferent location from the stimulation site, impacts the population coding capabilities. To do so, we kept the NMF spatiotemporal modules computed on the original data and recomputed the NMF activation coefficients on the spiking activity obtained after destroying spatial information by randomly shuffling the neural responses across neurons for all time bins. Then we used the classifier trained on the original data to compute how much information about each stimulus feature could be decoded (see Methods). We called this "space-coding removed" information. The difference between the original and the space-coding removed information quantifies how much of the information in the original, unshuffled spike trains can only be expressed and decoded because of the spatial structure of the code. Note that this quantification is performed at a fixed spatial density, and it is thus different from the previous analyses of the effect of changing the spatial density. We found that, after destroying the spatial structure, information content dropped, averaged across classes and features, by 19% (Fig 20A). The loss of information was higher for SA1s (30%) compared with RAs (5%) or PCs (25%). Thus, the nature of how information is distributed across neurons at different locations provides a contribution to population coding that is lost and cannot be recovered by the temporal organization of activity when the spatial structure is destroyed.

Next, to quantify the specific contribution of temporal structure to decoding information from the spatiotemporal population activity, we computed a "time-coding removed" information value from the population responses. To do so, we randomly shifted the spikes with each shift independently drawn from a uniform distribution with range $\pm 2$, $\pm 5$, and $\pm 10$ ms before recomputing the NMF activation coefficients and estimating the information content (see Methods). The difference between the original and the time-coding removed information quantifies how much of the information that was decoded from the spatiotemporal population activity is contributed by the millisecond-scale temporal structure of the code. We found that, after destroying the temporal structure of the data with time shifts, the information decoded from spatiotemporal neural activity dropped, averaged across classes and features, by 7% with the 2

ms shift, 19% with the 5ms shift, and 28% with the 10 ms shift (Fig 20B). Information loss was highest for PCs (24%, 41%, and 61%, respectively, for the different time shifts) and relatively lower for RAs (5%, 15%, and 20%) and SA1s (2%, 12%, and 20%). Notably, across our set of stimuli, we found higher information loss when neglecting the temporal resolution of spike trains rather than the spatial distribution. This result indicates that even in large afferent populations spike timing with high temporal precision remains an important part of the spatiotemporal neural code. In particular, when examining features that can be expected to mostly rely on temporal structure, such as vibration frequency, information dropped significantly already with the smallest jitter of 2 ms. In contrast, other features, such as stimulus size, appear to rely more on spatial than temporal activation. For these features, information content was preserved when disrupting the temporal code but decreased abruptly when destroying the spatial structure in the data. Finally, we noticed that for some stimulus features the information content increased slightly after destroying spatial or temporal structure. These small increases should not be interpreted as indicating that more information is available at lower temporal resolutions (which would contradict the Data Processing Inequality), but rather indicating that in such cases we could not find evidence of timing information contributing at a finer scale. These effects arise spuriously in any decoding method that computes a lower bound on the population information, whose tightness may vary to some extent across conditions. They might also reflect how we simulated noise: since we simulated motor noise by varying parameters such as indentation depth, most of the neural noise in the afferent responses is likely correlated; adding a small, uncorrelated temporal jitter might have helped with decoding in some cases.

# 3 Discussion

This study is based on a simulation paradigm, which provides novel insights on stimulus coding by tactile afferent populations. Much of our current understanding of encoding mechanisms of tactile stimuli derives from electrophysiological studies. However, these are severely limited in the number of afferents that can be recorded at a time. In addition, many previous studies have focused only on those afferents terminating directly at the stimulus contact location. Thus, a biased picture of tactile coding might have emerged. In fact, to our knowledge, population coding of tactile afferents, taken as the spatiotemporal activation of multiple afferents belonging to one or *more*

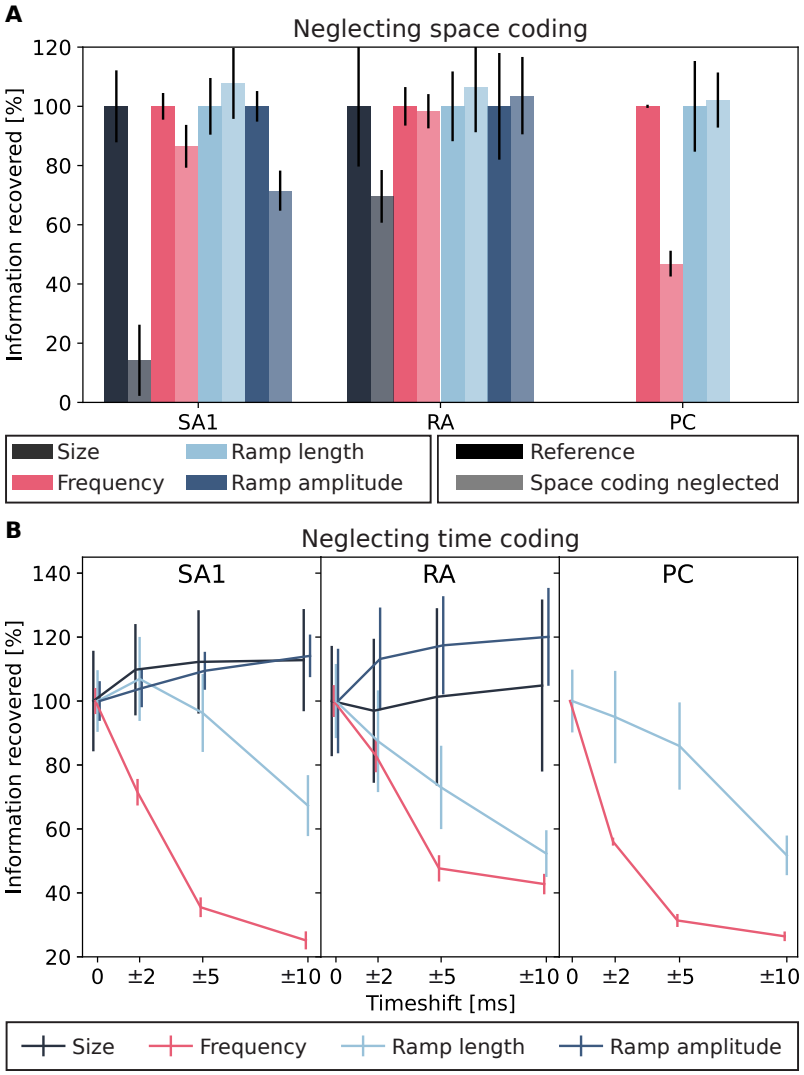


**Fig. 20: Information recovered after destroying spatial or temporal coding.** **(A)** Information recovered for each afferent class after neglecting afferents' spatial organization normalized with respect to the maximum information content in the original data at the saturation level (see Figure 17C). **(B)** Information recovered for each afferent class after destroying precise spike timing at different timescales. Again, information is normalized with respect to the maximum information content in the original data at the saturation level. Error bars represent standard deviation across different NMF instantiations. Note that for both stimulus size and ramp amplitude, information carried by PC class was null (see Figure 17C) and such class was excluded from these analyses.

classes, has scarcely been investigated before. Here, we used a recently developed computational model that allows simulation of tactile neural responses at the population level with high accuracy. Although any putative population-level coding mechanisms derived from modeling would need to be experimentally verified, this approach allows investigating aspects of the neural code that are currently experimentally intractable and can therefore generate ideas for potential downstream

decoding mechanisms.

## 3.1 Single-class coding and receptor density

We first investigated how the density of afferents from a single class plays a role in the encoding process. We showed that the information content of both SA1 and RA populations increases asymptotically with afferent density until saturation. This effect was consistent for all features considered, although the specific saturation densities varied between features. This result highlights that tactile information is generally spread across a population of multiple afferents, even for features that are not explicitly spatial. Furthermore, the afferent class most informative about a tactile feature at low innervation densities might be different from the most informative class at high densities. Consequently, judging or predicting the information content of a population from recordings of single afferents only might be misleading and provide a biased picture of how information is represented in full populations.

In contrast to SA1 and RA afferents, the information level for PC afferents was essentially constant for all density values considered across all tactile features. While this result might be taken to suggest that the PC population does not contribute information above that of a single afferent, there is evidence to suggest that PC populations might be important in different tactile contexts than the ones explored here: making contact with surfaces causes mechanical waves to spread throughout the hand, activating PC afferents as far away as the palm and their joint population activity carries information about how contact is made and other aspects of the grasp [221].

It should be noted that for all afferent classes, the minimum density needed to recover the maximum information for any tactile feature is lower than the empirical afferent densities estimated for the human hand [193]. We speculate that the minimum density of afferents required to reach the information saturation might be higher for more complex features. Indeed, as an initial investigation into the power of large-scale neural simulations on a population level, this study considered relatively simple stimulus features compared to the complexity of realistic tactile interaction. Similarly, previous studies showed a strong relationship between SA1 density and tactile spatial acuity [193]: afferents, particularly of SA1 type, need to be densely packed in the skin to resolve and discriminate extremely fine features. While our setup included one clearly

spatial stimulus (probe size), none of the others were purely spatial. Finally, afferent innervation densities across most of the skin of the human body are much lower than those in the hand and indeed within the range identified in the current study, suggesting that our stimulus set was covering a large part of the physiologically relevant range.

Interestingly, we found that the RA class at saturation density tended to encode less information than the SA1 and PC populations, but in contrast, was more informative than SA1s at low densities ($< 10$ afferents/cm$^2$). This result suggests that the way information is spread across afferent classes depends in part on receptor density, and in turn, should affect optimal decoding downstream. Indeed, tactile innervation density changes dramatically across different body areas, both in terms of the absolute number of afferents and relative innervation densities of different classes [193], and it is possible that changes in the class composition at different skin sites partially reflect density-dependent optimal allocation of afferent classes. Our findings also suggest that tactile information need not be linked firmly to a given receptor type, but that information is spread in a dynamic way across different afferent classes (see [201] for a concrete example in frequency coding).

## 3.2 Complementarity and redundancy across afferent classes

The second step of our analysis was to consider combinations of afferent classes and to evaluate their information content with respect to different stimulus features. Here, we found both redundant and complementary contributions to the information across afferent classes. All afferent classes generally provided at least some complementary information about stimulus features, suggesting that downstream areas should integrate information from different classes to maximize information (see also [197]). Quantifying such complementary information is a necessary first step towards further study of submodality convergence in the stimulus encoding process, especially considering that directly accessing the integration mechanisms in humans is complicated. Convergence has previously been inferred from cortical recordings in primates for multiple individual stimulus attributes [200, 222, 223], but here we quantitatively demonstrate that information is spread across afferent types in most cases, and therefore, submodality integration can be expected to be a general feature of downstream processing.

Not all information was complementary however, and we also found considerable degrees of redundancy between afferent classes. Redundancy in neural coding has been extensively debated (see [224] for a review) and can be a strategy for robust stimulus encoding. Indeed, over-representing stimulus information using large populations of neurons increases the probability of having a relevant impact in downstream neurons, guaranteeing —or, at least, making more plausible— that critical information is processed while negligible information is discarded —or less likely used—. Redundancy can rank information according to relevance, overcoming the associated coding inefficiency in favor of a significant performance increase [225]. Furthermore, redundancy could be interpreted as a strategy to make the neural code resilient in the event of temporary or permanent lack, shortage, or failure of input from an afferent class. This theory is supported by recent findings in an experimental study in mice that showed that the use of genetic ablation strategies to suppress the response of either rapidly or slowly adapting afferents leaves responses in the somatosensory cortex mostly unchanged [199], which implies that the required information can be recovered from the remaining afferent input. This would not have been possible if the two classes had encoded complementary information only. Such a process might be beneficial when several features are processed simultaneously, and redundancy between classes might help to disambiguate the stimulus.

## 3.3 Information maximizing receptor selection

We investigated whether increasing the density of afferents of a given class or combining them with afferents of a different class yields higher information gain. We found that adding afferents belonging to a different class was generally more efficient than increasing the density of the most informative class by the same amount, confirming that the information about stimulus features is not segregated in single afferent classes, but is spread across them. Indeed, while absolute tactile innervation densities vary widely across the body, the fraction of slowly adapting afferents at any given site varies only between 40 and 70% and is relatively evenly split for most body regions [193], especially for those with lower innervation. Our results suggest that such a composition increases information transmission, while minimizing fiber count. The number of tactile fibers that can fit into the nerves and spinal cord is naturally constrained, and consequently, extensive skin areas are innervated at low density. Neurons are also energetically expensive, and therefore

it is plausible that evolutionary optimization might have maximized the ratio between information and energy consumption by spatially distributing the mechanoreceptors and diversifying response properties across different receptor classes.

In several sensory systems other than touch neural populations are also composed of multiple cell classes with distinct response properties. Indeed, early sensory pathways frequently split into different classes with disparate response properties (e.g. the large number of retinal ganglion cell classes [188]). According to the efficient coding hypothesis, sensory systems have evolved to optimally transmit information about the surrounding world, given constraints on their biophysical components and energy use [226]. This theory also explains splitting a population into two or more cell classes as a strategy to maximize information transmission, as shown in previous studies for different sensory systems [190–192]. Our findings support this hypothesis, showing that, in most cases, a combination of classes was more informative than a single class higher-density population.

## 3.4 Limitations and future work

Our study focused on the three main classes of tactile afferents that mediate discriminative touch. However, other classes also contribute to tactile coding, such as SA2 afferents, which are thought to primarily signal skin stretch but are consciously perceivable [227]. Furthermore, tactile innervation and neural response properties differ somewhat in the hairy skin [193], which covers most of the human body. Thus, our results will most directly reflect tactile coding on the human hand, but future studies should consider how these results might extend to other regions of the body.

As the findings are based on computer simulations, the veracity of the results will depend on the accuracy with which the spiking responses can be replicated in the computational model. The stimuli we used, namely indentations by a single probe orthogonal to the skin surface with a superimposed vibration, are similar to those on which the original model was fit and fall into the range where it has been validated most extensively [202]. Still, by combining multiple tactile features, we believe that our simulated stimuli are sufficiently complex, varied, and natural that the resulting findings can be considered of behavioral importance. One avenue for future research would be to investigate information transfer on tactile inputs arising from natural behaviors such

as grasping and manipulating objects, which include multiple contacts, shear forces, and movement between the object and the skin. However, this would require further work on the precise spatiotemporal force patterns on the hand during such behaviors and spiking models that take into account more complex afferent response properties (see [228] for an example).

To study the effects of different innervation densities, we considered a simplified setup, distributing the afferents over a single dimension while neglecting some properties affecting the spatial distribution of afferents, for example the complex shape of the human hand. Future studies should take this aspect into account to reveal how the shape of the hand, the different afferent densities, and the composition of the population in different areas of the hand plays a role in stimulus encoding. In the same direction, population coding strategies and afferent distribution might be coupled with natural stimulus statistics in different body areas to deepen the understanding of how the human somatosensory system is optimised to receive and process natural tactile stimuli.

Finally, as in other information-theoretic analyses on large-dimensional neural response spaces, our analysis can only provide a lower bound on the true information contained in the population spiking patterns. As direct calculation of the information is prohibitive with respect to the amount of data that would be required, we chose a method that decomposes the high-dimensional responses, with information values subsequently estimated in the lower-dimensional space. An additional benefit of this method is that the initial unsupervised decomposition of the neural responses reflects aspects of neural processing in sensory pathways. However, the resulting information values will be affected by choices regarding this decomposition specifically, and the information calculation more generally, and different choices might yield somewhat different outcomes. To directly test the robustness of our method, we compared our method with a different analysis pipeline. We found qualitatively very similar results, suggesting that our main findings, for example regarding the benefits of integrating across different afferent classes, hold generally, rather than being dependent on the specific analysis method chosen.

# 4 Methods

| Class | Palm | Finger | Fingertip |
|---|---|---|---|
| SAI | 10 | 30 | 70 |
| RA | 25 | 40 | 140 |
| PC | 10 | 10 | 25 |

**Table 9:** Estimated innervation densities of afferent classes (afferents/cm$^2$) for different regions of the human hand [211].

## 4.1 Simulation of spiking activity

To generate the spiking activity of tactile afferents, we used a previously published and validated model called Touchsim [202]. We employed the model to simulate populations of SA1, RA, and PC afferents terminating along a line of 1 cm for SA1s and RAs, and 5 cm for PCs radiating outwards from the stimulus location. The density of afferents varied between 1 and 140 afferents/cm$^2$ for a total of 16 different populations per afferent type. This range includes the physiological innervation densities estimated for the human hand [211]. In some analyses, we also directly set individual class densities to those of the human palm or finger (see Table 9 for precise values).

We designed stimuli with circular shapes, which are indented in the skin following a ramp-and-hold function (see Fig 15 B). When the maximum amplitude of the ramp is reached, a sinusoidal wave is superimposed. This setup simulates well-established psychophysical setups in which a probe is brought into contact with the skin and then vibrated at a set frequency. It also includes many aspects of natural tactile stimulation: indentation, retraction, and constant stimulation at different depths and spatial scales, as well as vibrations at different frequencies. Individual stimuli are created by varying 4 different features: 1) the stimulus size (4 conditions: [1:1:4] mm), 2) the maximum ramp amplitude (4 conditions: [0.3:0.3:1.2] mm), 3) the ramp-up time (5 conditions: [0.01:0.01:0.05] s), and 4) the frequency of the superimposed sinusoidal wave (10 conditions: [0, 10, 20, 40, 60, 80, 100, 130, 160, 200] Hz). This setup yielded 800 unique stimuli, and the afferent response to each was simulated for 40 trials. The model included simulated neural noise. Additionally, in order to simulate environmental noise such as motor noise during active touch, we jittered the stimulus location (by $\pm$ 0.3 mm), the amplitude of the sinusoidal wave (by $\pm$ 0.05 mm), and the ramp amplitude (by $\pm$ 0.1 mm) on every trial.

## 4.2 Unsupervised spatiotemporal NMF

Information calculations from high dimensional data require prohibitively large datasets. A common strategy to address this issue is by first performing unsupervised dimensionality reduction on the data. Here, we used spatiotemporal Non-Negative Matrix Factorization (NMF) to decompose the spatiotemporal matrix of spiking responses across the population.

Responses were discretized by binning the spike trains into 2-ms intervals and counting the number of spikes falling into each bin. This resulted in a matrix $R \in \mathbf{R}^{M \times TN}$, where $M$ is the total number of trials, $T$ the number of time bins, and $N$ the number of afferents in the population. NMF decompositions are naturally suited to describe spatiotemporal matrices of spiking responses, because spike trains are non-negative, and because commonly occurring spike patterns may be non-orthogonal and partly overlapping, and NMF does not require assumptions of orthogonality or non-overlap of different activity modules. NMF describes a single trial spike train as a sum of trial-independent non-negative spatiotemporal modules (describing the most often recurring spatiotemporal firing patterns) and trial-dependent non-negative activation coefficients representing the strength of recruitment of each module in the considered trial [204, 205]:

$$R = HW + residuals, \tag{29}$$

where $H \in \mathbf{R}^{M \times K}$ contains the non-negative activation coefficients for the $K$ modules in each trial and $W \in \mathbf{R}^{K \times TN}$ contains the non-negative modules. We used the function *NMF* included in the scikit-learn Python library [229] to calculate the NMF decomposition.

We performed the NMF decomposition separately for each of the three afferent classes at each density value considered. Beforehand, we randomly separated the whole set of trials into balanced sets with a 25/75 split. We used the 25-set to determine the number of modules $K$ as the minimum number of modules capable of explaining a selected level of variance of the original data in $R$, as follows. First, to consistently select the level of variance explained between populations of the same class but with different densities, we calculated the saturation level of the accounted variance for each population considered (tolerance <1%). We averaged the saturation levels across populations of the same class with different densities and used this value as the new threshold for the explained variance. Finally, we calculated $k$ modules $W$ and activation coefficients $H$ on the

same 25-set. Given the $W$ modules from the 25-set, we computed the activation coefficients $H$ on the remaining 75-set. Given the random initialization of the spatiotemporal basis functions with the NMF decomposition, we computed 50 instantiations of the NMF to account for the variability of the method.

## 4.3 Stimulus decoder

After dimensionality reduction, we fed the activation coefficients $H$ computed with the NMF to a stimulus decoder. We used multinomial logistic regression to decode each stimulus feature separately on a trial-by-trial basis based on the neural activity (similarly to [209]). The scikit-learn Python library [229] was used for the implementation. This type of classifier uses a linear function $f(s, i)$ to predict the probability of outcome $s$ for trial $i$ such that:

$$f(s, i) = \beta_s \cdot \mathbf{H}_i \tag{30}$$

where $\mathbf{H}_i$ is a vector containing the NMF activation coefficients for trial $i$ and $\beta_k$ stores the coefficients associated with outcome $s$. When generalizing to $S_n$ features, the multinomial logistic regression model consists of $S_n - 1$ independent logistic regression models regressed against the remaining $S_n$ outcomes. Note that outcomes correspond to the possible values that the stimulus features could take and vary for each feature.

The 75-set was divided equally and stratified into training and test sets. We trained the classifier on the activation coefficients of the training set and evaluated performance using the activation coefficients of the test set. The training procedure was performed using a stratified 5-fold cross-validation. This process was repeated for each population of afferents (both for single and combined classes) and all afferent densities. The solver used for the fitting procedure was *lbfgs* in combination with *L2* regularization. We selected the parameter *C* for the regularization by performing grid search. The scoring of the classifier was the negative log-likelihood, also known as the cross-entropy loss.

The final fitted model outputs the posterior probability of observing each stimulus feature given the neural activity captured in the NMF activation coefficients [209]. From this posterior probability, we decoded the stimulus $\hat{s}$ that was most likely given the observed afferent activity.

## 4.4 Mutual Information

Next, we computed the mutual information [230] from the confusion matrix of the decoder as follows [184]:

$$I(S;\hat{S}) = \sum_{s\in S}\sum_{\hat{s}\in\hat{S}} p(s,\hat{s}) \log_2 \left( \frac{p(s,\hat{s})}{p(s)p(\hat{s})} \right) \tag{31}$$

where $S$, $\hat{S}$ stand for the set of all possible presented and decoded stimuli, respectively. $p(s,\hat{s})$ denotes joint probability distribution, which is derived from the confusion matrix obtained empirically across all trials, of presenting stimulus $s$ and decoding stimulus $\hat{s}$ in a given trial. $p(s)$ and $p(\hat{s})$ correspond to the marginal probabilities of $s$ and $\hat{s}$, respectively. The information in the confusion matrix is a data-robust lower bound to the total information carried by population activity. This approximation is tight when neural activity can be categorically binned into as many values as the number of distinct stimuli without losing considerable information. The information in the confusion matrix captures aspects of information processing, such as the distribution of decoding errors, which are not captured by simple measures such as the fraction of correctly decoded stimuli [184]. Since the information upper bound is the entropy of the stimulus set (indicating perfect single-trial stimulus discrimination), we normalised information values by dividing them by the entropy of the stimulus set:

$$H(S) = \log_2(S_n) \tag{32}$$

where $S_n$ is the number of values that the stimulus can take.

## 4.5 Computation of complementary information

To assess the complementarity of stimulus information carried by different classes, we computed the information carried about each stimulus feature by the joint activity of populations of two or three afferent classes and compared it to the information carried by a single-class population. We defined the amount of information carried by the pair of afferent classes that is complementary to that of a reference class as the difference between the information carried by all the classes (including the reference class and the additional ones) and the information carried by the reference class. We repeated this process, taking each class as the reference class in turn. As an example,

for SA1 afferents as the reference class, the complementary information is computed as:

$$\begin{aligned} I_{comp}(S, SA1) =& I(S, \{SA1, RA, PC\}) \\ & - I(S, \{RA, PC\}) \end{aligned} \tag{33}$$

We defined the redundant information between the additional classes and the reference class as the sum of the information carried individually by the reference class and the additional ones minus the information carried by all the classes together, such that (again, taking SA1s as the reference class):

$$\begin{aligned} I_{red}(S, SA1) =& I(S, SA1) \\ & + I(S, \{RA, PC\}) \\ & - I(S, \{SA1, RA, PC\}) \end{aligned} \tag{34}$$

The sum of redundant (eq. 34) and complementary (eq. 33) information for a class equals the total information carried by that class.

## 4.6 Contribution of spatial and temporal structure of neural activity to population coding

We assessed the contribution of fine temporal and spatial resolution within the spiking activity to information coding by destroying the temporal and spatial structures in the data. To destroy the spatial structure, we randomly permuted the order of afferents in the spiking matrix $R$. Then, keeping the non-negative modules $W$ obtained with the NMF decomposition on the original, non-shuffled data, we computed the activation coefficients on the spatial-shuffled data. We finally used these activation coefficients to feed the classifier previously trained on the original activation coefficients. To destroy the temporal structure in the data, we randomly shifted the spikes with a uniform distribution of ±2, ±5, and ±10 ms. Then, as for the spatial case, we obtained the activation coefficients on the time-shuffled data and used those to feed the classifier trained on the original data and estimate the residual information content after disrupting the data temporal structure.

### Control analysis using spatial NMF and supervised decoding of temporal structure

To test the robustness of the analysis pipeline with respect to the choice of low-dimensional representation, we calculated information values from an alternative NMF decomposition of the data. We first computed the spike count over the whole trial, $R_{count}$. We then applied the NMF decomposition on $R_{count}$ to find spatial modules $W_{space}$ capturing which afferents are firing together, such that:

$$R_{count} = H_{count} W_{space} + residuals. \tag{35}$$

The tolerance criterion for selecting the number of modules $M$ was the same as described above for the spatiotemporal NMF.

We computed a single set of spatial modules using the population activity pooled over all time bins. We then calculated a different activation coefficient $H_t$ for each spatial module and time bin producing in total a number of activation coefficients per trial equal to the product of the number of modules $M$ times the number of time bins $T$, a larger number than the activation coefficients per trial of the spatiotemporal NMF decomposition described above (which only produced $M$ activation coefficients per trial).

For the supervised decoding of the activation coefficients in each trial, we used the same GLM decoder described above.

# Supporting information

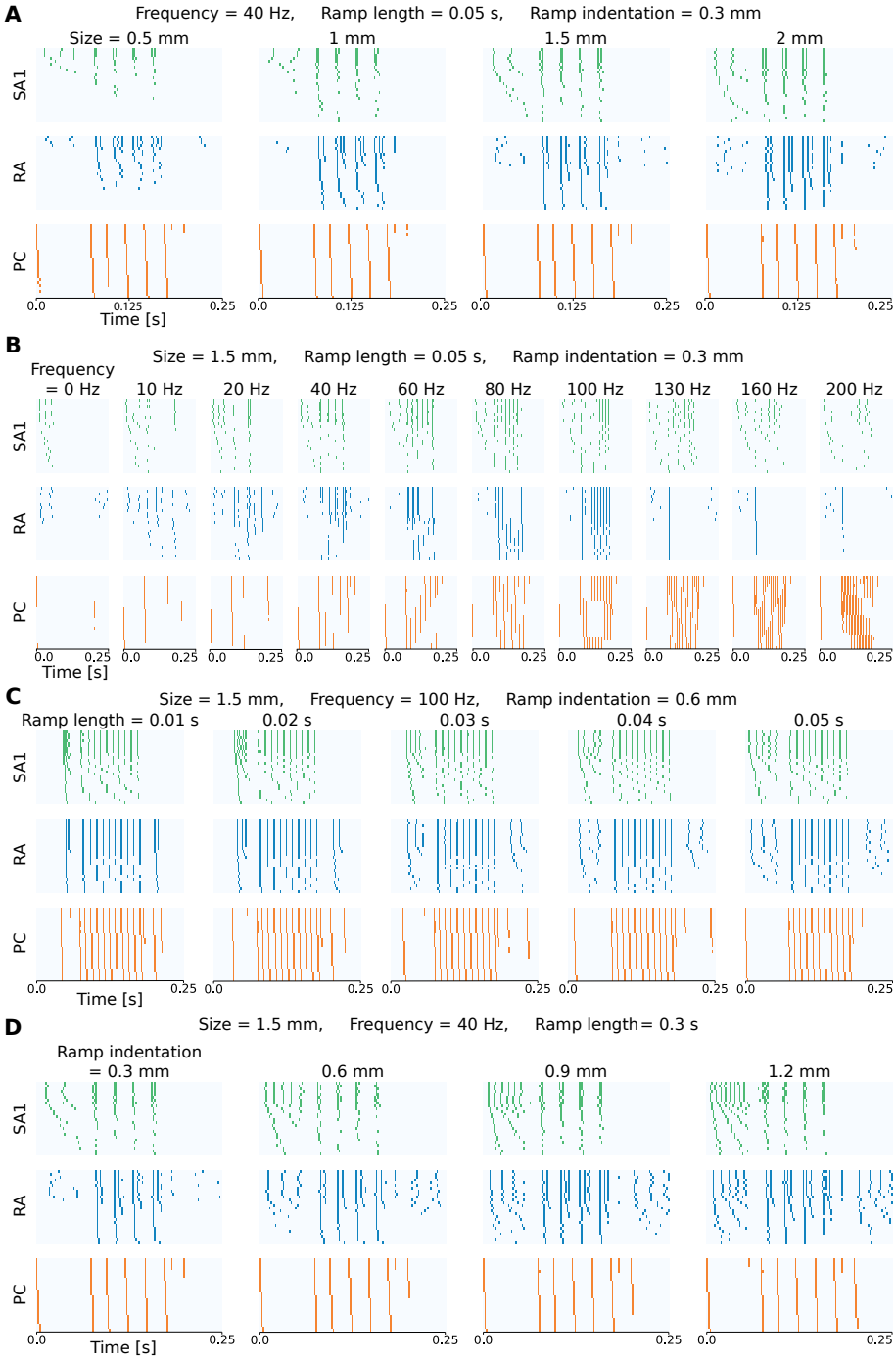


**Fig. 21: Illustrative examples of simulated spiking activity.** Responses are shown for the three afferent classes as a function of **(A)** stimulus size, **(B)** frequency, **(C)** ramp length, and **(D)** ramp amplitude. Note that we conditioned on the remaining features for each panel and that the afferent densities in this example are the ones in the finger.

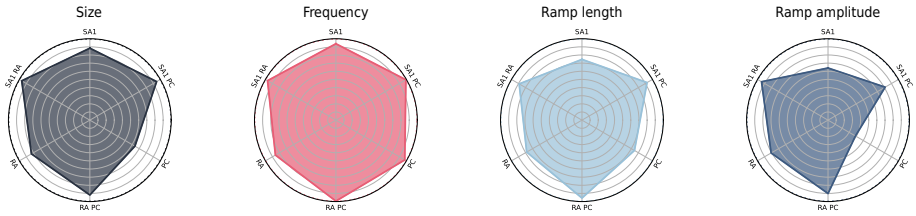


**Fig. 22: Robustness of findings using a spatial NMF decomposition of neural responses.** Responses are shown for the three afferent classes as a function of **(A)** stimulus size, **(B)** frequency, **(C)** ramp length, and **(D)** ramp amplitude. Note that we conditioned on the remaining features for each panel and that the afferent densities in this example are the ones in the finger.

# References

[183] A. Pouget, P. Dayan, and R. Zemel, "Information processing with population codes," *Nat. Rev. Neurosci.*, vol. 1, no. 2, pp. 125–132, Nov. 2000.

[184] R. Quian Quiroga and S. Panzeri, "Extracting information from neuronal populations: information theory and decoding approaches," *Nat. Rev. Neurosci.*, vol. 10, no. 3, pp. 173–185, Mar. 2009.

[185] A. P. Georgopoulos, A. B. Schwartz, and R. E. Kettner, "Neuronal population coding of movement direction," *Science*, vol. 233, no. 4771, pp. 1416–1419, Sep. 1986.

[186] E. Schneidman, J. L. Puchalla, R. Segev, R. A. Harris, W. Bialek, and M. J. Berry, "Synergy from silence in a combinatorial neural code," *Journal of Neuroscience*, vol. 31, no. 44, pp. 15 732–15 741, Nov. 2011.

[187] M. Adibi, J. S. McDonald, C. W. G. Clifford, and E. Arabzadeh, "Population decoding in rat barrel cortex: Optimizing the linear readout of correlated population responses," *PLoS Comput. Biol.*, vol. 10, no. 1, pp. e1 003 415–e1 003 415, Jan. 2014.

[188] T. Baden, P. Berens, K. Franke, M. Román Rosón, M. Bethge, and T. Euler, "The functional diversity of retinal ganglion cells in the mouse," *Nature*, vol. 529, no. 7586, pp. 345–350, Jan. 2016.

[189] V. E. Abraira and D. D. Ginty, "The sensory neurons of touch," *Neuron*, vol. 79, no. 4, pp. 618–639, Aug. 2013.

[190] J. Gjorgjieva, H. Sompolinsky, and M. Meister, "Benefits of pathway splitting in sensory coding," *J. Neurosci.*, vol. 34, no. 36, pp. 12 127–12 144, 2014.

[191] D. B. Kastner, S. a. Baccus, and T. O. Sharpee, "Critical and maximally informative encoding between neural populations in the retina," *Proceedings of the National Academy of Sciences*, vol. 112, no. 8, pp. 2533–2538, Feb. 2015.

[192] J. Gjorgjieva, M. Meister, and H. Sompolinsky, "Functional diversity among sensory neurons from efficient coding principles," *PLoS Comput. Biol.*, vol. 15, no. 11, p. e1007476, Nov. 2019.

[193] G. Corniani and H. P. Saal, "Tactile innervation densities across the whole body," *J. Neurophysiol.*, vol. 124, no. 4, pp. 1229–1240, Oct. 2020.

[194] R. S. Johansson and A. B. Vallbo, "Tactile sensibility in the human hand: relative and absolute densities of four types of mechanoreceptive units in glabrous skin," *J Physiol (Lond)*, vol. 286, pp. 283–300, Dec. 1979.

[195] A. W. Goodwin and H. E. Wheat, "Sensory signals in neural populations underlying tactile perception and manipulation," *Annu. Rev. Neurosci.*, vol. 27, pp. 53–77, Dec. 2004.

[196] K. O. Johnson, "The roles and functions of cutaneous mechanoreceptors," *Curr. Opin. Neurobiol.*, vol. 11, no. 4, pp. 455–461, Aug. 2001.

[197] H. P. Saal and S. J. Bensmaia, "Touch is a team effort: interplay of submodalities in cutaneous sensibility," *Trends Neurosci.*, vol. 37, no. 12, pp. 689–697, Sep. 2014.

[198] A. I. Weber, H. P. Saal, J. D. Lieber, J.-W. Cheng, L. R. Manfredi, J. F. Dammann, 3rd, and S. J. Bensmaia, "Spatial and temporal codes mediate the tactile perception of natural textures," *Proc. Natl. Acad. Sci. U. S. A.*, vol. 110, no. 42, pp. 17 107–17 112, Oct. 2013.

[199] A. J. Emanuel, B. P. Lehnert, S. Panzeri, C. D. Harvey, and D. D. Ginty, "Cortical responses to touch reflect subcortical integration of ltmr signals," *Nature*, vol. 600, no. 7890, pp. 680–685, Oct. 2021.

[200] H. P. Saal, M. A. Harvey, and S. J. Bensmaia, "Rate and timing of cortical responses driven by separate sensory channels," *Elife*, vol. 4, no. 12, pp. 7250–7257, 2015.

[201] I. Birznieks, S. McIntyre, H. M. Nilsson, S. S. Nagi, V. G. Macefield, D. A. Mahns, and R. M. Vickery, "Tactile sensory channels over-ruled by frequency decoding system that utilizes spike pattern regardless of receptor type," *Elife*, vol. 8, Aug. 2019.

[202] H. P. Saal, B. P. Delhaye, B. C. Rayhaun, and S. J. Bensmaia, "Simulating tactile signals from the whole hand with millisecond precision," *Proceedings of the National Academy of Sciences*, vol. 114, no. 28, pp. 201 704 856–201 704 856, Jun. 2017.

[203] D. D. Lee and H. S. Seung, "Learning the parts of objects by non-negative matrix factorization," *Nature*, vol. 401, no. 6755, pp. 788–791, Oct. 1999.

[204] A. Onken, J. K. Liu, P. P. C. R. Karunasekara, I. Delis, T. Gollisch, and S. Panzeri, "Using matrix and tensor factorizations for the Single-Trial analysis of population spike trains," *PLoS Comput. Biol.*, vol. 12, no. 11, p. e1005189, Nov. 2016.

[205] P. L. Williams and R. D. Beer, "Nonnegative decomposition of multivariate information," *arXiv preprint arXiv:1004.2515*, 2010.

[206] S. A. Overduin, A. d'Avella, J. Roh, J. M. Carmena, and E. Bizzi, "Representation of muscle synergies in the primate brain," *Journal of Neuroscience*, vol. 35, no. 37, pp. 12 615–12 624, 2015. [Online]. Available: https://www.jneurosci.org/content/35/37/12615

[207] S.-P. Kim, Y. N. Rao, D. Erdogmus, J. C. Sanchez, M. A. L. Nicolelis, and J. C. Principe, "Determining Patterns in Neural Activity for Reaching Movements Using Nonnegative Matrix Factorization," *EURASIP Journal on Advances in Signal Processing*, vol. 2005, no. 19, p. 829802, Nov. 2005. [Online]. Available: https://doi.org/10.1155/ASP.2005.3113

[208] J. Wei, W. Bai, T. Liu, and X. Tian, "Functional connectivity changes during a working memory task in rat via nmf analysis," *Frontiers in Behavioral Neuroscience*, vol. 9, 2015. [Online]. Available: https://www.frontiersin.org/articles/10.3389/fnbeh.2015.00002

[209] C. A. Runyan, E. Piasini, S. Panzeri, and C. D. Harvey, "Distinct timescales of population coding across cortex," *Nature*, vol. 548, no. 7665, pp. 92–96, 2017.

[210] S. Noei, I. S. Zouridis, N. K. Logothetis, S. Panzeri, and N. K. Totah, "Distinct ensembles in the noradrenergic locus coeruleus are associated with diverse cortical states," *Proceedings of the National Academy of Sciences*, vol. 119, no. 18, p. e2116507119, 2022. [Online]. Available: https://www.pnas.org/doi/abs/10.1073/pnas.2116507119

[211] A. B. Vallbo' and R. S. ohansson, "Properties of cutaneous mechanoreceptors in the human hand related to touch sensation," *Hum. Neurobiol.*, vol. 3, pp. 3–14, 1984.

[212] E. Ribot-Ciscar, J. P. Vedel, and J. P. Roll, "Vibration sensitivity of slowly and rapidly adapting cutaneous mechanoreceptors in the human foot and leg," *Neurosci. Lett.*, vol. 104, no. 1-2, pp. 130–135, Sep. 1989.

[213] S. Panzeri, N. Brunel, N. K. Logothetis, and C. Kayser, "Sensory neural codes using multiplexed temporal scales," *Trends Neurosci.*, vol. 33, no. 3, pp. 111–120, Mar. 2010.

[214] H. P. Saal, S. Vijayakumar, and R. S. Johansson, "Information about complex fingertip parameters in individual human tactile afferent neurons," *J. Neurosci.*, vol. 29, no. 25, pp. 8022–8031, Jun. 2009.

[215] E. L. Mackevicius, M. D. Best, H. P. Saal, and S. J. Bensmaia, "Millisecond precision spike timing shapes tactile perception," *J. Neurosci.*, vol. 32, no. 44, pp. 15 309–15 317, Oct. 2012.

[216] R. S. Johansson and I. Birznieks, "First spikes in ensembles of human tactile afferents code complex spatial fingertip events," *Nat. Neurosci.*, vol. 7, no. 2, pp. 170–177, Feb. 2004.

[217] K. H. Long, J. D. Lieber, and S. J. Bensmaia, "Texture is encoded in precise temporal spiking patterns in primate somatosensory cortex," *bioRxiv*, 2021.

[218] S. Panzeri, R. S. Petersen, S. R. Schultz, M. Lebedev, and M. E. Diamond, "The role of spike timing in the coding of stimulus location in rat somatosensory cortex," *Neuron*, vol. 29, no. 3, pp. 769–777, Mar. 2001.

[219] R. S. Petersen, S. Panzeri, and M. E. Diamond, "Population coding of stimulus location in rat somatosensory cortex," *Neuron*, vol. 32, no. 3, pp. 503–514, Nov. 2001.

[220] ——, "The role of individual spikes and spike patterns in population coding of stimulus location in rat somatosensory cortex," *Biosystems.*, vol. 67, no. 1-3, pp. 187–193, Oct. 2002.

[221] Y. Shao, V. Hayward, and Y. Visell, "Compression of dynamic tactile information in the human hand," *Science Advances*, vol. 6, no. 16, p. eaaz1158, Apr. 2020.

[222] Y.-C. Pei, P. V. Denchev, S. S. Hsiao, J. C. Craig, and S. J. Bensmaia, "Convergence of submodality-specific input onto neurons in primary somatosensory cortex," *J. Neurophysiol.*, vol. 102, no. 3, pp. 1843–1853, Sep. 2009.

[223] A. W. Carter, S. C. Chen, N. H. Lovell, R. M. Vickery, and J. W. Morley, "Convergence across tactile afferent types in primary and secondary somatosensory cortices," *PLoS One*, vol. 9, no. 9, pp. e107 617–e107 617, Jan. 2014.

[224] H. Barlow, "Redundancy reduction revisited," *Network*, vol. 12, no. 3, pp. 241–253, Aug. 2001.

[225] J. L. Puchalla, E. Schneidman, R. A. Harris, and M. J. Berry, "Redundancy in the population code of the retina," *Neuron*, vol. 46, no. 3, pp. 493–504, 2005. [Online]. Available: https://www.sciencedirect.com/science/article/pii/S0896627305003119

[226] H. B. Barlow, "Possible principles underlying the transformations of sensory messages," in *Sensory Communication*. The MIT Press, Aug. 2013.

[227] R. H. Watkins, M. Amante, H. B. Wasling, J. Wessberg, and R. Ackerley, "Slowly-adapting type II afferents contribute to conscious touch sensation in humans: evidence from single unit intraneural microstimulation," *J. Physiol.*, May 2022.

[228] J. A. Pruszynski and R. S. Johansson, "Edge-orientation processing in first-order tactile neurons," *Nat. Neurosci.*, no. August, pp. 1–7, Aug. 2014.

[229] F. Pedregosa, G. Varoquaux, A. Gramfort, V. Michel, B. Thirion, O. Grisel, M. Blondel, P. Prettenhofer, R. Weiss, V. Dubourg, J. Vanderplas, A. Passos, D. Cournapeau, M. Brucher,

M. Perrot, and E. Duchesnay, “Scikit-learn: Machine learning in Python,” *Journal of Machine Learning Research*, vol. 12, pp. 2825–2830, 2011.

[230] C. E. Shannon, “A mathematical theory of communication,” *The Bell system technical journal*, vol. 27, no. 3, pp. 379–423, 1948.

# Conclusion

## 1 Impact

In this thesis, we have explored the neuroscience of touch in the context of its application to robotics and prosthetics. Our studies aimed to shed light on the mechanisms underlying tactile perception and how these can be leveraged to develop more sophisticated and effective devices that can mimic or enhance human touch.

We have shown that touch is a complex sensory modality that involves a variety of neural structures and processes, from the peripheral nerves in the skin to the somatosensory cortex in the brain. We have discussed the role of different types of mechanoreceptors in encoding different features of tactile stimuli, such as texture, pressure, and vibration, and possible mechanisms showing advantages in therms of the integration and processing of such information carried out by the brain to give rise to our subjective experience of touch.

We have also examined some of the challenges and opportunities associated with developing neuromorphic touch-sensitive robotics and prosthetics. We have highlighted the importance of designing devices that can mimic the complexity and flexibility of human touch, while also being robust, reliable, and easy to use. We have discussed some of the strategies that have been proposed to achieve this, including the use heterogeneous populations of sensors providing complementary but also redundant information about the surroundings.

Overall, this thesis has shown that the neuroscience of touch holds great promise for the development of innovative and transformative technologies that can improve the lives of many people. By better understanding the mechanisms of touch perception and using this knowledge to

inform the design of touch-sensitive devices, we can create new opportunities for individuals with disabilities, as well as for a wide range of applications in industry (exoskeletons and orthoses), healthcare (surgery robots), and entertainment (haptics for virtual reality).

## 2 Future work

There is still much work to be done in this field, and many unanswered questions remain. However, the research presented in this thesis represents an important step towards a better understanding of the neuroscience of touch and its application to robotics and prosthetics. It is our hope that this work will inspire further research and innovation in this exciting and rapidly evolving field.

Future investigations can address a wide range of topics following up this thesis. First, from a pure neuroscientific point of view, the fundamental knowledge about tactile encoding is far from being complete. Understanding whether the somatosensory cortex applies any of the principles suggested in this thesis might be the next step towards a better understanding of touch. Second, addressing a question more related to the applicability and transfer of knowledge about touch to robotics and prosthetics, investigations should be focused in conveying whether the strategies suggested in this thesis can be replicated using artificial sensors mimicking the mechanoreceptors biological properties, in terms of responses and dynamics.